THE ASTROPHYSICAL JOURNAL SUPPLEMENT SERIES, 54:291–334, 1984 February

HIGH-RESOLUTION VLA OBSERVATIONS OF THE RADIO JET IN NGC 6251

R. A. PERLEY AND A. H. BRIDLE
National Radio Astronomy Observatory[1]

AND

A. G. WILLIS
Athabasca University, Edmonton, Alberta
Received 1983 May 19; accepted 1983 August 24

ABSTRACT

The jet in the radio galaxy NGC 6251 has been observed with the VLA using resolutions from 1.″15 to 15″ at 1370, 1480, 1662, and 4885 MHz, and a resolution of 50″ at 1446 and 1662 MHz. The resulting maps give exceptionally detailed information on the distributions of the total and polarized intensity over the jet. There are no significant gradients in spectral index, either along or across the jet. The transverse deflections of the jet have a complex spectrum in which longer "wavelengths" dominate at greater distances from the radio core. An oscillation with a wavelength of 143″ (61 kpc) dominates the shape of the jet beyond 240″ (103 kpc) from the core.

The jet expands laterally at a variable rate, exhibiting several stages of confinement and reexpansion. Its only center-darkened feature is located immediately coreward of the first slowdown in its lateral expansion. The brightness of the jet varies with its width in a manner which suggests that relativistic particle reacceleration or magnetic field amplification, or both, occurs many tens of kpc from the radio core.

A counterjet has been detected for ~130″ (~56 kpc) in the direction opposite to that of the main jet. The ratio of intensities between the jet and the counterjet varies between 40:1 and ≥ 200:1 with distance from the core.

There are large and complex gradients of the Faraday rotation measure both along and across the jet which we attribute to the presence of a magnetoionic medium outside the jet but within NGC 6251. The (density-weighted) line-of-sight magnetic field reverses direction over distances of ~10 kpc within NGC 6251. Some features of the rotation measure distribution correlate with changes in the expansion properties of the jet, suggesting that the magnetoionic medium in NGC 6251 interacts with the jet. There is no evidence for depolarization of the jet by thermal material within it, although a *false* depolarization is produced at low resolutions by the gradients in the Faraday rotation measure.

The projected magnetic configuration of the jet is dominated by the component parallel to the jet axis for the first 90″ (40 kpc) from the core. Further from the core the field on the axis of the jet is dominated by the perpendicular component, while the field at the edge remains predominantly parallel. There are, however, significant regions where the magnetic configuration is dominated by oblique field components. These regions are also anomalous in their expansion and brightness-radius behaviors, and may be related to the formation of shocks in the jet.

The implications of these results for the physics of the jet are discussed. Confinement of the jet by thermal pressure of a hot gaseous halo associated with NGC 6251 is considered. Thermal confinement of the jet beyond 7 kpc from the core requires a 0.5 to 4 keV luminosity on a scale of 50 kpc around the galaxy that is consistent with *Einstein* observations of NGC 6251 and of the X-ray halos of other elliptical galaxies. The rapidly expanding section of the jet closer to the core is probably free, however.

Helix-like and sheared tangled-field geometries are considered for the three-dimensional magnetic structure of the jet; the data require a mixture of random and organized field components whichever geometry is adopted for the organized field. Emission models which have axial symmetry cannot reproduce all observed features of the total and polarized intensity data. The ability of particle acceleration mechanisms based on large-scale turbulence to fit the observed brightness variations along this jet depends critically on how the widths of the synchrotron emissivity and of the flow through the jet are assumed to be related. The polarization data are used to place upper limits on the thermal density in the jet, assuming some explicit configurations for its internal magnetic field.

[1]The National Radio Astronomy Observatory is operated by Associated Universities, Inc., under contract with the National Science Foundation.

Several model-dependent estimates are made of the mean velocity of the jet. The constraints of the velocity are weak without a firm estimate of the thermal density within the jet. Plausible cold jet models exist with velocities near 8000 km s^{-1} and efficiencies of converting bulk kinetic energy to synchrotron radiation in the lobes near 0.04. Similarly efficient hot relativistic jet models cannot, however, be excluded without further data on the symmetries between the jet and the counterjet. Several models for the lateral deflections of the jet are examined.

Subject headings: galaxies: individual — galaxies: jets — interferometry — polarization — radio sources: galaxies

I. INTRODUCTION

It has become widely believed (e.g., the reviews by Miley 1980; Fomalont 1980; Rees, Begelman, and Blandford 1981; Willis 1981; Bridle 1982) that the long, well-collimated radio jets which link the active nuclei of many radio galaxies and quasars to their extended radio lobes are dissipative examples of an energy transport "pipeline" that is present in all large-scale extragalactic radio sources. Detailed studies of the brightness and polarization distributions over such radio jets are therefore expected to lead to improved understanding of the processes whereby the energy reservoirs in the extended radio lobes of these sources are replenished from the central objects. Of particular interest are observations of the following:

1) The rates of widening of the jets, which provide clues to the location of, and mechanism for, collimation of the sources;
2) Their intensity and spectral distributions, which provide evidence for the location of, and amount of, relativistic particle acceleration along the jet paths;
3) Their Faraday rotation and depolarization properties, which may constrain models of their thermal matter content;
4) Their magnetic field configurations, which are essential ingredients of detailed comparisons between their radiative structures and models for the dynamics of the underlying flows.

This paper reports multifrequency observations of the radio jet in the 14 mag elliptical galaxy NGC 6251 using the Very Large Array (VLA) (Thompson *et al.* 1980) of the National Radio Astronomy Observatory. The jet in NGC 6251 is particularly suitable for detailed multifrequency study for several reasons. It is one of the brightest known examples of a well-collimated asymmetric (i.e., "one-sided") jet in a moderately powerful radio galaxy ($P_{1480} \approx 2.2 \times 10^{24}$ W Hz^{-1}). Furthermore, it can be resolved in the transverse direction at all VLA frequencies and can be traced along its length for several hundred VLA beamwidths. The evolution of its properties with distance from the central active object can therefore be determined in unusually rich detail.

Section II of this paper briefly reviews previous observations of NGC 6251, and § III describes our observing and data reduction procedures. Sections IV and V present the total intensity and polarized intensity characteristics of the jet derived from the new VLA observations. Section VI summarizes the principal organized features of the jet; readers with a primarily theoretical interest in jet phenomena may prefer to review this section before reading §§ III and IV.

Section VII discusses the impact of our results on models of physical processes in the jet. Section VII*a* deals with the question of whether, and where, the jet is free or confined. Section VII*b* discusses the evidence for a magnetoionic medium in NGC 6251. The structure of the magnetic field in the jet is modeled in § VII*c*, and the evidence for, and mechanisms of, particle acceleration in the jet are discussed in § VII*d*. Section VII*e* deals with the constraints on the thermal electron density within the jet. Constraints on its velocity are examined in § VII*f*. The nature of the lateral oscillations of the jet is discussed in § VII*g*. Section VIII summarizes our conclusions about its physical parameters.

II. PREVIOUS OBSERVATIONS OF NGC 6251

The radio emission associated with NGC 6251 was first studied by Waggett, Warner, and Baldwin (1977), who showed that a bright, well-collimated radio jet links a small-diameter radio core to one of two large-scale emission regions on either side of the parent galaxy. The large-scale emission has a total extent of 1°.1 (see Fig. 1). At the measured redshift of 0.023 (Longair and Schuch, quoted by Waggett *et al.*) this corresponds to a projected linear size of 1.7 Mpc (for $H_0 = 75$ km s^{-1} Mpc^{-1} the image scale is 429 pc $arcsec^{-1}$). The source is therefore one of the largest known radio galaxies.

Young *et al.* (1979) noted that NGC 6251 is on the edge of the loose cluster of galaxies Zw 1609.0+8212, whose redshift is 0.024, in good agreement with the redshift of NGC 6251 quoted by Waggett *et al.* They also reported that its optical spectrum is that of a normal giant elliptical galaxy except for a weak, sharp O[III] λ5007 emission line. They showed that its luminosity profile does not conform to a King model, but has a central "light spike" similar to that in M87 (Young *et al.* 1978; Sargent *et al.* 1978).

The radio jet has an initial relatively straight bright region 4'.4 (113 kpc) long (Waggett *et al.*) and a fainter curved extension 3'.5 (90 kpc) long (Willis, Wilson, and Strom 1978). VLBI observations (Readhead, Cohen, and Blandford 1978; Cohen and Readhead 1979) revealed a parsec-scale jet extending from a compact component toward the large-scale jet along P.A. 300°.5 ± 2°. This *VLBI* "minijet" is misaligned with the mean position angle of the larger scale jet by 4° ± 2°. It is unclear, however, whether the jet radiates on all scales from ~1 pc to the kpc scale of the base of the large-scale jet, because of the great difference in angular resolution and brightness sensitivity between the *VLBI* observations and the published maps made with connected interferometers (e.g., Saunders *et al.* 1981).

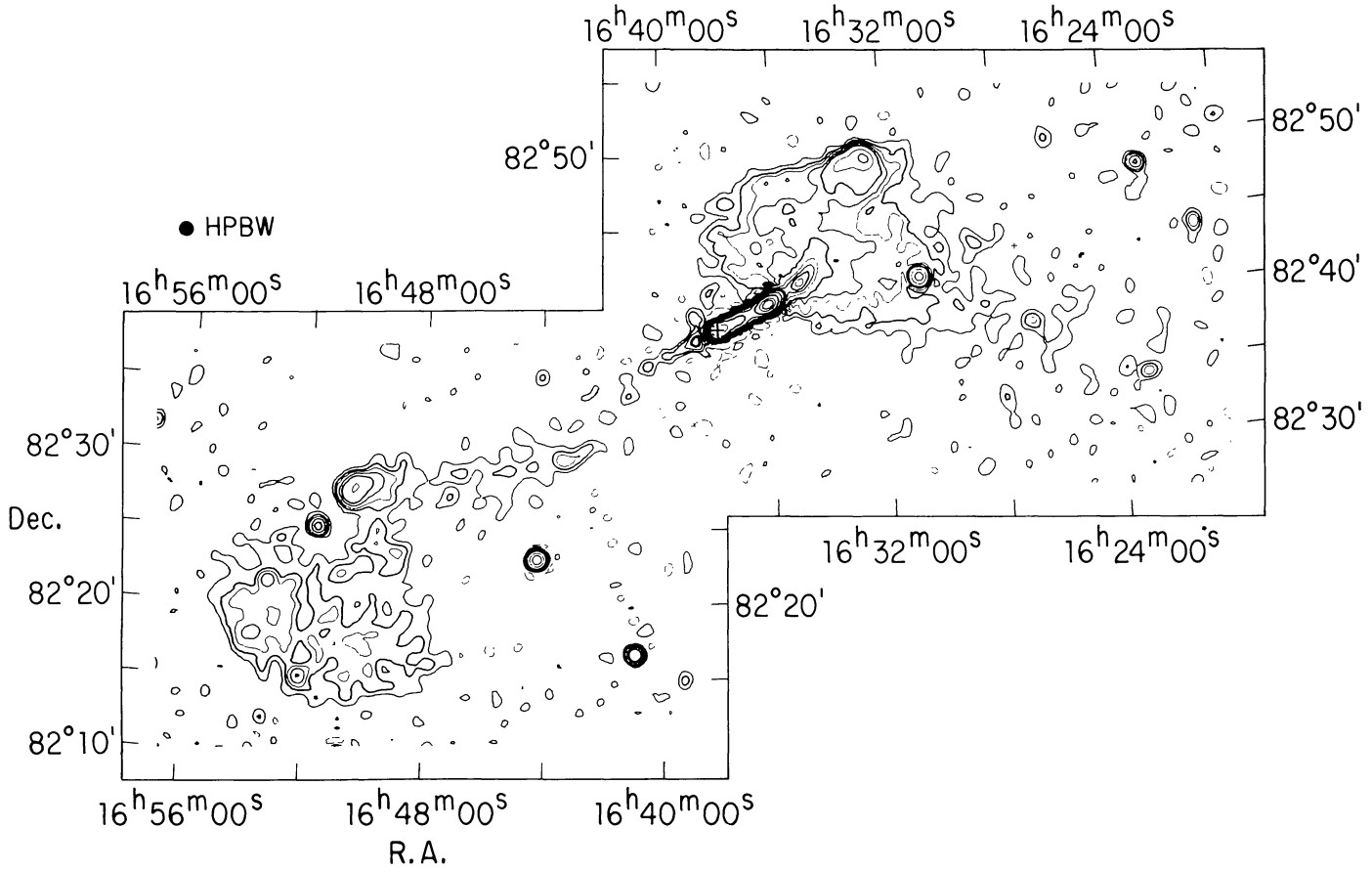

FIG. 1.—Map of the entire NGC 6251 source at 610 MHz with 50″ resolution (from Willis *et al.* 1982). The cross marks the position of the nucleus of NGC 6251.

TABLE 1A

VLA OBSERVING PARAMETERS

PARAMETER	DATE			
	1979 Nov 05	1980 Mar 31	1980 Dec 05	1981 Oct 05
Frequency (MHz)	1479.9	4885	1370/1662	1446/1662
Bandwidth (MHz)	12.5	6.25	25/25	12.5/12.5
Number of antennas	14	21	22/22	27/27
Duration (hr)	12	10.5	6/6	0.16/0.16
Configuration	mixed	mixed	A	D
Minimum baseline (kλ) ...	0.2	0.6	2/2.4	0.1/0.11
Maximum baseline (kλ) ...	94	120	155/185	5.6/6.4
α (fringe stopping)	16 37 20.00	16 37 00.00	16 37 45.230	16 37 56.970
δ (fringe stopping)	82 38 50.00	82 39 15.00	82 38 29.08	82 38 18.50

TABLE 1B

ASSUMED 3C 286 FLUX DENSITIES

Frequency (MHz)	Flux Density (Jy)
1370.....	14.99
1446.....	14.60
1480.....	14.44
1662.....	13.62
4885.....	7.41

III. THE VLA OBSERVATIONS

We observed NGC 6251 with the VLA on five occasions. Table 1A gives the main parameters of the observations. The 1480 and 4885 MHz data were obtained using nonstandard VLA configurations, with a greater density of short baselines than the 1370 and 1662 MHz data, but poorer sampling of the longer baselines (see Fig. 2). We therefore use the 1480 and 4885 MHz data for most analyses of the larger scale structures throughout this paper, but the 1370 and 1680 MHz data where the highest angular resolution is essential. At each frequency,

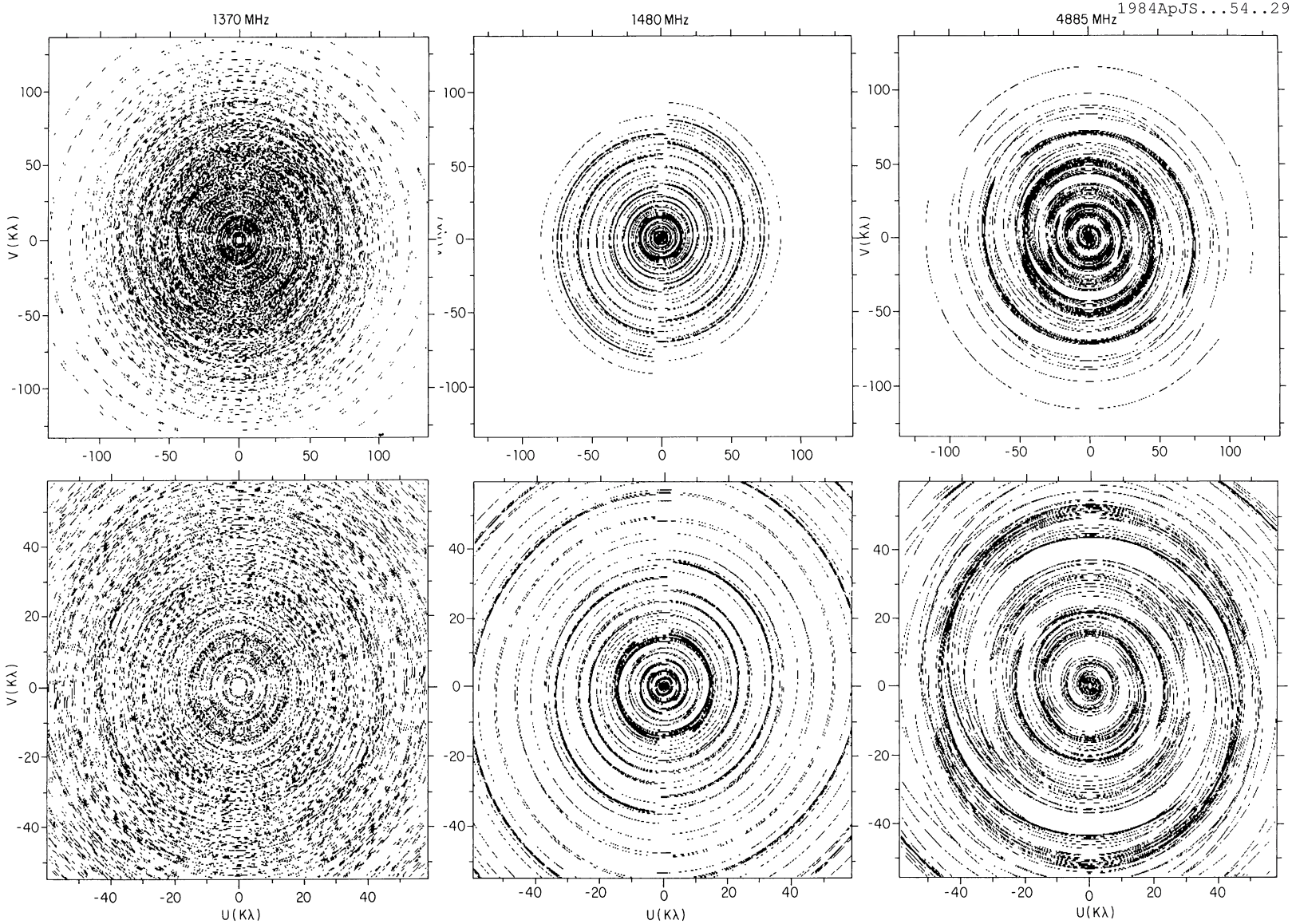

FIG. 2.—Plots of the (u, v)-plane coverages obtained in the principal 1370, 1480, and 4885 MHz observing sessions reported in this paper. *Upper row*: the (u, v)-plane coverage out to 135 kλ. *Lower row*: expanded view of the inner 58 kλ, showing the superior coverage of the inner 3.5 kλ of the (u, v)-plane for the 1480 and 4885 MHz data.

the flux density scale was normalized to that of Baars *et al.* (1977) by observations of 3C286. Table 1B lists the assumed flux density of 3C286 at each observing frequency.

NGC 6251 contains a "core" radio component that is unresolved to the VLA. This component, which coincides with the optical nucleus of the galaxy, has a flux density greater than or equal to 0.4 Jy at all of our observing frequencies. Furthermore, most of the emission from the jet is resolved out over baselines longer than 50 kλ (1 kλ = 1000 wavelengths) at these frequencies. We were therefore able to use the core component as a phase reference over the longer baselines to correct the observations for atmospheric and ionospheric phase fluctuations, as described by Perley, Fomalont, and Johnston (1980). This procedure allowed us to achieve dynamic ranges of ~ 500:1 in the initial CLEAN (Högbom 1974) total intensity maps.

The calibration of the atmospheric and ionospheric fluctuations was further refined using the self-calibration algorithm of Schwab (1980) with source models obtained by CLEANing the initial maps. The absolute coordinates of the maps were lost in the phase-referencing processes, but were recovered using the position of the radio core ($\alpha_{1950.0} = 16^h37^m56^s.970 \pm 0^s.024$, $\delta_{1950.0} = +82°38'18''.50 \pm 0''.05$) obtained from independent astrometry (Perley 1982). "Zero-spacing" flux densities of 2.4 Jy at 1370 MHz, 2.2 Jy at 1480 MHz, 2.0 Jy at 1662 MHz, and 1.2 Jy at 4885 MHz were added to the VLA data in the mapping process to minimize the zero-level offsets ("bowls") around the jet on the final maps. These flux densities were determined from measurements of the visibility function of NGC 6251 at short baselines using the D-configuration of the VLA.

The maps were processed using the NRAO Astronomical Image Processing System (AIPS). All maps were CLEANed (Högbom 1974; Clark 1980) and restored with truncated circular Gaussian beams; they have also been corrected for attenuation by the primary beam pattern of the individual VLA antennas.

The on-axis instrumental linear polarizations of the antennas were calibrated to ±0.1% from observations of the source 1803+784. The polarization position angle scale at each frequency was set by assuming that the integrated linear polarization of 3C286 is at P.A. 33°. Since 1803+784 was appreciably linearly polarized at the time of these observations (> 6.5% at 1662 MHz in 1980 December), it was monitored throughout them to track changes in the ionospheric Faraday rotation. The apparent position angle of its linear polarization changed by less than 10° during each of the 12 hr observations, showing that the properties of the ionospheric Faraday screen were stable within our observing periods. We also used an ionospheric modeling program developed by R. C. Bignell to test whether the ionospheric Faraday rotations should reasonably have been expected to be small throughout each observing period, based on ionospheric electron densities measured at the time of the observations. The rotation corrections predicted by the model at 1370 MHz were less than 10° throughout each of our observing periods. Both our observations of the polarized calibrator and the ionospheric model therefore imply that the systematic uncertainties in our quoted polarization position angles should be less than or equal to 5°.

IV. TOTAL INTENSITY PROPERTIES

a) Maps

Figure 3 shows a map of the first 4'.4 (113 kpc) of the jet at 1480 MHz with resolution (FWHM) of 2''.11 (0.9 kpc). The first 4'.4 of the jet can be divided into three structurally distinct regions:

1) The *inner* region within 120'' (~ 50 kpc) of the radio core, wherein the jet is bright and contains many discrete knots;

2) A faint *central* region extending from ~120'' to ~180'' (~ 50 to ~ 75 kpc) from the core in which there are no bright knots;

3) An *outer* bright region ~ 90'' (~ 40 kpc) long in which the bright knotty substructure reappears but the transverse intensity profiles are generally asymmetric, in contrast to those in the inner and central regions.

The fainter curved extension of the jet discovered by Willis, Wilson, and Strom (1978) is considered to be a fourth structural regime throughout this paper. It is too diffuse to register on any of the VLA maps with beamwidths smaller than 15'', so we do not discuss it in as much detail as the first 4'.4 of the jet.

Both the large (arc minute) scale brightness fluctuations and the knotty substructure of this jet contrast with the generally smooth brightness gradients along the well-resolved jets of NGC 315 (Willis *et al.* 1981) and 3C31 (Fomalont *et al.* 1980).

Figure 4 (*left panel*) displays the innermost 58'' (~ 25 kpc) of the jet at 1''.15 resolution (FWHM) at 1662 HMz. At this resolution (493 pc) there are two bright elongated knots in the first 2''–6'' (0.9–2.6 kpc) of the jet. This contrasts with the structure at the bases of the jets in NGC 315 (Bridle *et al.* 1979), 3C31 (Fomalont *et al.* 1980), and 3C449 (Perley, Willis, and Scott 1979). These sources have "gaps" (i.e., regions of greatly diminished emission) several kpc long between the brightest jet emission and the unresolved radio cores, when observed with spatial resolutions similar to that obtained here for NGC 6251. The emission in these "gaps" is fainter than the bright knots at the bases of their jets by factors between 5:1 and 20:1 (VLA observations have detected faint emission within the previously reported "gaps" in NGC 315 and 3C449; see Bridle, Fomalont, and Henriksen 1983; Perley and Cornwell 1983). The brightness *contrast* between the first few kpc of the jet in NGC 6251 and the brightest train of knots along it is much less than that in the corresponding regions of the jets in NGC 315, 3C31, and 3C449. In this sense NGC 6251 may represent one extreme of "gap" size in a jet, the other being represented (among sources which do have detectable jets) by the more powerful sources 3C219 (Perley *et al.* 1980), 3C388 (Burns, Christiansen, and Hough 1982), and 3C438 (Laing, Bridle, and Fomalont 1983), which have "gaps" 13, 7, and 13 kpc long, respectively, between their cores and the first bright knots in their jets.

The "ears" extending from the core roughly perpendicular to the jet in Figure 4 are an instrumental artifact at the −30 dB level resulting from an intentional offset of the intense core from the fringe stopping center during these observations. This level of artifact does not influence the other features of

the map, because their peak intensities are much less than that of the core component. Test observations made in the VLA A-configuration at 1480 MHz with the core at the fringe stopping center showed that the appearance of the first 10″ of the jet in Figure 4 is not significantly distorted by this effect. Despite their lower sensitivity, these test observations also confirmed that the "ears" appearing in Figure 4 are an artifact.

Figure 4 (*right panel*) displays the next 63″ (~ 27 kpc) of the jet at the same resolution. Between ~ 80″ and ~105″ from the core the ridge line of the jet undergoes perturbations of amplitude ~1″; these and other transverse oscillations of the jet are discussed in more detail in § IV*c* below. Note that most of the transverse brightness profiles in this region of the jet are more centrally symmetric than those in the outer jet (see Fig. 3).

b) The Spectral Index Distribution of the Jet

Figure 5 shows maps of the first 200″ (~125 kpc) of the jet at the same resolution (4.4″ FWHM) at 1480 and 4885 MHz. The dense coverage of the inner part of the (u, v)-plane at these two frequencies (see Fig. 2, *lower row*) makes it unlikely that significant extended emission is missing or misrepresented on either map at this resolution. These maps are therefore the most appropriate for spectral comparison. The very strong similarity of the two maps in Figure 5 shows the lack of spectral index gradients along or across the jet between these frequencies.

Figure 6 shows a one-dimensional profile of the 1480–4885 MHz spectral index α [defined as $S(\nu) \propto \nu^{-\alpha}$] along the ridge line of the jet, derived from maps made at these frequencies at 10″ resolution. The spectral index increases by less than 0.05 over the first 240″ (~100 kpc) of the jet, and is everywhere within the uncertainties of 0.64 ± 0.05. This spectral index is the same as that given for the source as a whole below 2.7 GHz by Waggett, Warner, and Baldwin (1977). Saunders *et al.* (1981) deduced an index of 0.58 ± 0.05 for the jet between 408 and 5000 MHz. This is consistent with our estimate to within the combined errors. Differences between the Cambridge and VLA flux density calibrations could account for the slight discrepancy (a 5% difference in flux density scale at either 1480 or 4885 MHz would translate into a spectral index discrepancy of 0.04 between these frequencies).

c) The Transverse Oscillation of the Jet

The ridge line of the jet is not straight. Its first 120″ (~ 50 kpc) exhibit small oscillations around a mean position angle of $296\overset{\circ}{.}4 \pm 0\overset{\circ}{.}1$ (in excellent agreement with the earlier estimate of $296\overset{\circ}{.}5 \pm 0\overset{\circ}{.}5$ by Waggett, Warner, and Baldwin 1977). The outer jet has large deflections from this position angle, as noted by Saunders *et al.* (1981). We measure the deviations Δ of the peaks of the transverse brightness profiles of the jet from an axis along P.A. $296\overset{\circ}{.}4$, as a function of angular distance Θ from the core at several resolutions.

Figure 7 (*upper*) plots Δ/Θ against $\Theta \leq 120''$. Figure 7 (*lower*) plots the same quantities for $\Theta \leq 400''$. An harmonic oscillation whose amplitude increases linearly with Θ would appear as a sine wave on these plots. Such a linear increase of amplitude with distance from the core could be produced, for example, by precession of the primary collimator (Begelman, Blandford, and Rees 1980), or by growth of a Kelvin-Helmholtz instability on an *expanding* jet (Hardee 1982).

Figure 7 shows the presence of oscillations with (projected) wavelengths 143″, 31″, and 9″ in the ridge line deviations of the jet. The 143″ oscillation can also be seen in Figure 8, a 1480 MHz map at 15″ resolution which traces the oscillation through the fainter extension of the jet. The 9″ oscillation dominates in the first 40″ of the jet, while the 31″ oscillation is most prominent between 120″ and 240″ from the core. Note, however, that the resolution of the data along the jet changes with distance from the core. The jet becomes wider, and thus more difficult to detect at a given resolution, further from the core. There is therefore some bias toward detecting longer wavelength oscillations in the outer parts of the jet and shorter wavelength oscillations in the inner parts.

To test whether the more complex behavior of the jet deflections at other distances from the core (e.g., between 40″ and 120″ from the core) is due to beating between a few clear-cut oscillation wavelengths, we made power spectrum analyses of the variations of both Δ/Θ and Δ with Θ. We used the mean removal and prewhitening techniques described by Blackman and Tukey (1958) and examined the significance of peaks in the power spectra using the criteria given by Lake and Roeder (1972) and Burbidge and O'Dell (1972). These power spectra showed the following:

1) That no *single* wavelengths contain excess power at the 99% significance level *over the entire length* of the jet;

2) That the peaks in the power spectra of the *normalized* deviations Δ/Θ are generally more significant than those in the spectra of Δ;

3) That, in addition to the wavelengths of 143″, 31″, and 9″, an oscillation with projected wavelength 5.″7 is present in the inner 120″ of the jet at the greater than 99% significance level, and an oscillation with projected wavelength 12″ is present in the range $20'' < \Theta < 100''$ at this significance level.

Results (1) and (2) confirm the conclusions drawn directly from Figure 7 that the dominant oscillation wavelengths lengthen with increasing distance from the core, and that their amplitudes also grow with distance from the core.

The 143″ (~ 61 kpc) oscillation dominates the behavior of the jet beyond ~ 240″ (100 kpc) from the core. It was previously noted by Saunders *et al.* (1981), whose Figure 4 may be compared with our Figure 7. Saunders *et al.* report the wavelength as 125″. The discrepancy with our value is within the errors of estimation from our data and from their Figure 4. Figures 3 and 8 show that the 143″ oscillation involves the lower level contours as well as the ridge line of the jet. It therefore represents a bulk displacement of the synchrotron-emitting material rather than changes in the internal symmetry of the transverse intensity profiles. The oscillation is superposed on a roughly parabolic drift of the ridge line of the jet toward the northwest. The amplitude of the oscillation (after removing the contribution due to the drift) grows approximately linearly with distance from the core.

The oscillation with 31″ (~13 kpc) projected wavelength which is traced by the peaks of the knots in the outer jet grows

(This Page Intentionally Left Blank)

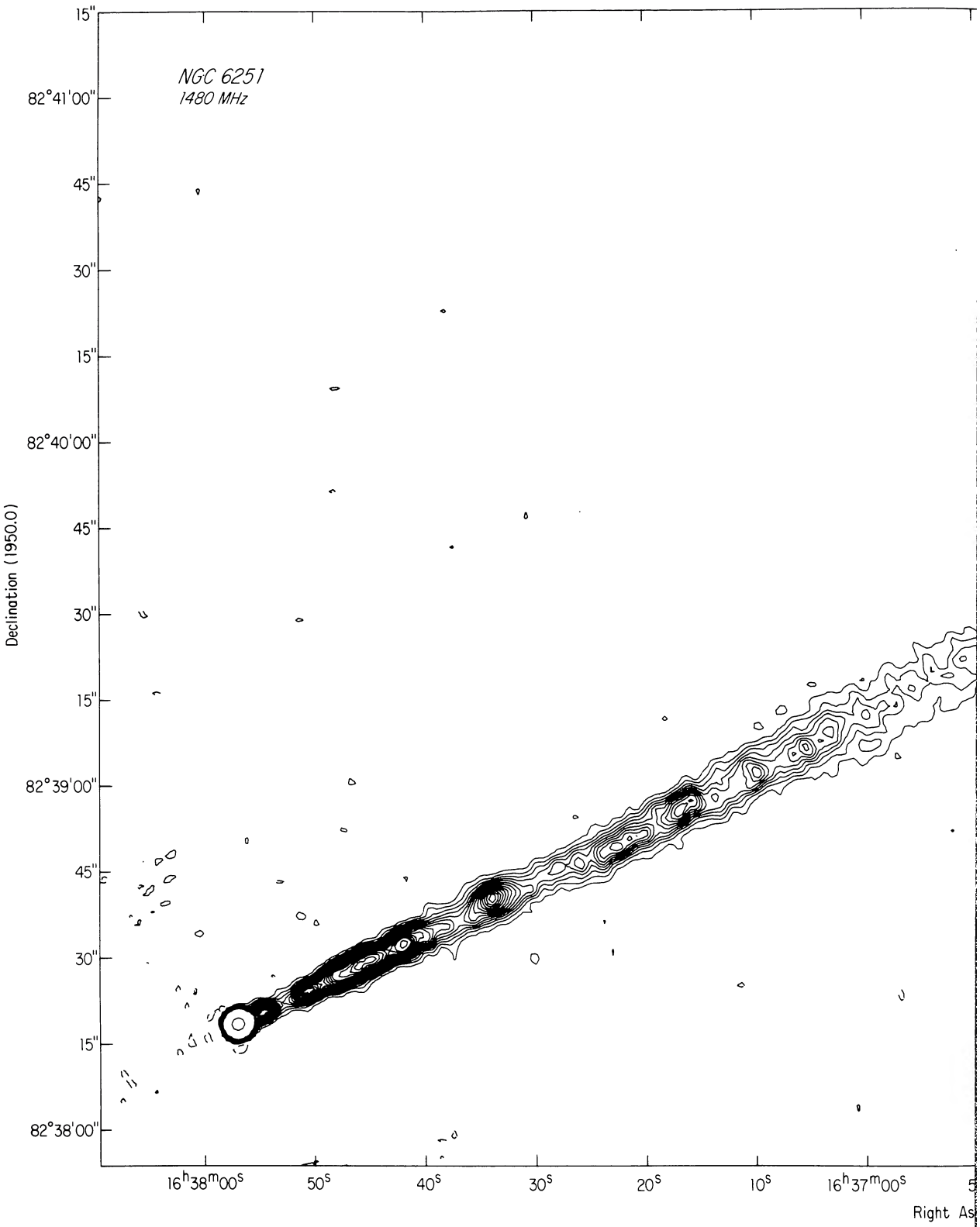

FIG. 3.—Unrotated map of the inner 4'.4 of the jet at 1480 MHz with 2".11 resolution. Contours are drawn at −0.448 (*dashed*) and + per beam. The highest contour delineates the FWHM of the beam around the peak of the core source.

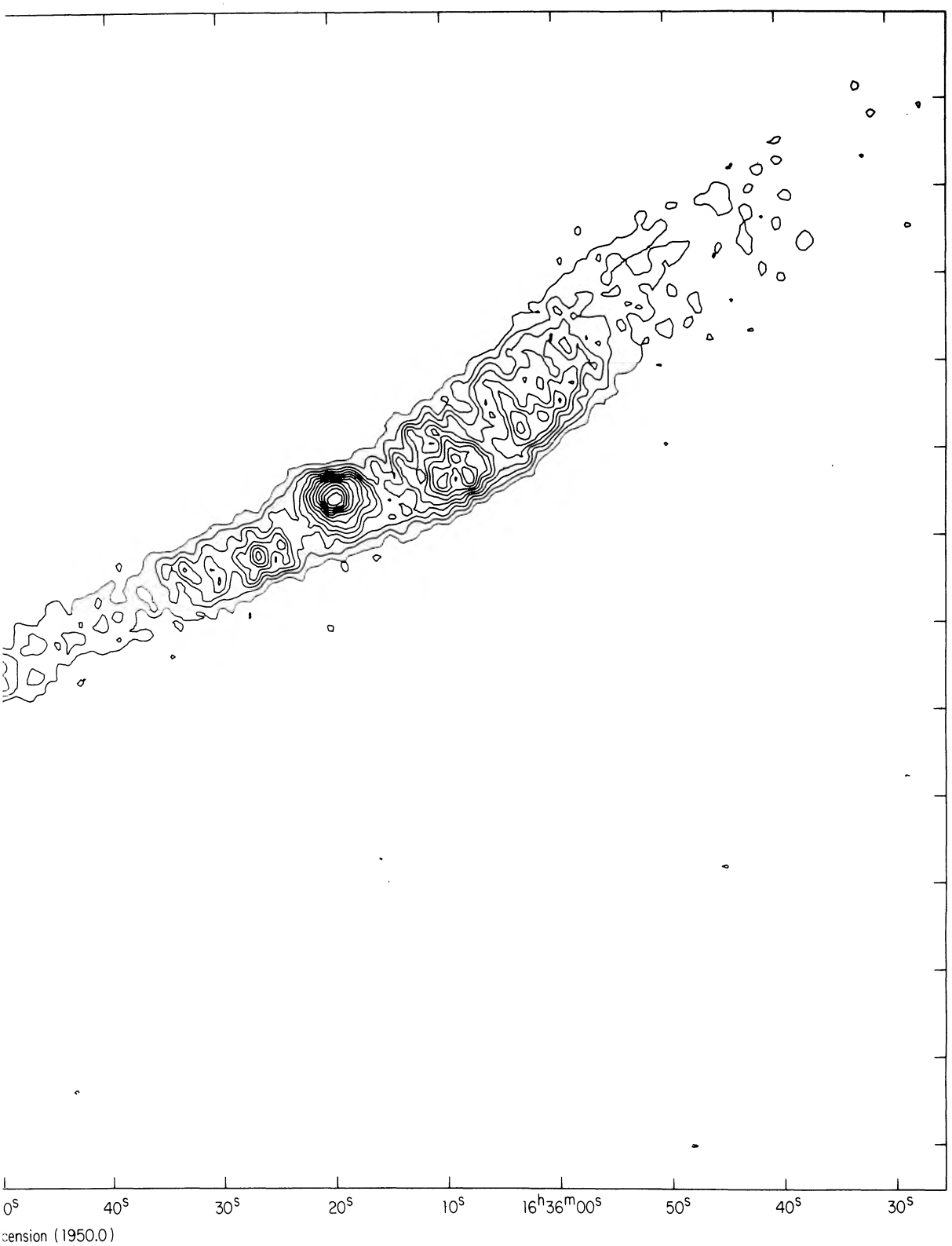

0.448 mJy per beam, then at equal intervals of 0.448 mJy per beam until 6.27 mJy per beam, then at 7.17, 8.06, 8.96, and 224 mJy

(This Page Intentionally Left Blank)

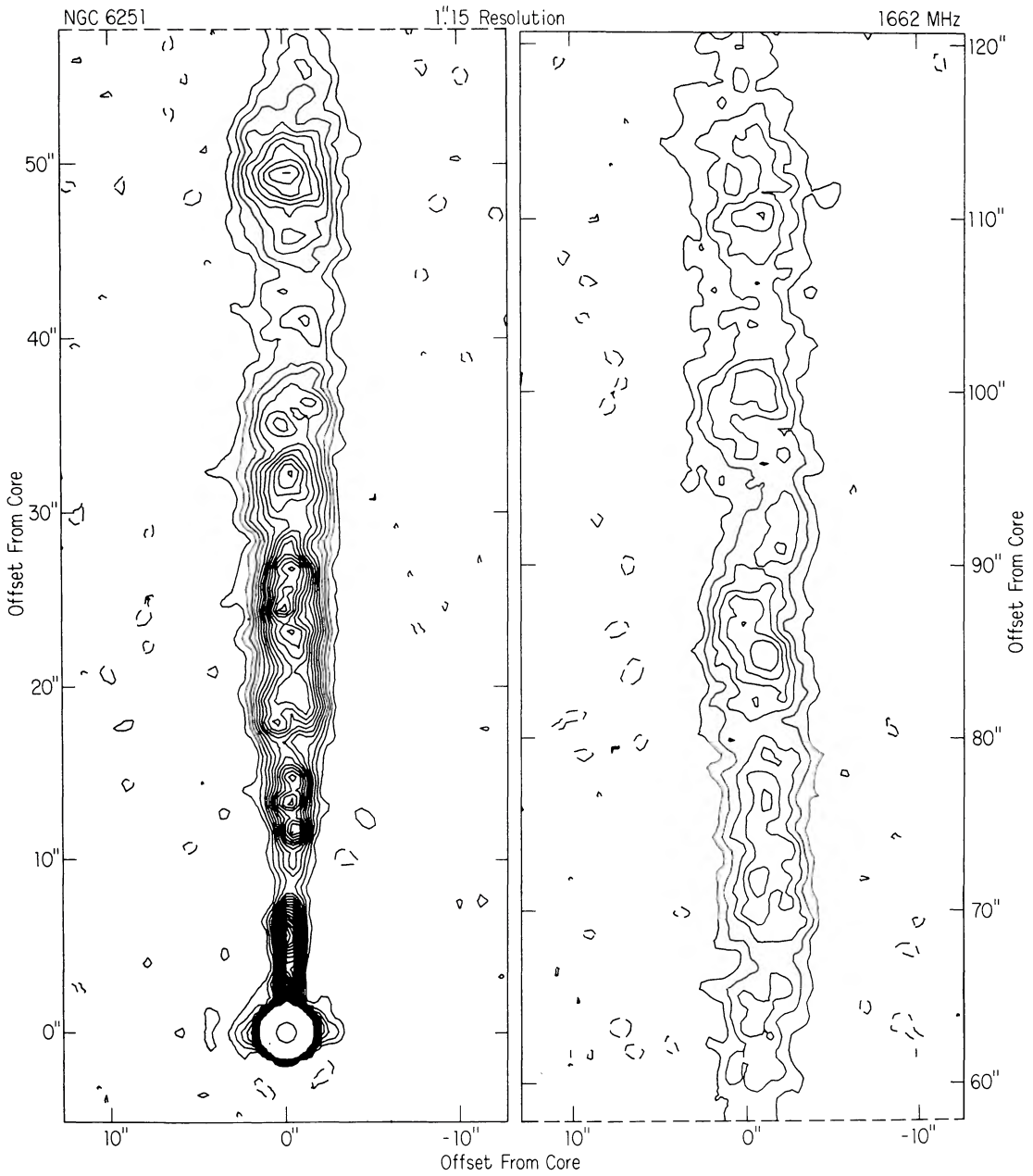

FIG. 4.—Rotated map of the inner 2′ of the jet at 1662 MHz with 1".15 resolution. Contours are drawn at −0.226 (*dashed*) and +0.226 mJy per beam, then at equal intervals of 0.226 mJy per beam until 4.07 mJy per beam. A further contour at 226 mJy per beam delineates the FWHM of the beam around the peak of the core source. The "ears" around the core approximately at right angles to the jet are an instrumental artifact (see text).

faster than linearly over the range $100'' < \Theta < 250''$. This oscillation involves changes in the symmetry of the transverse intensity profiles and does not appear to involve the lower intensity levels. It thus does *not* represent a bulk displacement of the entire jet.

The faster oscillations in the inner 100" of the jet (Fig. 7, *upper panel*) grow more slowly than linearly with distance from the core. Since the transverse emission profiles here are not so well resolved as those in the outer jet, we cannot be sure of the extent to which the fast oscillations result from changes in profile shape rather than from bulk displacements of the jet.

d) *The Collimation of the Jet*

The "width" of a radio jet can be parameterized in several ways. For a jet with symmetric, centrally brightened transverse profiles the FWHM of a Gaussian function fitted to the profile shapes (Bridle *et al.* 1980; Willis *et al.* 1981) is a simple and practical measure. The outer jet in NGC 6251 has transverse intensity profiles that are not centrally symmetric, however (see Fig. 3). Figure 9 shows some representative profile shapes; note the asymmetries of the profiles shown in Figs. 9*e* and 9*f*.

The relation between the FWHM Φ and an isophotal width ϕ of a profile depends on its shape and on its peak brightness.

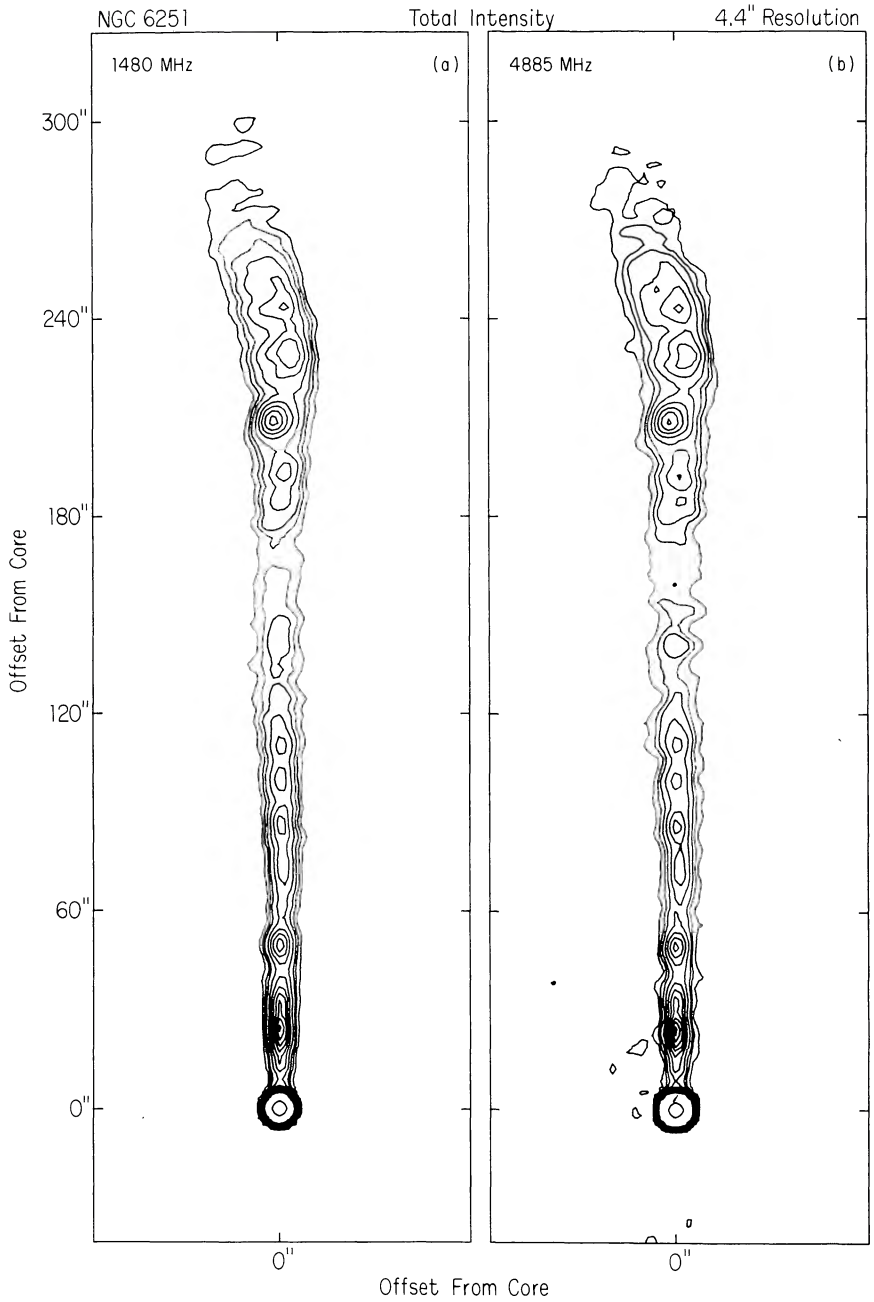

FIG. 5.—Maps of the inner 5′ of the jet at (*a*) 1480 and (*b*) 4885 MHz with 4.″4 resolution. The contour intervals (−1, 1, 2, 3, 5, 7.5, 10, 12.5, 15, 17.5, 20, 22.5, and 25 times [*a*] 1.33 mJy and [*b*] 0.6 mJy) are chosen so that emission with a spectral index of 0.61 between these frequencies would contour at the same relative level in each map.

In the bright knots in the outer jet of NGC 6251, the FWHM decreases even though there is little or no associated perturbation of the outer isophotes of the jet. How such variations relate to the collimation properties of any underlying flow depends on the physical processes governing the distribution of the synchrotron emissivity over the jet. It is not clear which, if any, of the practical width measures for a radio jet is best compared with the parameters of theoretical models. We therefore display two measures of the jet width for the outer parts of this jet:

1) The deconvolved Gaussian FWHM Φ. We fit a Gaussian of FWHM Φ_o to the observed transverse intensity profile, then deconvolve the FWHM Φ_b of the CLEAN beam from this Φ_o using the relation $\Phi = (\Phi_o^2 - \Phi_b^2)^{1/2}$;

2) The isophotal width ϕ to an outer brightness level on the map, with a first-order correction for the finite beamwidth.

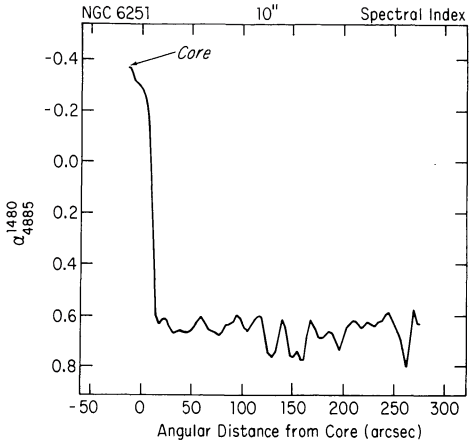

FIG. 6.—One-dimensional profile of spectral index between 1480 and 4885 MHz along the ridge line of the jet at 10″ resolution. The local fluctuations away from the core illustrate the uncertainties in the spectral index determination.

Figure 10 shows the expansion of the jet with angular distance Θ from the radio core over its inner 250″, using width measures from the 1662 MHz map at three resolutions. The individual points show the deconvolved FWHM Φ. These deconvolved measurements of Φ agree well where they overlap at different resolutions, showing that they are not biased noticeably by the finite beamwidths Φ_b. The curve shows the isophotal width ϕ to the 0.45 mJy per beam contour, minus twice the FWHM of the beam. (This corrects the isophotal widths for the finite beamwidth to a first approximation which is adequate for our purposes in the central and outer jet, where the correction is small).

It is clear that the jet does not expand at a constant rate, as would a steady, free (unconfined) jet. Between the brightness minimum at $\Theta \approx 10''$ (~ 4.3 kpc from the core) and the point at $\Theta = 20''$ (~ 9 kpc from the core) the jet widens rapidly. It then expands more slowly and, on a small scale, oscillates in radius, until ~180″ (80 kpc) from the core, where it again expands rapidly. This reexpansion beyond 180″ from the core

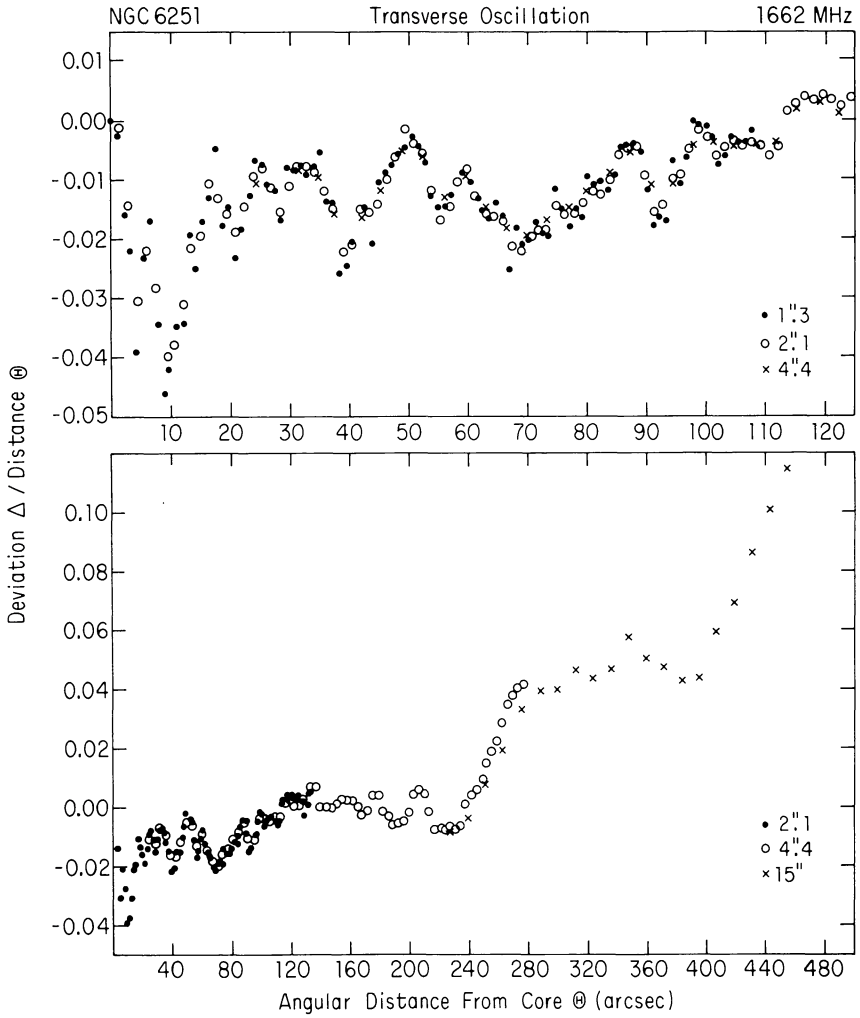

FIG. 7.—Deviation Δ of the ridge line of the jet from an axis with position angle 296°.4, normalized by angular distance Θ from the core, as a function of Θ. The ratio Δ/Θ measures the angular deflection of the jet from the fiducial position angle, as seen from the core. *Upper panel*: data for $\Theta < 120''$ at three resolutions. *Lower panel*: data for $\Theta < 460''$ at three resolutions. The noise in these plots decreases from left to right, as a result of the normalization by Θ. The scatter between adjacent points indicates the noise in that part of the plot.

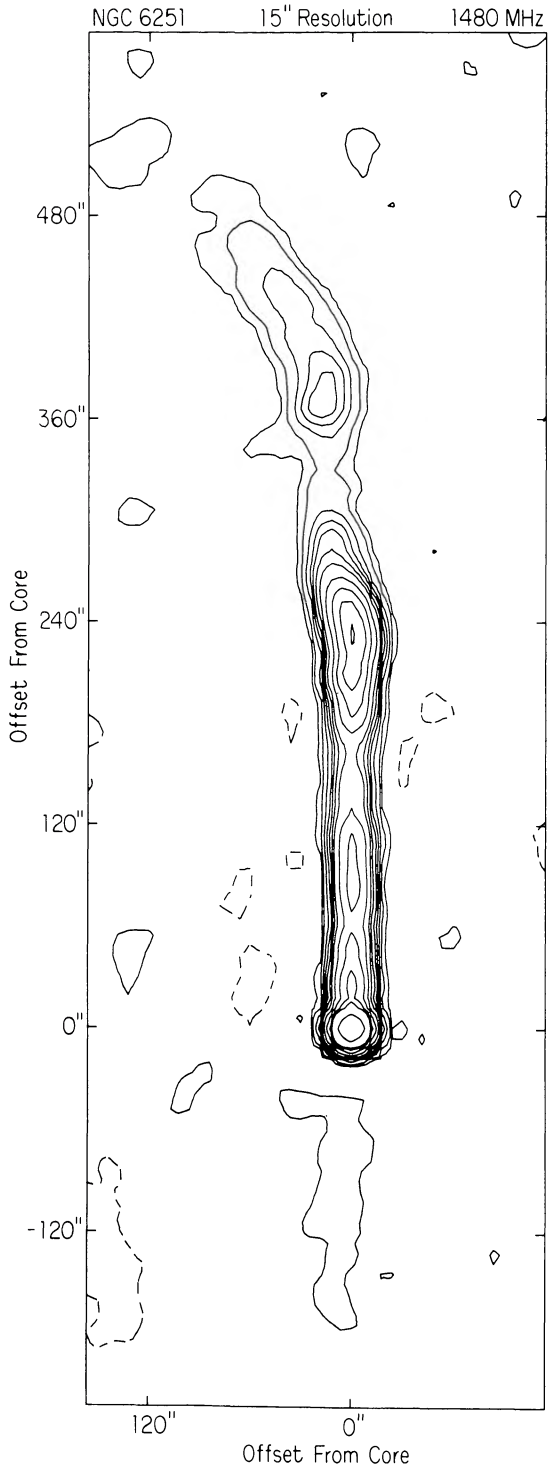

FIG. 8.—Rotated map of 8′ (~ 200 kpc) of the jet at 1480 MHz with 15″ resolution, showing the transverse oscillation, the bulk displacement of the lower contours, and the very weak counterjet within 150″ of the core on the side away from the main jet. Contours are drawn at −1.18 (*dashed*), 1.18, 2.36, 4.72, 7.08, 9.44, 13.0, 17.7, 29.5, 47.2, 70.8, 94.4, and 236 mJy per beam. The highest contour delineates the FWHM of the beam around the peak of the core source.

coincides with the end of the faint central region of the jet, with its general rebrightening, and with the appearance of asymmetric knotty substructure. The initial slowing of its expansion occurs around 20″ (~ 9 kpc) from the core, but this is followed by oscillations in the expansion rate. The oscillations produce an appearance of "steps" in the expansion, e.g., the generally slow expansion between 40″ and 90″ (17 and 40 kpc) from the core. The lower panel of Figure 10 shows the 1662 MHz intensity along the ridge line of the jet at 4.″4 resolution, to assist relation of the features of its expansion to those of its intensity variation.

Note that the large oscillations of the FWHM data at $\Theta > 120''$ anticorrelate with oscillations of the peak intensity in the knotty substructure of the outer jet. Because this substructure has very asymmetric transverse brightness profiles (see Fig. 9), the FWHM Φ does not describe the shape of the profiles well at these distances from the core. Figure 10 shows that the isophotal width ϕ varies more smoothly (and monotonically) than the FWHM Φ with distance from the core in this knotty substructure.

Figure 11 shows the inner 120″ (~ 50 kpc) of the expansion in more detail, using FHWMs derived from the 1662 MHz data at 1.″3 and 2.″1 resolution. Note the oscillations in the FWHM (expansion and contraction of the brighter features of the jet) between 60″ and 110″ from the core. Note also the slowing of the initially rapid lateral expansion near $\Theta = 18''$ (~ 8 kpc from the core).

The large-scale collimation behavior shown in Figures 10 and 11 is similar to that of the jets in NGC 315, 3C31, and 3C449, which also expand most rapidly a few kpc from their radio cores (Willis *et al.* 1981; Bridle *et al.* 1980; Perley, Willis, and Scott 1979; Bridle 1982), then slow down and (in the case of NGC 315) ultimately reexpand. We interpret this behavior in § VII*a*.

e) *Is the Jet Ever Center-darkened?*

The map of the jet with 18″ by 2″ resolution at 5 GHz shown by Saunders *et al.* (1981; their Fig. 3) contains transverse emission profiles in the fainter central region ($120'' < \Theta < 180''$) that are center-darkened. Saunders *et al.* note that this effect could either be an artifact of uncompensated atmospheric phase irregularities in their data, or a real concentration of the synchrotron emissivity toward the outside of a hollow cylinder in this region of the jet. There is no sign of center-darkening in this region in any of the VLA maps (see Fig. 3, for example), which have sensitivities and resolutions across the jet equal to, or better than, that of Saunders *et al.* Figure 9*d* shows a typical transverse profile through our 1662 MHz data in the region where theirs showed evidence of center-darkening. We infer that the apparent center-darkening noted by Saunders *et al.* was probably an artifact of phase errors in their data, as they suggested.

There is, however, a center-darkened knot (or cluster of knots) 18″ (7.7 kpc) from the core in our highest resolution 1662 MHz map (see Fig. 4). This feature is immediately on the coreward side of the first slowdown of the lateral expansion. Its center-darkening is responsible for the "overshoot" in the FWHM data at $\Theta = 18''$ (see Fig. 11). Section VII*a* suggests an interpretation for this unusual feature.

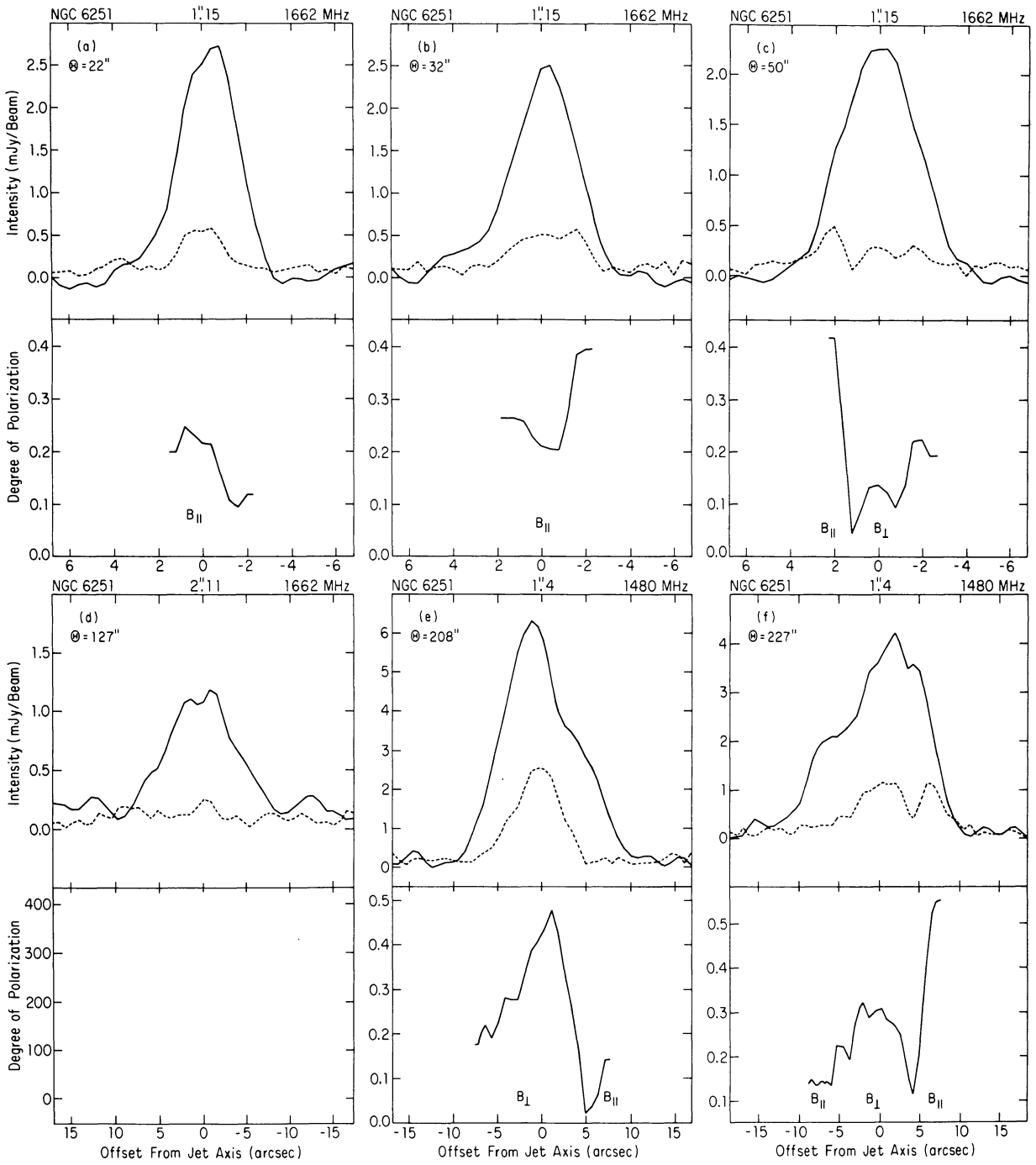

FIG. 9.—Sample transverse intensity profiles at various locations along the jet, from the 1662 MHz data at 1".15 and 2".11 resolution and the 1480 MHz data at 2".11 resolution. The upper panels show the total and polarized intensities (full and dotted curves, respectively); the lower panels show the degrees of linear polarization only in regions where the error in this quantity is $< \pm 0.1$. The profiles are taken at angular distances Θ from the core of 22", 32", 50", 127", 208", and 227", respectively.

f) The Brightness of the Counterjet

We have searched for emission to the southeast of the radio core along the projected axis of the main jet (i.e., along P.A. 116°.4) within 4'.4 of the core on all of the VLA maps. In both NGC 315 and 3C31 the fainter "counterjets" expand more rapidly than the main jets (Willis *et al.* 1981; Bridle *et al.* 1980), so our most significant new data on the counterjet emission in NGC 6251 are those derived from the 1480 MHz map at 15" resolution (Fig. 8) and from the 1446 and 1662 MHz D-configuration "snapshots" at 50" resolution.

Figure 12 shows the 1446 MHz snapshot map at 50" resolution. A weak counterjet extends for ~130" (~56 kpc) from the core along P.A. 116°. The counterjet appears on this

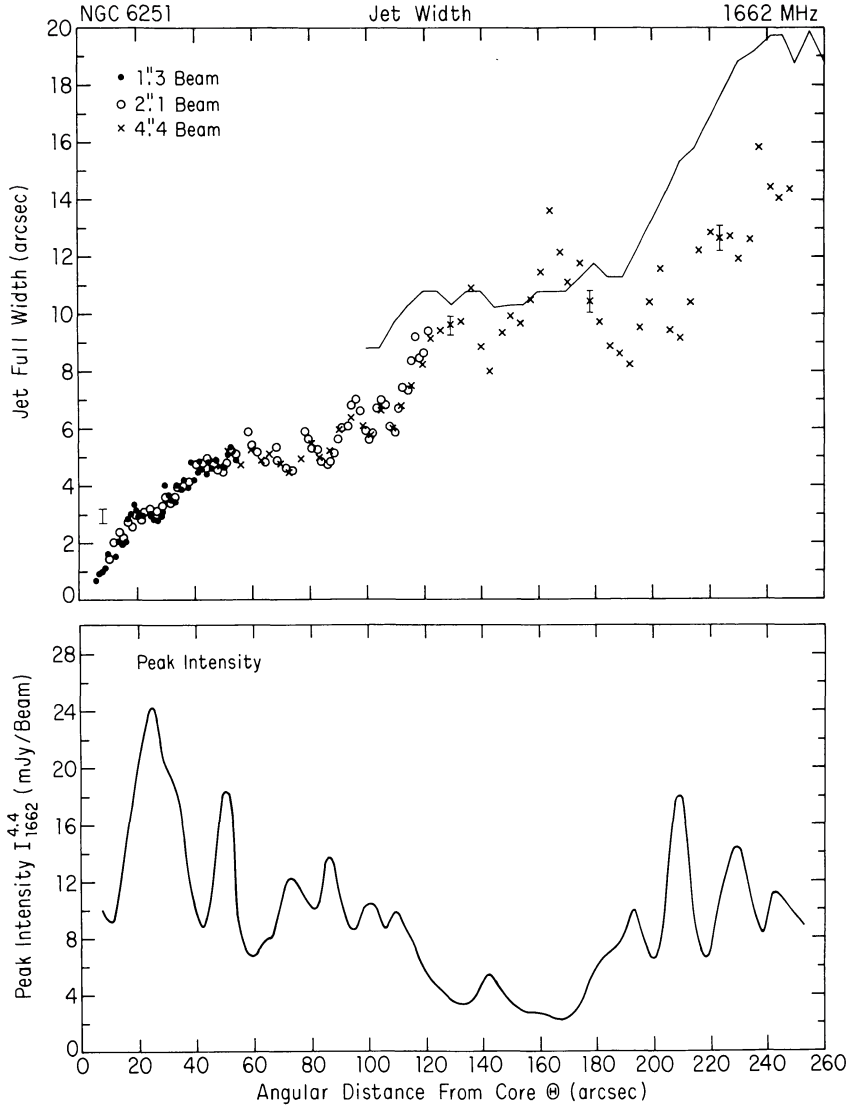

FIG. 10.—*Upper panel*: collimation properties of the first 250″ of the jet. Individual points show the deconvolved FWHM Φ from the 1662 MHz data at the resolution indicated. Typical errors are shown by the vertical bars. The continuous line shows the full width ϕ between the 0.45 mJy per beam contours at 1662 MHz, minus twice the FWHM of the instrumental beam. Note the smooth variation of the isophotal width ϕ relative to that of Φ, beyond $\Theta \sim 100''$. *Lower panel*: intensity profile along the ridge line of the jet at 4.″4 resolution, from the 1662 MHz data at 4.″4 resolution.

map at all stages of reduction, both before and after self-calibration. It is therefore not an artifact of the self-calibration procedure, and its detection independently confirms the reality of the counterjet emission in the WSRT 610 MHz map shown as Figure 1. The ratio between the peak intensities of the main jet and the counterjet 100″ from the core on this map is 30:1. The corresponding ratio on the 1662 MHz map is 45:1, and that on the WSRT 610 MHz map is 40:1. We conclude that the intensity ratio between the main jet and the counterjet 100″ from the core is ~ 40:1 at 50″ resolution.

This ratio varies with distance from the core, however. For example, we detect no 1446 MHz emission at 50″ resolution near the location 240″ along the extrapolation of the counterjet corresponding to the rebrightening of the outer main jet. At this resolution the outer main jet 240″ from the core is as bright as the emission within 90″ of the core. Any proportional enhancement of the counterjet corresponding to this rebrightening of the main jet would be readily detectable. Integrations over several beam areas show that the *average* intensity ratio between the main jet and the counterjet is greater than or equal to 200:1 by 240″ (~ 100 kpc) from the core component. The corresponding ratio from the WSRT 610 MHz map (Fig. 1) is greater than or equal to 250:1.

Figure 8 has a (barely) significant elongated feature in the region where the counterjet is detected at 50″ resolution. At this 15″ resolution the main jet has greater than or equal to 50 times the brightness of the counterjet at 100″ from the radio core, and the counterjet is resolving.

These variations in the brightness ratio between the jet and the counterjet show that the counterjet is not simply a fainter replica of the main jet. They also explain why the counterjet was not detected by 1417 MHz observations with the One-Mile

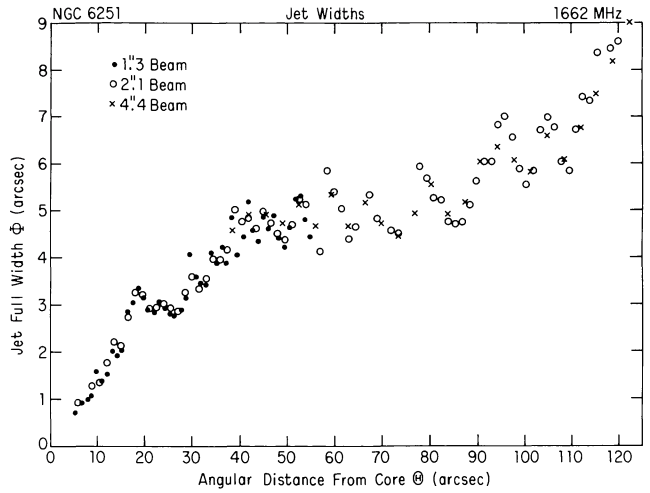

FIG. 11.—Collimation properties of the inner 125″ of the jet. The points show the deconvolved FWHM Φ from the 1662 MHz data at the indicated resolutions.

Telescope (Waggett, Warner, and Baldwin 1977). The rapid dimming of the counterjet beyond 100″ from the core would have made it difficult to detect in these observations. Our 1446 MHz data show that the ratio of the integrated intensities of the main jet and counterjet within 250″ of the core is 130:1. The observations by Waggett *et al.* would have had sufficient sensitivity to detect the counterjet only within one of their beamwidths of the core component, where such detection would have required high dynamic range. The observations of this region with 3.″7 resolution at 2.7 GHz by Saunders *et al.* will have resolved the counterjet so that it was well below the noise and ripple on their map.

g) *Luminosity Evolution of the Jet*

Since both the magnetic field strengths and the relativistic particle energies in an expanding laminar jet should decrease with distance from the active core (see §§ VII*c*, VII*d* below), it is of interest to examine how the luminosity of the jet varies (*a*) with distance from the core and (*b*) with the width of the jet. To examine the *global* behavior of the luminosity (as opposed to fluctuations arising from changes in the shape of the transverse intensity profiles) we discuss first the evolution of the *spectral luminosity per unit length* of the jet. We estimate this from the 1662 MHz maps by integrating the transverse intensity profiles over the width of the jet.

Figure 13 shows how the 1662 MHz luminosity per unit length varies with angular distance Θ from the radio core over the first 400″ of the jet. There are local fluctuations of order 2:1 in the luminosity per unit length over the first 180″ (77 kpc), but only about a twofold *large-scale* decrease in spectral luminosity per unit length over this region, despite the fact that over the same region the FWHM grows by a factor of almost 10. For Θ = 160″ to 260″ the luminosity per unit length *increases* from $\sim 4.3\times10^{21}$ to $\sim 2.6\times10^{22}$ W Hz^{-1} kpc^{-1}, with large local fluctuations in the knotty substructure (see Fig. 3). Even excluding the behavior in this region, the spectral luminosity per unit length of the jet as a whole decreases by only a factor of 4 over a region where the jet widths increase by a factor of ~ 35.

Figure 14 (*left panel*) plots the peak brightness I_ν of the transverse profiles against their deconvolved FWHMs Φ over the inner 120″ of the jet (where most of these profiles are symmetric and the jet is straight) using our 1662 MHz data at 1.″3 and 2.″1 resolution. The structure at Θ < 9″ is not well enough resolved for the $I_\nu(\Phi)$ data to be reliable, so the plots

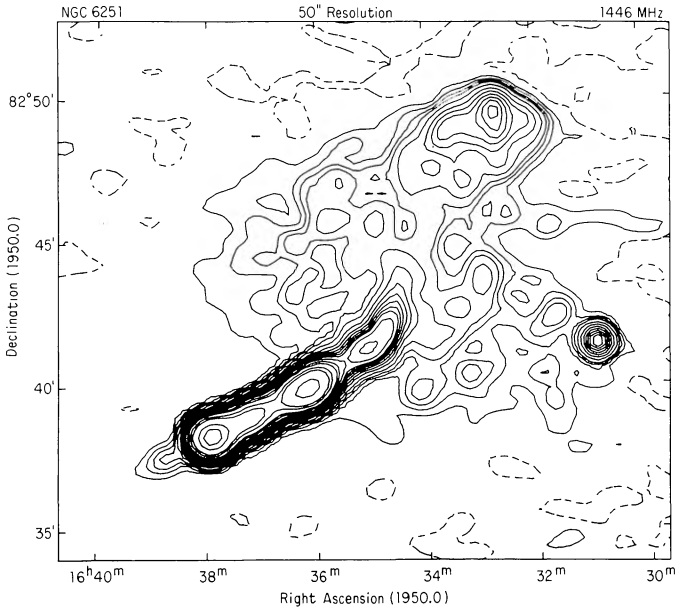

FIG. 12

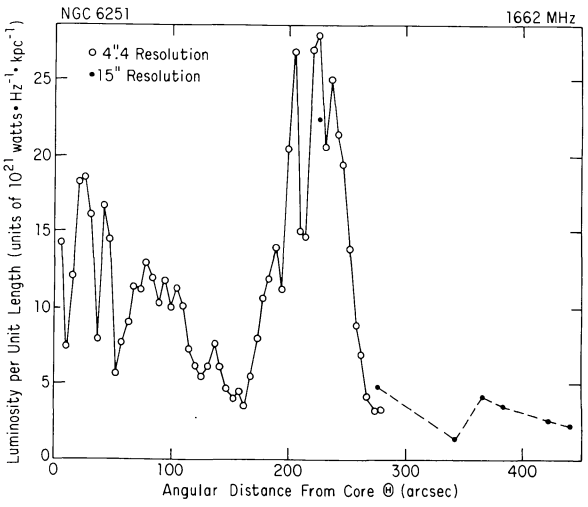

FIG. 13

FIG. 12.—Unrotated map of the jet and northwest lobe from the 1446 MHz data at 50″ resolution, showing evidence for the counterjet, independent of that in Figs. 1 and 8. Contours are drawn at −1.33 (*dashed*) and +1.33 mJy per beam, then at 2.66, 3.99, 5.32, 7.98, 10.6, 13.3, 16.6, 20.0, 23.3, 26.6, 30.0, 33.3, 40, 66.5, 100, 133, 266, and 400 mJy per beam.

FIG. 13.—Spectral luminosity per unit length of the jet at 1662 MHz plotted against angular distance Θ from the radio core. Note the local fluctuations and the increase in luminosity per unit length beyond 180″ from the core.

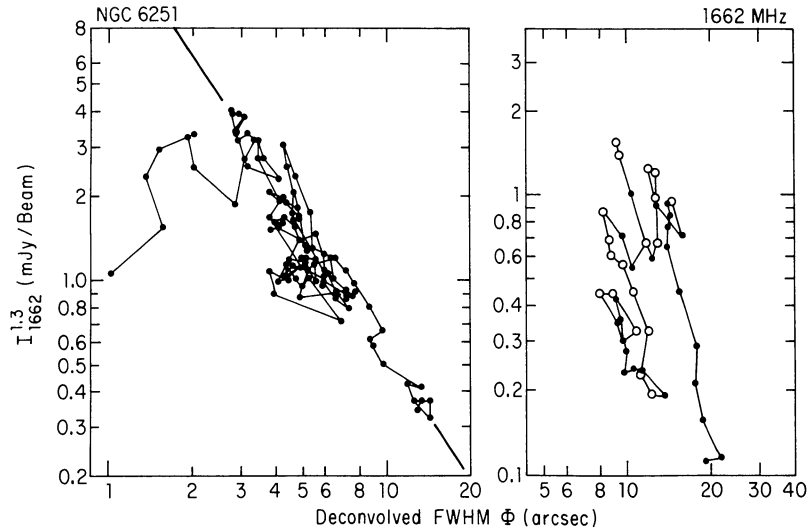

FIG. 14.—Peak profile intensity I_ν at 1662 MHz plotted against deconvolved FWHM Φ of the jet. *Left panel*: the first 120″ of its length, using data at 1.″3 and 2.″1 resolution. The thick line shows a $\Phi^{-1.5}$ law. *Right panel*: the region beyond 120″ from the core, using data at 4.″4 resolution. Points obtained from regions of the jet where I_ν is increasing with distance are shown as open circles. In both panels the scale of I_ν has been normalized to mJy per beam area at 1.″3 resolution.

begin with $\Phi \approx 1''$. The peak brightness I_ν *in*creases with Φ for $9'' < \Theta < 13''$, then decreases as $\Phi^{-1.5}$ for $13'' < \Theta < 17''$. A rapid increase of I_ν with Φ until $\Theta = 20''$ is followed by an extensive region over which $I_\nu = \Phi^{-1.5 \pm 0.2}$ on average, with occasional significant local deviations from this trend in the knots. The region at $47'' < \Theta < 60''$, containing the bright knot at $\Theta = 50''$, is the longest section of the inner jet over which the $I_\nu(\Phi)$ relation deviates significantly from this average behavior. In the knot itself, $I_\nu \propto \Phi^{-3.8}$ on both its coreward and its lobeward sides, while $I_\nu \propto \Phi^{-1.0}$ in the fainter emission preceding and following the knot. Outside this anomalous region, the mean ($I_\nu \propto \Phi^{-1.5}$) brightness-width relation holds whether I_ν is increasing or decreasing with distance from the core. The discrepancies between this *average* behavior and the brightness-width law expected in simple adiabatic expansions are interpreted in § VII*d*.

The corresponding plots for the central and outer regions of the jet ($\Theta > 120''$) at 4.″4 resolution (Fig. 14, *right panel*) show that the average slope of the $I_\nu(\Phi)$ relation increases with distance from the core in these regions. The central ($120'' < \Theta < 180''$) section of the jet has $I_\nu \propto \Phi^{-2.2}$ on average. The knots at $\Theta \approx 190''$ and $\approx 210''$ have $I_\nu \propto \Phi^{-2.6}$ and $\Phi^{-3.4}$, respectively, on both their coreward and lobeward sides. There is little correlation between I_ν and Φ on the *core*ward side of the knot at $\sim 230''$ from the core, but its *lobe*ward side has $I_\nu \propto \Phi^{-4.5}$. Note also that the various *segments* of the $I_\nu(\Phi)$ plot in the outer jet do not superpose on one another, as they do in the inner jet. Rather, at $\Theta = 174''$, 202″, and 220″ there are *sudden* increases in intensity in regions of increasing Φ which cause nonalignment of the various segments of the plot.

Figure 3 shows that the knots in the outer jet are a series of bright asymmetric peaks superposed on smoother low-level features. This is also illustrated by the contrasting behavior of the FWHM and isophotal width plots for the outer jet (Fig. 10). The FWHMs Φ derived from the Gaussian fits to these complex structures are only crude descriptions of their transverse profiles, particularly on the steepest brightness gradients. The details of the $I_\nu(\Phi)$ relation in the outer jet must therefore be interpreted cautiously, although the trend for its slope to increase with distance from the core is certainly significant.

V. POLARIZED INTENSITY PROPERTIES

a) Degree of Linear Polarization

Figure 15 plots the degrees of linear polarization at 1662 MHz (p_{1662}) along the jet at 2.″1 (0.9 kpc) resolution. The zero-level bias in the map of polarized intensity $P = (Q^2 + U^2)^{1/2}$ (Wardle and Kronberg 1974) has been corrected in deriving this map of p_{1662}, and in all other maps of the degree of polarization referred to below.

For the first 27″ (12 kpc) from the core (Fig. 15, *left panel*) p_{1662} is mainly in the range 20%–50%, its highest values occurring in the first 10″ of the jet. There is little transverse structure in the degree of polarization at these distances from the core. Between ~ 27″ and 90″ (~12 and ~ 40 kpc from the core) p_{1662} is generally a minimum at the center of the jet, taking values less than 5% in many places beyond $\Theta = 40''$. The degree of polarization at the edges of the jet is typically 20%–30% in this region. Beyond 90″ from the core, p_{1662} rises in the center of the jet, becoming more typically 20%, while at the edges of the jet it decreases to ~ 5%–10% (*center panel*). At this resolution the polarized intensity approaches the noise level on the maps ~150″ (65 kpc) from the core, but reappears ~170″ (73 kpc) from the core. The data at 4.″4 resolution show that the average value of p_{1662} in this region is 10%–20%.

In the "outer" region beyond 180″ from the core, p_{1662} has a complex structure (Fig. 15, *right panel*). From $\theta \sim 180''$–210″ the maximum degree of polarization generally occurs near the center of the jet, and is typically 20%–30%. Further from the core, the axis of the jet has regions of both high (> 40%) and

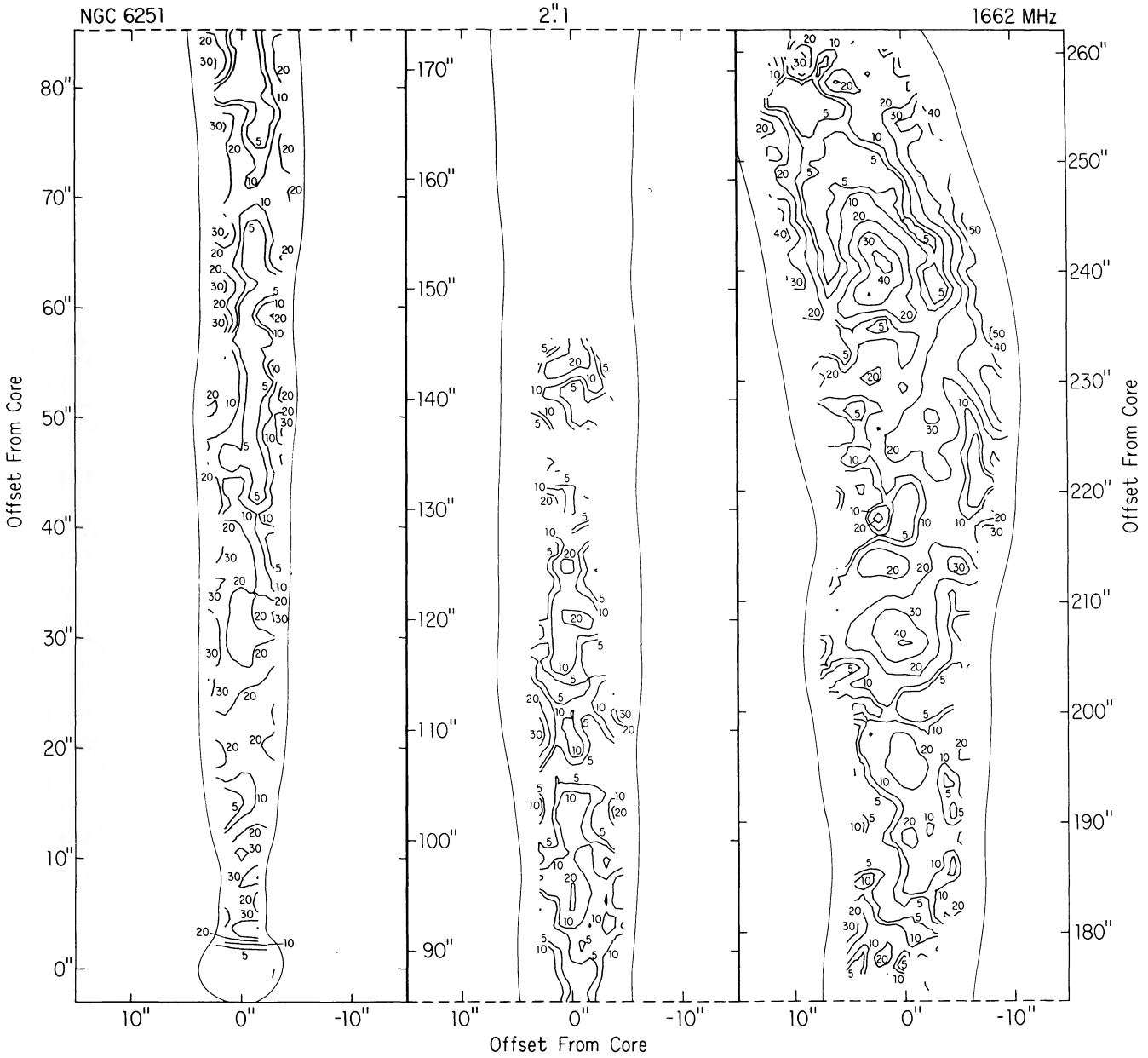

FIG. 15.—Contour plot of the degree of linear polarization p_{1662} at 1662 MHz at 2".1 resolution. Data have been excised wherever the error in p_{1662} was $> \pm 0.1$.

low (< 5%) polarization, while p_{1662} at the edges of the jet reaches 40%–50%. In many places the degree of polarization has a double-trough structure—the center of the jet is 30%–40% polarized and is bordered on both sides by minima reaching to less than 5%. These double troughs are related to a change from transverse to axial magnetic field across the jet (see § V*c* below).

The *maximum* value of p_{1662} seen in the transverse profiles *decreases* from ~ 50% for the first 10" or so along the jet, remains at ~ 20% for the next ~180" (~ 75 kpc), then increases to 40%–50% in the highly expanded outer regions of the jet. The maxima in the outer jet are generally on its edges, except for two strongly polarized knots on the axis ~ 205" (88 kpc) and 240" (103 kpc) from the core.

Figure 16 plots p_{1662} along the ridge line of the inner 180" of the jet at 2".1 resolution. There are alternate regions of increasing and decreasing degrees of polarization, resembling the polarization "oscillations" along the ridge line of the jets in 3C31 (Fomalont *et al.* 1980). The degrees of polarization at the base of the jet in NGC 6251 greatly exceed those of 10%–15% at comparable distances from the core in both 3C31 and NGC 315 (Fomalont *et al.* 1980), however.

The values of p_{1370} and p_{1480} track those of p_{1662} to within the errors of measurement. Those of p_{4885} generally follow

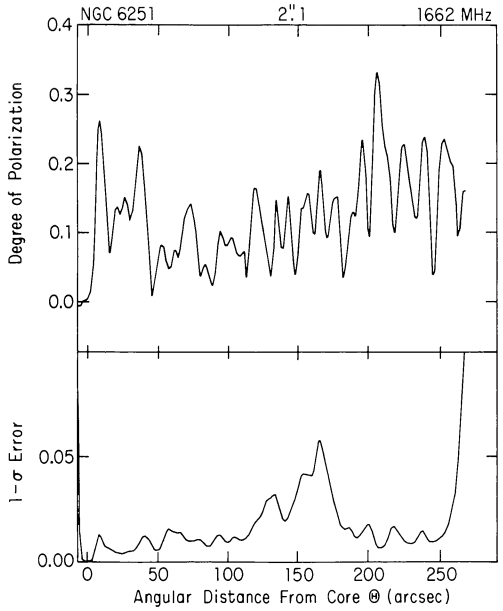

FIG. 16.—Profile of the degree of linear polarization at 1662 MHz at 4".4 resolution along the ridge line of the jet. The lower panel shows the error in the degree of polarization as a function of angular distance from the core.

p_{1662}, except that at 4".4 resolution p_{4885} is generally higher in the region from 20" to 70" from the core, as reported previously by Willis *et al.* (1981). In this region, however, we find that the depolarization ratio $D = p_{1662}/p_{4885}$ increases toward unity as the instrumental resolution is increased. This variation of D with resolution, together with the rotation measure maps (§ V*b*), provides strong evidence that the depolarization noted by Willis *et al.* (1981) at 4".4 resolution is due to differential Faraday rotation across the beam, rather than to thermal material in the jet. In the outer jet p_{1662}/p_{4885} is within errors of 1.0 at all locations and all resolutions.

We remind the reader that very high signal-to-noise ratios are needed to measure depolarization accurately. If P_1 and P_2 are the polarized flux densities, and δ_1 and δ_2 are their errors, at frequencies ν_1 and ν_2, respectively, the lower limit to the error δD in the depolarization is

$$\delta D = D\left[(\delta_1/P_1)^2 + (\delta_2/P_2)^2\right]^{1/2} \quad (1)$$

Thus, to determine the depolarization D at any point along the jet to an accuracy of 10% ($\delta D = 0.1$), a signal-to-noise ratio of 15:1 or better is required on *both* polarized intensity maps at that point. This is difficult to achieve, except in strongly polarized or very bright sources. Furthermore, when many individual values of D with lower signal-to-noise ratio are averaged (to obtain more stable estimates) the polarized flux densities *must* be corrected for the bias of the Ricean distribution at low signal to noise (Wardle and Kronberg 1974). If this is not done, the resulting estimates of D are biased toward false depolarization at the frequency at which the data were less noisy. Taking these effects into account, we find no *convincing* evidence for internal depolarization between 1370–1662 and 4885 MHz anywhere in the jet.

b) Rotation Measure

Figure 17 shows the distributions of the E-vectors over the first 240" of the jet with a resolution of 4".4 (1.9 kpc) at all four frequencies. Two properties of these distributions are noteworthy:

1. Beyond ~ 90" (~ 40 kpc) from the core, the 1480 MHz E-vectors are rotated by an average of $90° \pm 30°$ from the 4885 MHz position angles.

2. Within 90" of the core, there are much larger variations in the position angle differences between these two frequencies. Between 15" and 50" (6 and 21 kpc) from the core, the 1480 MHz position angles also change systematically *across* the jet, whereas the 4885 MHz vectors are roughly uniform.

Because maps of E-vector position angle χ at two frequencies do not define the distribution of the Faraday rotation measure (RM) uniquely, the 1370 and 1662 MHz observations were made primarily to study the RM variations in the inner parts of the jet from maps of the E-vector position angle χ at the three closely spaced frequencies of 1370, 1480, and 1662 MHz. (In the absence of noise, RMs can be determined unambiguously over a range of 220 rad m^{-2} between 1370 and 1480 MHz.) Figure 18 shows the distributions of the E-vectors over the base of the jet at 1662 and 1370 MHz at 1".4 resolution, to demonstrate the complexity of the rotation in this region directly.

We determined the RM distribution over the jet by fitting the values of χ from corresponding cells in the maps at all four frequencies to a λ^2 law of rotation using a linear least-squares regression algorithm. Figure 19 shows sample plots of the position angles χ against λ^2 at selected locations along the jet. These locations are identified with black dots in Figure 20. There are good fits to the λ^2 law of rotation for negative RMs in the range from -10 to -135 rad m^{-2}, depending on location. Similarly good fits to the λ^2 law were found throughout the jet.

Figure 20 shows the distribution of the RM over the first 290" of the jet at 4".4 resolution. The RM map was derived only from those four-frequency χ-λ^2 fits for which (*a*) the correlation coefficient of the fit exceeded 0.95 and (*b*) all four values of χ were accurate to better than 30°, while two values were accurate to better than 20°. Before contouring, the RM distribution was inspected for locally discrepant values. Such values were excised, and the contours were instead interpolated between more distant RM values derived from more accurate values of χ. These restrictions and the filtering procedure were necessary to resolve ambiguities in the RM fits in the presence of noise in the polarization data, while preserving consistency among adjacent values of the derived RMs.

Figure 20 (*left panel*) shows contours of the RM in the region within 140" of the core; beyond this there is little systematic structure in the RM, so local values rather than a contour map are shown in the right panel. The RM values in this panel are shown at intervals of 5".25, except where a value on this uniform grid failed to meet the selection criteria described above. In such cases, the closest reliable value is shown at its actual location. Figure 20 demonstrates the following:

1. The RM is -49 rad m^{-2} to within the measurement errors everywhere beyond ~180" from the core. The mean of

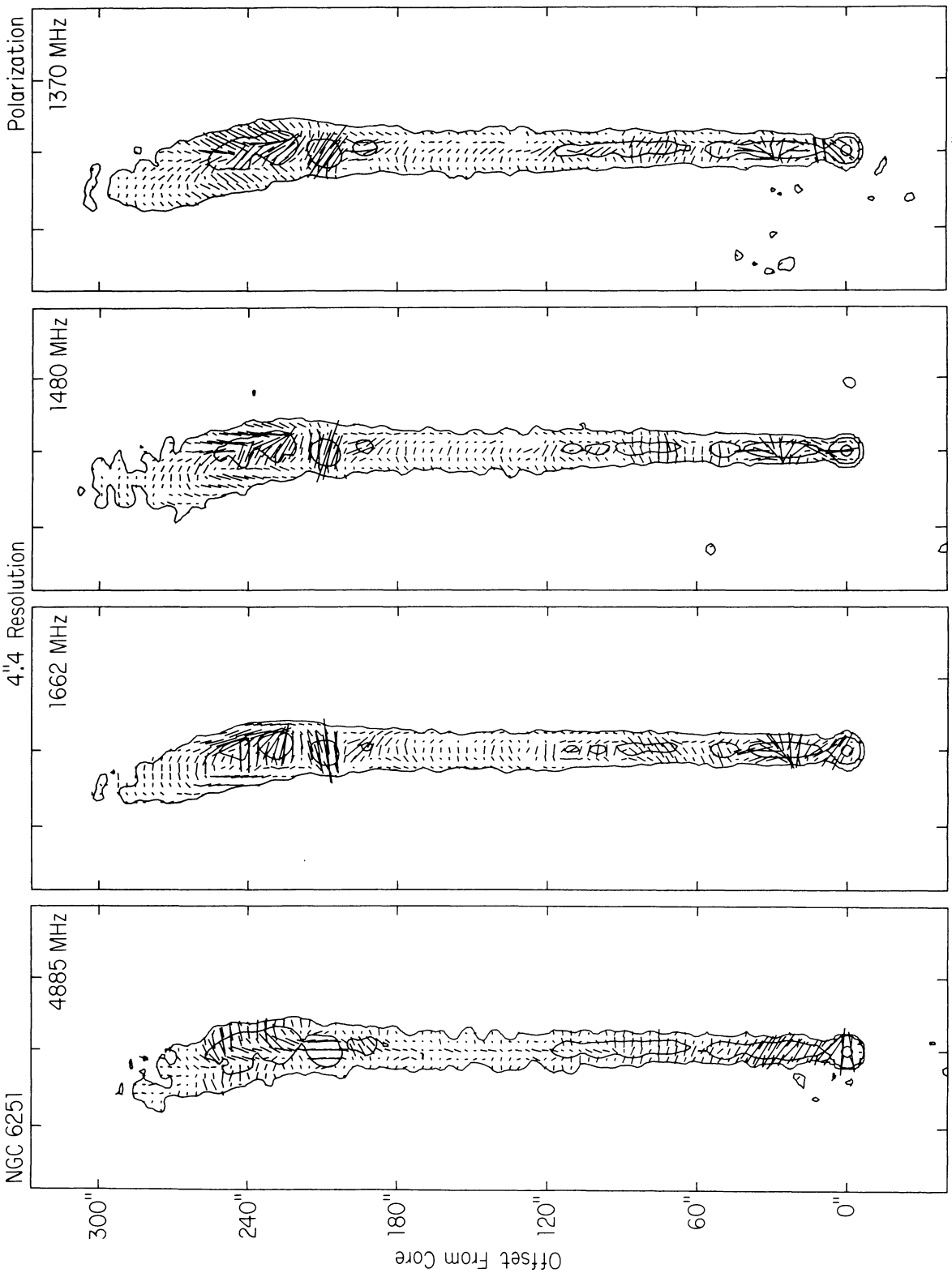

FIG. 17.—Distributions of E-vectors over the entire jet at 4".4 resolution at all four frequencies. The lengths of the vectors are proportional to the polarized intensities, with scales of 6.4, 4.6, 3.7, and 3.9 arcsec mJy^{-1} in the 4885, 1662, 1480, and 1370 MHz maps, respectively. The vectors in the 4885 MHz map are close to the noise limit in the central part of the jet.

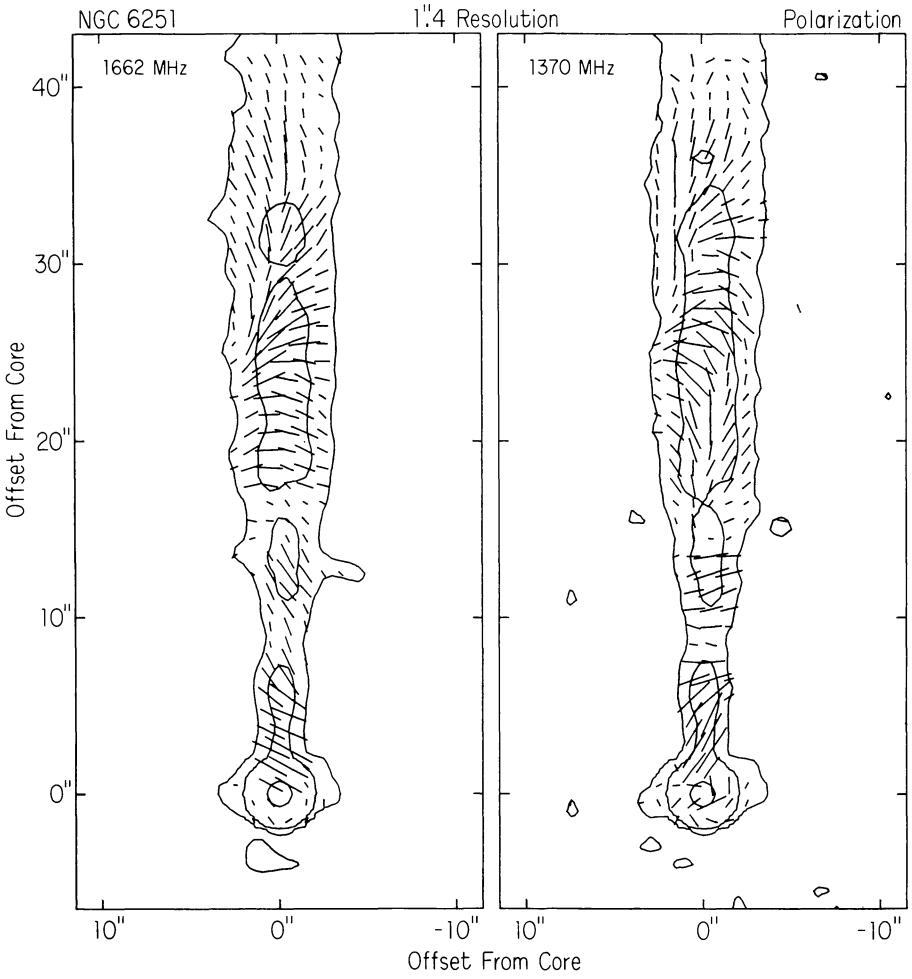

FIG. 18.—Distributions of E-vectors over the inner ~ 40″ of jet at 1″.4 resolution at 1662 MHz (*left panel*) and 1370 MHz (*right panel*). The vector scales are 2.13 and 2.19 arcsec mJy^{-1} for 1662 and 1370 MHz, respectively.

the RMs found at 123 locations where the signal-to-noise ratio of the polarized intensity was greater than or equal to 12:1 at *each* of the four frequencies is -48.9 ± 0.2 rad m^{-2}. The fluctuations of the RM values plotted in this region are due mainly to noise in the data.

2. There are very strong gradients *along* the jet between RMs of -10 and -130 rad m^{-2} in the inner 50″ (~ 20 kpc). The most negative RMs occur within 20″ (~ 9 kpc) of the center of NGC 6251.

3. Between ~ 40″ and ~ 70″ (~ 17 and ~ 30 kpc) from the core there are steep RM gradients *across* the jet; on the northern (*left*) edge the RM is typically -70 to -80 rad m^{-2}, while on the southern edge it is typically -10 to -50 rad m^{-2}. The RMs on the southern edge become steadily more negative over this region, however, so that at 75″ from the core the entire jet has an RM of -70 to -80 rad m^{-2}.

Figure 21 shows details of the RM distribution at 2″.1 resolution over the inner ~ 58″ of the jet. At this resolution we also see steep RM gradients across the jet in the region 15″ to 25″ from the core. The north edge has RMs fluctuating wildly in the range -50 to -100 rad m^{-2}, while the south edge has relatively constant RMs in the range -90 to -120 rad m^{-2}. The RM gradients across the jet here are thus of the *opposite sign* to those further from the core noted above.

Note from Figure 21 that there are many parts of the inner jet where RM differences greater than or equal to 50 rad m^{-2} occur over scales of ~ 5″. RM gradients of this magnitude will cause strong differential rotation across the beamwidths of the WSRT and Cambridge telescopes at frequencies below 2000 MHz. The depolarization found at 30″ from the core by Saunders *et al.* (1981) on comparing 610 and 2700 MHz data at 1′ resolution can be explained entirely by this effect. The electron density in the inner jet estimated from the apparent 610 MHz depolarization by Saunders *et al.* is therefore invalid.

We interpret the RM distribution in detail in § VII*b* below.

c) Projected Magnetic Field Structure

Maps of the projected magnetic field configuration were derived from the four-frequency χ-λ^2 distributions. The zero-wavelength intercept of the four-frequency χ-λ^2 variation was used to obtain the intrinsic E-vector position angle $\chi(0)$ at each map point. The zero-wavelength E-vectors were then rotated through 90° to map the projected B-vector distri-

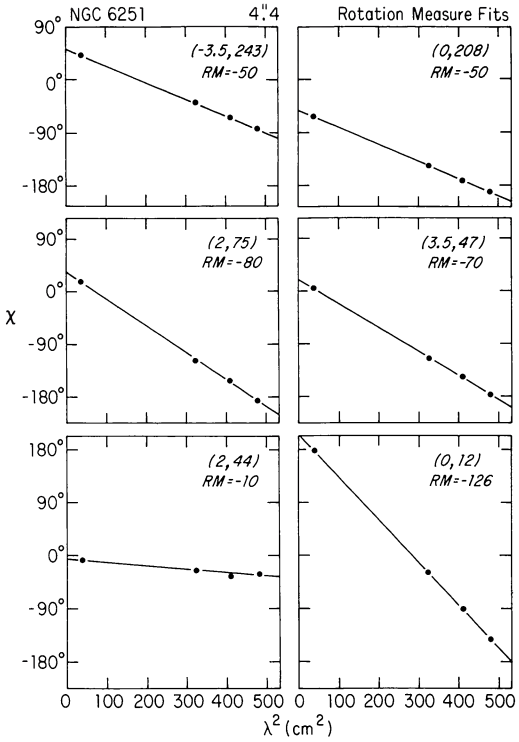

FIG. 19.—Plots of E-vector position angle χ vs. λ^2 at six locations along the jet, from the data at 4".4 resolution. The locations are identified by their offsets from the core in arc seconds (see also Fig. 20). The RM value inferred from each plot is given in rad m^{-2}. The errors in the position angles are comparable to, or smaller than, the sizes of the dots.

bution. Figure 22 shows the B-vector map at 4".4 resolution. Vectors are displayed only where the values of the E-vector position angle χ were accurate to less than 15° at all four frequencies. This restriction prevents the appearance of false "turbulence" in the B-vector distribution due to noise in the polarization position angle data.

The magnetic field is predominantly longitudinal (i.e., parallel to the jet axis) for the first 90" (~ 40 kpc) from the core, both at the center and at the edges of the jet. Such longitudinal ($B_{\parallel}$) configurations have often been found over the first (and brightest) ~10% of the lengths of the jets in low-luminosity radio galaxies and over the entire lengths of jets in more powerful sources (Bridle 1982). There are regions in the center of this jet between 20" and 40" from the core where the projected field is, however, as much as 45° from the axis of the jet. There is a second anomalous region of oblique field near the peak of the bright knot at $\Theta = 50''$. Figure 23 shows these field structures at higher resolution (2".1). At this resolution the field near the jet axis at $\Theta = 50''$ is almost perpendicular to the jet.

Adjacent vectors in these field maps are well ordered, and the deviations from strictly longitudinal field are well above the uncertainties due to noise in the correction for the RM. It is important to recognize that, although the regions of oblique field coincide with those of steep RM gradients (see Fig. 21), the field misalignment is not an artifact of our correction for the effects of the RM. This can be seen from the 4885 MHz E-vector distribution shown in Figure 17, which shows the misalignment directly. The rotations needed to bring these 4885 MHz E-vectors to "zero wavelength" are between 1° to 20° throughout these regions; these rotations are much smaller than the observed deviations from pure longitudinal field.

In the outer 1' (~ 26 kpc) of the structure in Figure 22 the magnetic field is predominantly perpendicular to the jet axis ($B_{\perp}$) at the center of the jet and parallel to the axis ($B_{\parallel}$) at the edges. Such center-$B_{\perp}$, edge-$B_{\parallel}$ configurations have previously been seen in the more expanded parts of the jets in 3C31 (Fomalont *et al.* 1980) and in the counterjet and outer main jet in NGC 315 (Willis *et al.* 1981). The major change from dominant $B_{\parallel}$ to dominant $B_{\perp}$ on the axis occurs in the same region of the jet (~ 90" from the core) as the following:

1) The region where the central brightness I_{ν} declines most rapidly with distance Θ from the core;
2) The onset of the lateral reexpansion;
3) The termination of the central polarization minimum;
4) The stabilization of the RM at values close to those in the outer region of the jet.

The outer jet contains several knots in which the projected magnetic field configuration deviates substantially from the center-$B_{\perp}$, edge-$B_{\parallel}$ pattern which dominates this region. The field at the knot ~190" from the core is 40°–50° from the axis. The field at the knot ~ 210" from the core is 15°–20° from the axis in the other direction (see Fig. 23, *right panel*). At this knot the steepest brightness gradient (on its coreward side) is perpendicular to the projected field, however.

d) Equipartition Magnetic Field Strengths

We have computed the equipartition magnetic field strengths B_{eq} and energy densities u_{min} at various locations along the jet, assuming at each location a uniformly filled cylindrical geometry with its axis in the plane of the sky and a radius equal to the deconvolved Gaussian HWHM of the transverse intensity profile. In each case the radio spectrum was assumed to be a power law extending from 10 MHz to 10 GHz with the observed mean spectral index of 0.64. Equal energies were assumed to reside in relativistic protons and electrons, and the bulk velocity of the jet was assumed to be nonrelativistic. The validity of these assumptions (or of the principle of equipartition) anywhere along the jet is, of course, questionable. We therefore attach less significance to the absolute values of the derived magnetic fields than to the form of their variation along the jet.

Figure 24 shows the variation of B_{eq} with the deconvolved 1662 MHz FWHM Φ over the inner jet from Figure 10. The values of B_{eq} have been determined at the local maxima and minima of intensity along the jet, so that the scatter in Figure 24 represents the range of values of B_{eq} produced by the large-scale intensity fluctuations in the jet. Over most of the inner and central regions of the jet ($25'' < \Theta < 130''$) B_{eq} scales as $\Phi^{-0.73}$. The variation of B_{eq} with Φ is slower ($\sim \Phi^{0.0}$) in the inner 15" (6 kpc) of the jet. At the base of this region the peak intensities I_{ν} may be underestimated and the path length through the jet overestimated as the result of uncertainties in Φ caused by smearing with the instrumental beam. The

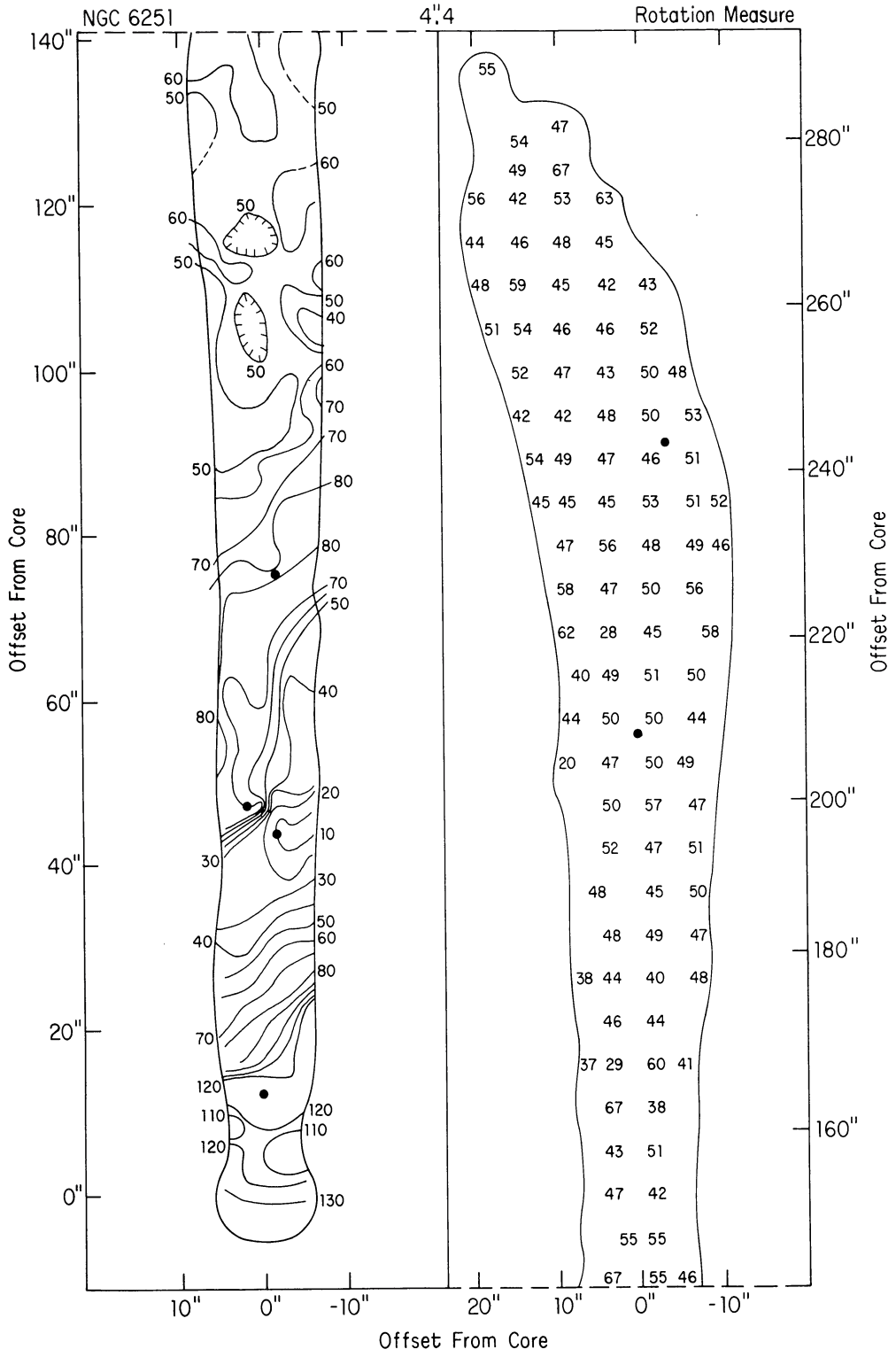

FIG. 20.—Distribution of RM (negative signs omitted) over the entire jet at 4".4 resolution. *Left panel*: contour map of RM fluctuations over the inner jet; dotted contours show regions where the detailed RM variation is poorly determined. *Right panel*: individual values in the outer jet; see the text for discussion of the grid selection. The dots show the locations for which the fits to the λ^2 law are plotted in Fig. 19.

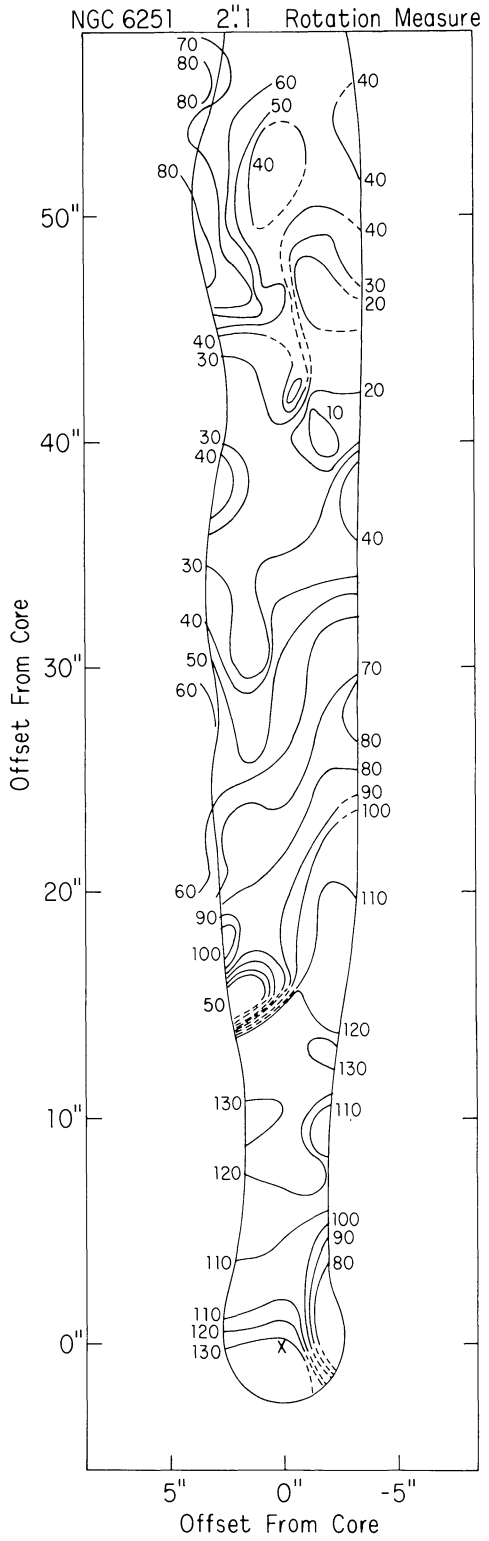

FIG. 21.—RM contour map (negative signs omitted) over the inner 60″ of the jet at 2″.1 resolution. Dotted contours denote regions where the detailed variation of the RM is uncertain.

resulting ~ 20% uncertainties in B_{eq} are not large enough to account for the slower $B_{eq}(\Phi)$ variation in this part of the jet, however.

Table 2 lists the equipartition field strengths and minimum energy densities at selected locations in the jet as a function of angular distance Θ from the core source. The locations are chosen to be at local maxima and minima of the intensity, to illustrate the local variability of these estimates made with the same assumptions at different positions along the jet.

VI. SUMMARY OF CHARACTERISTICS OF THE JET

Sections IV and V above discussed the principal features of the jet in total and polarized intensity. Figure 25 summarizes how the main parameters of the jet vary with angular distance Θ from the central core source over the first 300″ from the core.

In § IV*a*, we divided the first 4.′4 of the jet into three principal sections by the appearance of its total intensity distribution. These three sections are as follows:

1. *The "inner" jet* ($\Theta < 120''$, within ~ 50 kpc of the core), where its transverse intensity profiles (see Figs. 9*a*–9*c*) are symmetric, and it has substantial blobby substructure. This is also the regime (*a*) where the RM deviates substantially from the value of -49 rad m^{-2} it takes in the outer jet (see Fig. 20); (*b*) of predominantly longitudinal magnetic field on the jet axis (see Fig. 22); and (*c*) of the polarization minimum (trough) along the center of the jet (see Fig. 15). Over most of this region the central brightness I_ν of the jet declines with its FWHM Φ as $I_\nu \propto \Phi^{-1.5 \pm 0.2}$ (see Fig. 14).

2. At $90'' < \Theta < 120''$ (~ 40 to 50 kpc from the core) there is a transition from these properties to those of the *central "fading" regime* $120'' < \Theta < 180''$ (~ 50 to 80 kpc from the core), where the jet has no comparably bright knots, and a more rapid decline of central brightness with radius (see Fig. 14). In this region the RM also declines to its value in the "outer" jet (Fig. 20), and the projected magnetic field at the center of the jet becomes predominantly perpendicular to the axis (Fig. 22).

3. At $\Theta \geq 180''$ (beyond 77 kpc from the core) there is a transition to *the "outer" jet*, where the transverse intensity profiles are asymmetric (see Figs. 3, 9*d*, and 9*e*), and the blobby substructure reappears. This is the regime of the most complex polarization structure (Fig. 15), of *sudden* local re-brightening of the jet (Fig. 13), and of its strong transverse oscillation and deflection (Figs. 7 and 8). The brightness-radius relation in the jet away from the regions of sudden brightness enhancement steepens rapidly with distance from the core in this part of the jet (Fig. 14).

Figure 25 also indicates some intriguing correlations among the jet properties *within* these three principal sections:

1. At $\Theta = 20''$–$25''$, a rapid decline in the rate of lateral expansion of the jet (Fig. 11) occurs where (*a*) the jet reaches its peak brightness in the inner region (Fig. 4); (*b*) a steep RM gradient appears *across* the jet (Fig. 21); and (*c*) the projected magnetic field on the jet axis first becomes significantly oblique to the axis (Fig. 23). This region also marks the onset of the extended region over which the central brightness I_ν of the jet declines with FWHM Φ as $\Phi^{-1.5}$ (Fig. 14).

2. At $\Theta = 40''$–$60''$, the second local decline in the rate of lateral expansion of the jet is accompanied by (*a*) the ap-

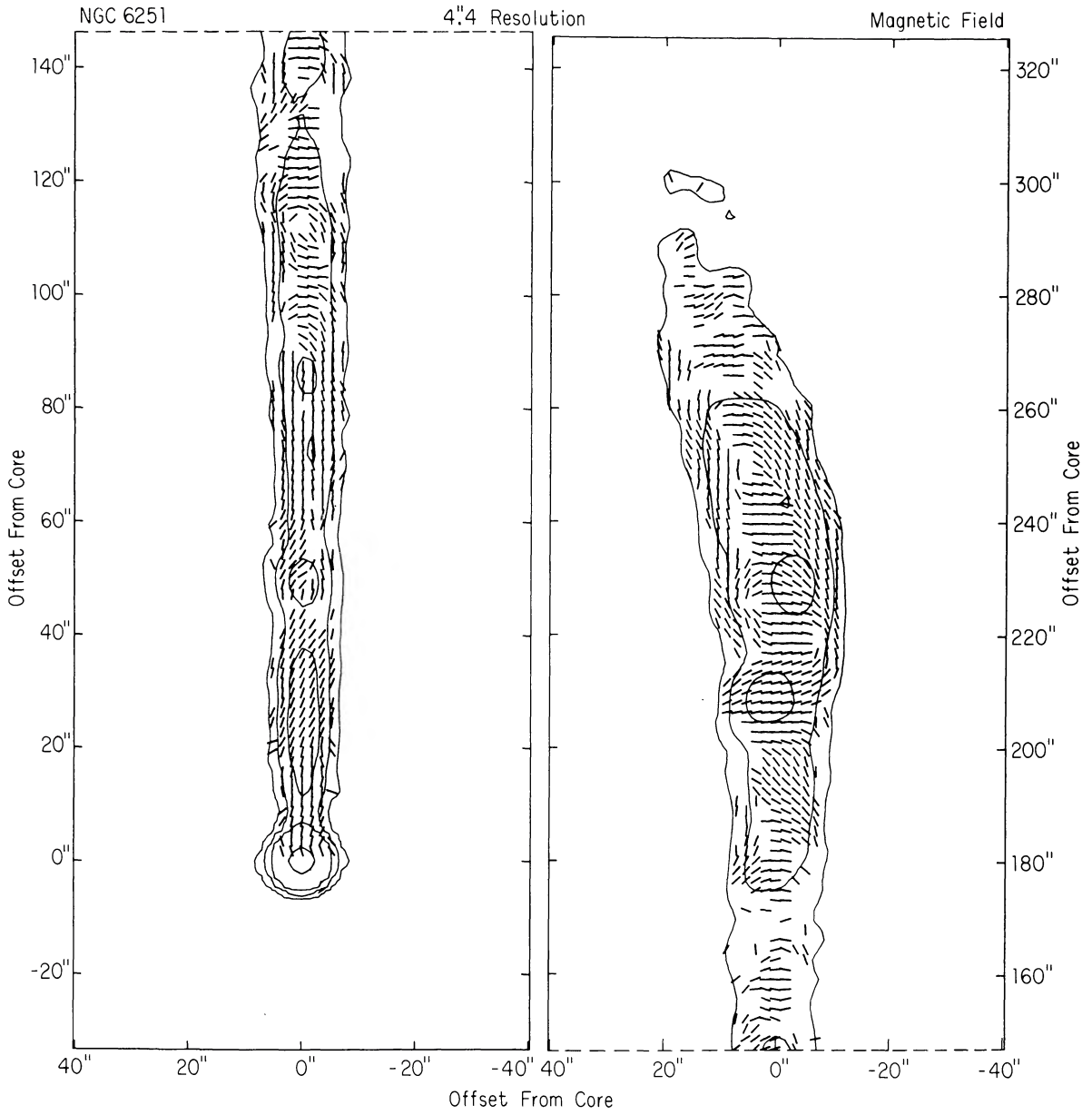

FIG. 22.—Map of the projected magnetic field configuration over the first 4'.4 of the jet at 4".4 resolution. The lines are of constant length; their orientations are those of the projected *B*-vectors.

pearance of a bright knot, at $\Theta = 50''$; (*b*) the appearance of an exceptionally steep transverse RM gradient (opposite in sign to that at $\Theta = 20''$–$25''$); and (*c*) a local anomaly in the projected magnetic field, which briefly becomes perpendicular to the jet axis at the center of the jet. This region also exhibits strong local departures from the average $\Phi^{-1.5}$ law of brightness variation with jet radius.

The following section relates some of these properties, and the correlations among them, to physical processes within and around the jet.

VII. DISCUSSION

a) *Freedom and Confinement of the Jet*

We saw in § IV*d* above (Figs. 10 and 11) that the jet expands at a variable rate. The growth of the jet's transverse FWHM Φ with angular distance Θ from the core is similar to that of the main jet in NGC 315 (Willis *et al.* 1981; Bridle, Chan, and Henriksen 1981; Bridle 1982): a regime of rapid expansion followed by a collimation "shoulder" where $d\Phi/d\Theta \rightarrow 0$, then reexpansion.

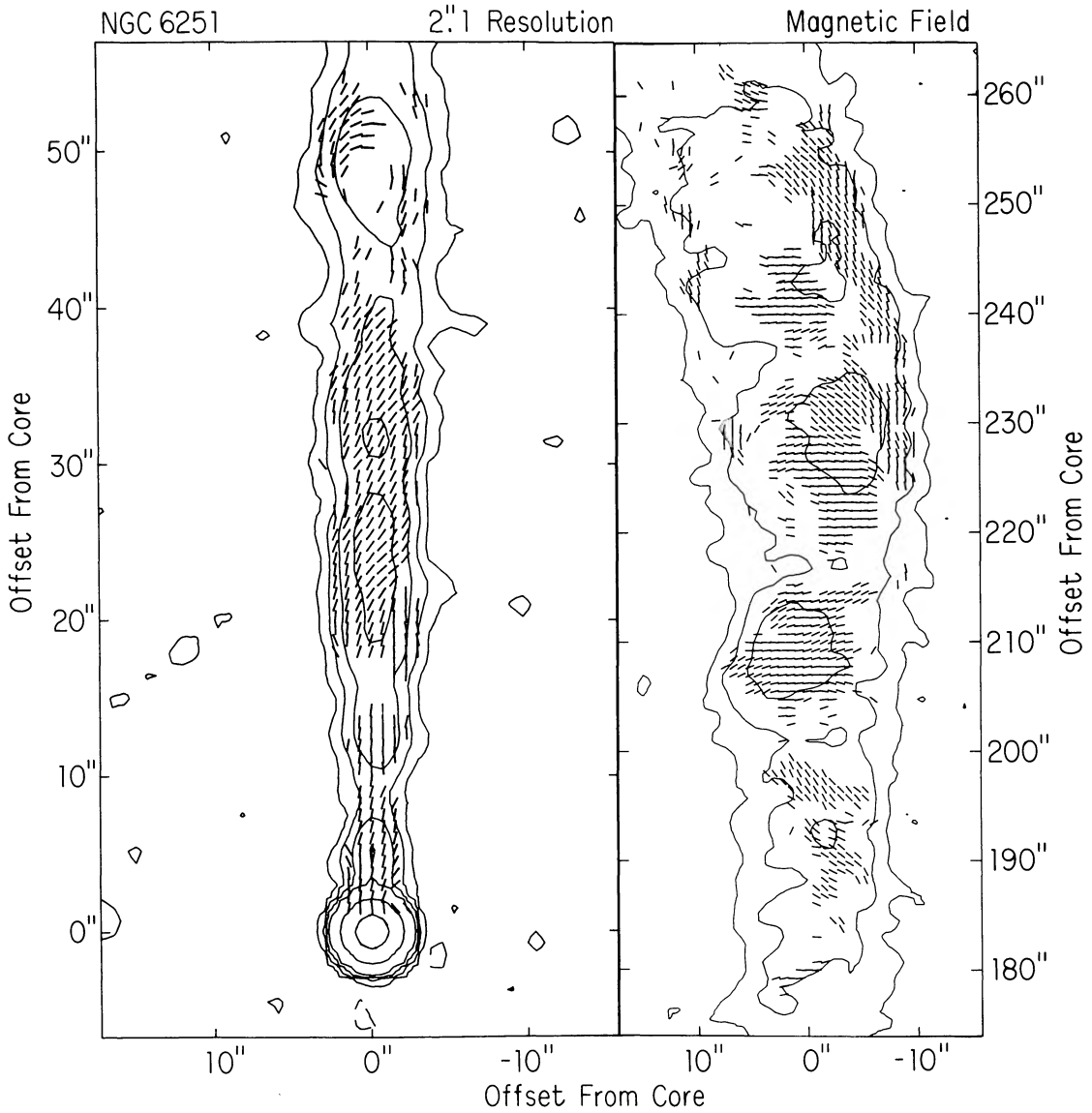

FIG. 23.—Map of the projected magnetic field configuration over the inner 55″ of the jet (*left panel*) and outer 90″ of the jet (*right panel*) at 2″.1 resolution. Vectors are shown only at positions where the *E*-vector position angles χ were accurate to better than 15° at all four frequencies. The lines are again of constant length.

A free (unconfined) jet expands laterally with a velocity v_r equal to its internal sound speed c_s where it first became free. Even if c_s subsequently decreases, e.g., because of radiative cooling of the jet material, the transverse expansion in a free jet continues at its original speed v_r. Steady, free jets therefore expand at a constant rate $d\Phi/d\Theta$ (unless their longitudinal motion is decelerated by gravity, in which case their rate of expansion $d\Phi/d\Theta$ could appear to accelerate). This is clearly *not* what is observed in NGC 6251.

The *average* expansion rate (from the FWHM data) in the first regime of rapid expansion at $\Theta < 17''$ is $\langle d\Phi/d\Theta \rangle = 0.16$. This rate corresponds to a Mach number of 14 sec ι if this regime of the jet (the first 7 kpc) is in fact free. (Here ι is the angle between the axis of the jet and the plane of the sky). If the jet is *confined* at these distances, it would expand at $v_r < c_s$, so that the actual Mach number would be less than 14 sec ι.

The expansion rate in the range $12'' < \Theta < 20''$ appears to be faster ($d\Phi/d\Theta \approx 0.35$), but the data for $17'' < \Theta < 20''$ are influenced by the center-darkening of the knot at $\Theta = 18''$. At this knot the fitted Gaussian FWHM grows rapidly as a result of the change in the transverse profile shape, so the Φ-Θ data for $17'' < \Theta < 20''$ should not be used to estimate the Mach number of the flow.

To zeroth order, the *minimum* pressures required to confine the jet can be estimated from the equipartition calculations in § V*d* (Table 2), as described by Burns, Owen, and Rudnick (1979). Expressing the required pressures as equivalent den-

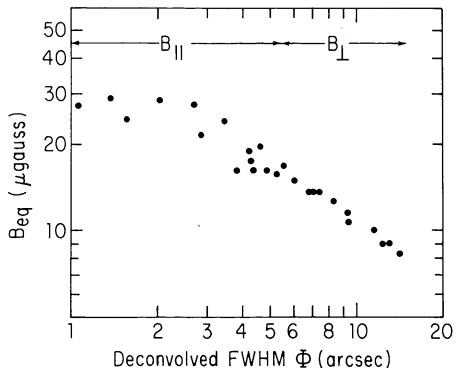

FIG. 24.—Variation of the equipartition magnetic field strength B_{eq} in microgauss with the deconvolved FWHM Φ of the jet at 1662 MHz. The regions of the diagram derived from data with $B_{\parallel}$ and $B_{\perp}$ dominant on the jet axis are indicated by the arrows.

sity-temperature (nT) products, we find that the minimum values of nT can decrease from $\sim 1.6\times10^5$ cm^{-3} K at 10″ (4.3 kpc) from the core to $\sim 1.6\times10^4$ cm^{-3} K at 130″ (56 kpc) from the core. Thermal pressures of the necessary magnitude could therefore be provided by an external medium at $T\sim 3\times10^7$ K whose density declines from 0.005 to 0.0005 cm^{-3} over this range of distances from the core. These parameters are similar to those of X-ray halos detected around several nearby elliptical galaxies by observations from the *Einstein Observatory* (Fabricant, Lecar, and Gorenstein 1980; Schreier, Gorenstein, and Feigelson 1982; Biermann and Kronberg 1983). We therefore examine thermal confinement models for the jet in some detail.

Chan and Henriksen (1980, hereafter CH) and Bridle, Chan, and Henriksen (1981, hereafter BCH) gave models for thermally confined *self-similar* supersonic jets whose expansion properties may be calculated simply by integration of a certain ordinary differential equation. Figure 26 (*upper panel*) shows an illustrative fit to our Φ-Θ data of a thermally confined model of the type shown by BCH in their Figure 3. The dynamical effects of the magnetic field were set to zero in this model by choosing the Alfvénic Mach number at its sonic point to be 10^{10}. Table 3 lists other parameters of the model.

We have not demanded that the model reproduce all features of the data, for several reasons. First, we are comparing the parametric radius R of the model with the FWHM Φ of the synchrotron radiation from the jet. The relation between these quantities depends on the three-dimensional structure of the magnetic fields in the jet and on the distribution of relativistic particles within it. Second, the assumption that the jet's internal structure is self-similar at all distances from the core may be only a rough approximation to the behavior of a real jet when its collimation properties change suddenly with distance. For example, a supersonic jet may be shocked internally when its expansion rate changes rapidly, and shocks are not described explicitly in the self-similar model.

Figure 26 (*lower panel*) shows the run of the external pressure in the fitted model. A rapid decline in pressure with distance from the core, initially as $\Theta^{-4.15}$, is required for $\Theta \le 10''$ (≤ 4 kpc) along the jet. This is followed by a much slower decline, proportional to $\Theta^{-1.5}$, over the range $10'' < \Theta < 120''$ (4–50 kpc), steepening asymptotically to $\Theta^{-2.6}$ at $\Theta \ge 150''$ (64 kpc). The collimation properties of the jet could therefore result from passage of the jet through an initial rapidly declining kpc-scale "core" atmosphere of NGC 6251 into a "halo" with a pressure scale of some tens of kpc.

Sanders (1983) has drawn attention to the fact that an initially confined jet, such as we assume here, can become free if the external pressure drops rapidly, by "detaching" from the confining pressure as described by Courant and Freidrichs (1948). Such detachment occurs if the jet would otherwise need to expand supersonically to maintain pressure balance with the external medium. Sanders notes that a highly supersonic jet should detach from its confinement if the confining pressure declines as a power law steeper than z^{-2}. This does not conflict with our invocation of a steeper power law in the initial regime of the above model, however. In this simple form, Sanders's conclusion is *asymptotically* true (in the hypersonic limit), but a jet emerging from a nozzle into a power-law atmosphere takes many nozzle scales to adapt its expansion to the pressure gradient in the atmosphere and cannot react instantaneously to changes in this gradient. We tested the self-consistency of the BCH model shown in Figure 26 by

TABLE 2

EQUIPARTITION PARAMETERS OF JET

Angular Distance (Θ) from Core	FWHM Φ	B_{eq} (μgauss)	$U_{min}\times10^{13}$ (J m^{-3})
8″.8	1″.06	27.	55.
9.9	1.57	24.	56.
11.0	1.36	29.	77.
13.2	2.01	28.	75.
16.5	2.86	22.	44.
26.4	2.76	27.	70.
31.9	3.45	24.	54.
38.5	4.85	16.	24.
49.5	4.21	22.	47.
57.2	3.90	16.	24.
63.8	4.32	17.	26.
71.5	4.21	19.	33.
80.3	5.22	16.	23.
84.7	4.60	20.	35.
94.6	7.07	14.	17.
100	5.52	17.	27.
105	6.98	14.	17.
112.5	7.43	14.	17.
117	9.32	11.5	12.
121.5	9.41	10.6	11.
126	11.6	10.0	9.4
127.5	12.5	9.0	7.5
129	14.2	8.3	6.5
132	13.0	8.9	7.4
143.5	8.0	9.1	7.7
164.5	13.6	6.5	2.6
192.5	8.15	10.9	11.
199.5	10.4	8.3	6.4
210	9.12	12.	13.
217	12.2	7.7	5.6
231	11.9	9.7	8.7
238	15.8	7.0	4.6
252	14.0	10.7	11.
262.5	17.6	5.1	2.4
276.5	18.8	3.7	1.3

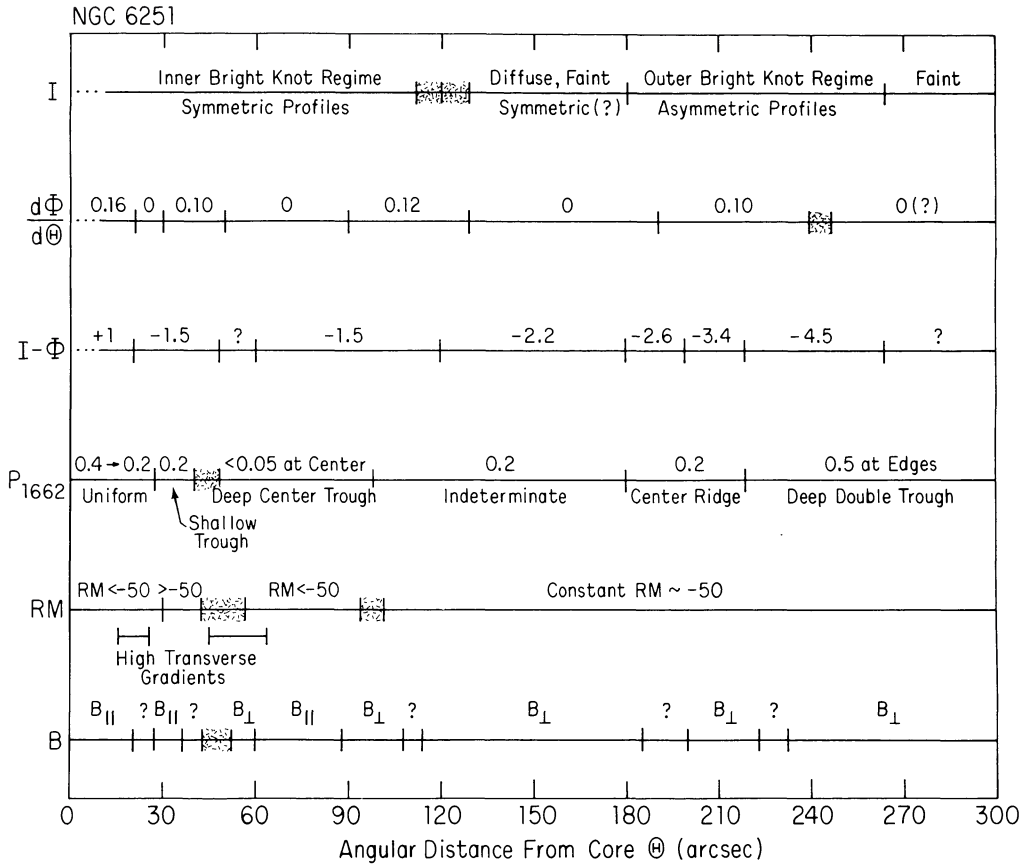

FIG. 25.—Summary of systematic variations of jet properties with distance from the radio core. The rows of the figure show, in turn, attributes of the variation of the total intensity (I), the expansion rate ($d\Phi/d\Theta$), the slope of the central intensity vs. FWHM[$I_\nu(\Phi)$] relation, the degree of linear polarization at 1662 MHz (p_{1662}), the rotation measure (RM), and the dominant projected magnetic field component on the axis of the jet (B). Well-defined transition points are marked by single bold bars; less well-defined transition regions are marked with broad bands.

checking that the predicted expansion was locally subsonic everywhere along the jet.

Computation of a BCH model in which only the inner rapidly varying component of the model atmosphere shown in Figure 26 was present demonstrated that, in the absence of the outer pressure component, the jet would have detached from the confining pressure (i.e., become "free") ~12″ from the core. The model given in Figure 26 has begun to adjust to the "halo" pressure term by that distance from the core, however, so the local Mach number of its lateral expansion nowhere exceeds 0.6. The model's self-consistency is sensitive to the height assumed for the sonic point, or nozzle, however. If the nozzle height for this *large-scale* jet (*not* necessarily that of the VLBI jet) were a factor of 2 closer to the core than the 1.″6 (690 pc) used for this model, then the jet might have become free before it encountered the "halo" pressure. This alternative has some attractive features, which we consider further below.

Table 4 gives the *minimum* values of the mass and of the 0.5–4 keV thermal bremsstrahlung luminosity associated with the external medium whose pressure curve is shown in Figure 26, as a function of its assumed (isothermal) temperature. The pressures have been normalized to the minimum pressures of the relativistic particles and fields in the radio jet in the range from 10″–120″ (4.3–51 kpc) from the core. If the temperature in the halo medium is similar to the 3×10^7 K in the M87 halo (Kellogg, Baldwin, and Koch 1975; Fabricant, Lecar, and Gorenstein 1980; Lea, Mushotzky, and Holt 1982), then the 0.5–4 keV luminosity of the *halo* component of NGC 6251 need be no more than 1.4×10^{42} ergs s^{-1}, 1/10 that of the halo in M87. A 1.9×10^7 K X-ray atmosphere of approximately the needed "halo" central density in Figure 26, but of smaller linear scale, has been detected around the normal elliptical galaxy NGC 5846 by Biermann and Kronberg (1983). Preliminary results from 22,000 s of *Einstein* IPC observations of NGC 6251 itself (Ku 1982) show an inner X-ray source ($<$ 40 kpc in scale) with 0.5–4 keV luminosity 1.4×10^{42} ergs s^{-1}. Ku also derives an upper limit of $\leq 2.1\times10^{41}$ ergs s^{-1} to the luminosity of any more extended (150 kpc) "halo." Halos with properties similar to those needed to confine the jet in NGC 6251 evidently occur in other elliptical galaxies, and the *Einstein* data on NGC 6251 itself are consistent with thermal confinement of the jet beyond 20″ (9 kpc) from the core if the temperature there is ~ 3×10^7 K.

Extrapolation of the "core" component of Figure 26 into the *base* of the jet predicts a much larger X-ray luminosity in the inner ~ 2″ (~ 0.9 kpc) than the total observed by Ku (1982). We conclude that, unless the interstellar medium on

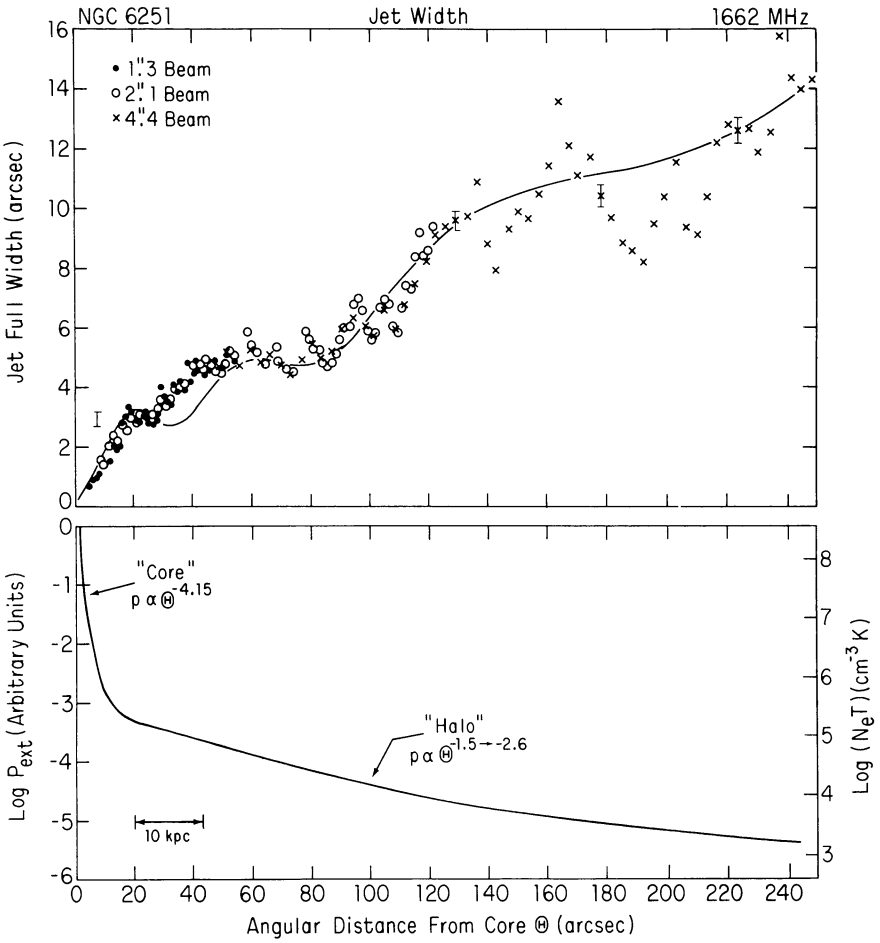

FIG. 26.—*Upper panel*: BCH thermal pressure confinement model (*solid line*) fitted to the FWHM data from Fig. 10. *Lower panel*: external pressure variation in the BCH model fitted to the data in the upper panel.

this scale in NGC 6251 has a temperature well above, or well below, 3×10^7 K, the X-ray luminosity of the source observed by Ku is incompatible with thermal confinement of the inner few seconds of the jet. It is therefore more likely that the *rapidly expanding* region of the jet at $\Theta < 20''$ is a regime of free expansion in which the Mach number of the jet is $\sim 14 \sec\iota$ as estimated above. (As noted earlier, the BCH model shown in Fig. 26 could be adapted to produce these conditions by lowering the assumed height of its sonic point.) The slower expansion at $\Theta \approx 20''$ could then result from reconfinement of a detached jet (whose internal pressure would be rapidly decreasing) by the slowly varying "halo" component of the pressure curve shown in Figure 26.

TABLE 3

PARAMETERS OF MODEL ATMOSPHERE IN THERMAL CONFINEMENT FIT

$$p = \frac{f}{1+(f-1)(z/z_s)^m} + \frac{(1-z_s/z)(z_s/z_e)^m}{1+(z/H)^{m'}} \times \frac{f}{f-1},$$

where $f = [(\Gamma+1)/2)]^{\Gamma/(\Gamma-1)}$; $\Gamma = 4/3$; $z_s = 1''.6 = 0.69$ kpc; $z_e = 11''.95 = 5.13$ kpc; $H = 39''.0 = 16.7$ kpc; $m = 4.15$; $m' = 2.60$, and jet radius ($z = 1''.6$) $= 0''.12 = 51$ pc.

Sanders (1983) has discussed the dynamics of reconfinement of initially free jets by halo components of galactic or cluster atmospheres. He concludes that conical shock waves propagate into the jets, possibly leading to particle reacceleration there, as discussed by Blandford and Ostriker (1978). This may, in principle, account for the center-darkening of the knot at $\Theta = 18''$, immediately coreward of the first clear slowdown in the expansion. The expanding jet would first "notice" the confining external pressure at its edges, so the growth of shocks, and of particle acceleration associated with them, would begin at the edges. This could lead to the observed limb-brightened (center-darkened) transverse profile. The shocks would propagate into the jet and reflect, leading to (possibly quasi-periodic) increases in brightness and oscillations in the expansion rate farther down it as direct and reflected shocks cross. Shock crossings might be responsible for the train of bright knots beyond the region ($\Theta \approx 20''$) where the lateral expansion of the jet first slows dramatically, and again beyond the "second reconfinement," at $\Theta \approx 45''$. Both of these confined regions also exhibit "anomalous" projected magnetic field orientations (see Fig. 23), which

TABLE 4

MINIMUM MASS (M) AND 0.5–4 keV LUMINOSITY (L) OF MEDIUM REQUIRED TO CONFINE JET IN NGC 6251

PARAMETER	TEMPERATURE (K)		
	4×10^7	2×10^7	10^7
Halo L (2.0–50 kpc)[a]	1.3×10^{42}	4.5×10^{42}	1.1×10^{43}
Halo M (2.0–50 kpc)[b]	3.8×10^{10}	7.5×10^{10}	1.5×10^{11}
Halo L (2.0–200 kpc)[a]	1.5×10^{42}	4.9×10^{42}	1.2×10^{43}
Halo M (2.0–200 kpc)[b]	1.2×10^{11}	2.4×10^{11}	4.7×10^{11}
Core L ($\leqslant$1.0 kpc)[a]	4.7×10^{43}	1.6×10^{44}	3.8×10^{44}
Core M ($\leqslant$1.0 kpc)[b]	7.6×10^{8}	1.5×10^{9}	3.0×10^{9}
Core L ($\leqslant$ 2.0 kpc)[a]	5.2×10^{43}	1.7×10^{44}	4.1×10^{44}
Core M ($\leqslant$ 2.0 kpc)[b]	1.2×10^{9}	2.5×10^{9}	5.0×10^{9}

[a] In ergs s^{-1}.
[b] In units of $M_\odot$.

might be produced by oblique shocks compressing the field in the jet.

We conclude that the brightness and polarization structure of the jet near its major recollimation points qualitatively resembles that described by Sanders's model for reconfinement. This reinforces our inference from the X-ray data that the rapidly expanding innermost regime of this jet is one of free (detached) lateral expansion. We plan higher resolution observations of these regions to test these speculations by examining the detailed morphology, magnetic configurations, and spectral index distributions in the knots in the inner jet.

Although NGC 6251 is an X-ray source of approximately the correct *luminosity* to account for thermal confinement of the jet beyond 9 kpc from the core, the *spatial distribution* of its X-ray emitting gas is not yet clear. It is particularly important to know the scale size of the inner 1.4×10^{42} ergs s^{-1} which is not resolved by the *Einstein* IPC data. If most of this emission originates in the inner few kpc of NGC 6251, thermal collimation of the jet might be ruled out at all distances, and an alternative mechanism would then have to be invoked.

CH and BCH also included in their self-similar jet models the $\boldsymbol{J}\times\boldsymbol{B}$ force between any current carried along the jet and its associated circumferential magnetic field. For the pure CH field configuration, a mixture of thermal and magnetic confinement can also produce expansion properties similar to those observed in NGC 6251 (e.g., Fig. 5*b* of BCH). The magnetic field configuration observed *in the NGC 6251 jet itself* cannot confine the jet in this way, however, since the major collimation changes shown in Figures 10 and 11 occur within the part of the jet where the apparent magnetic field (Fig. 22) is predominantly longitudinal. If the jet is partially or totally confined by magnetic stresses, these must be associated with a circumferential component of the field that lies *outside* the observed synchrotron-emitting region. (The return current must also be unobservable.) We now discuss the evidence from our data that there are indeed magnetic fields (but of indeterminate configuration) in NGC 6251 outside the radio jet.

b) Evidence for a Magnetoionic Medium in NGC 6251

Figure 27 shows a profile of the RM variation along the ridge line of the jet as a function of distance from the core. Also marked is the approximate outer boundary of the optical image of NGC 6251 on the Palomar Schmidt print shown in Figure 28 (Plate 2).

The RM of ~ -49 rad m^{-2} in the outer parts of the jet is similar to the mean of the RMs measured for other extragalactic sources in this area of sky ($l=116°$, $b=31°$) by Simard-Normandin and Kronberg (1980). We therefore attribute this component of the RM over the jet to foreground rotation in the magnetoionic medium of our Galaxy, especially since we find no depolarization in this part of the jet at any resolution (§ V*a* above). In contrast, the large RM gradients in the first 70″ (30 kpc) of the jet are very unlikely to be fluctuations in the Faraday depth of the line of sight through

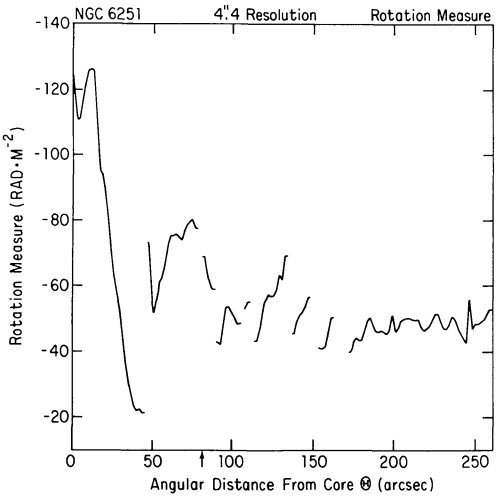

FIG. 27.—RM profile along the jet ridge line at 4″.4 resolution. The arrow marks the outer boundary of the light associated with NGC 6251 in the plate shown as Fig. 28.

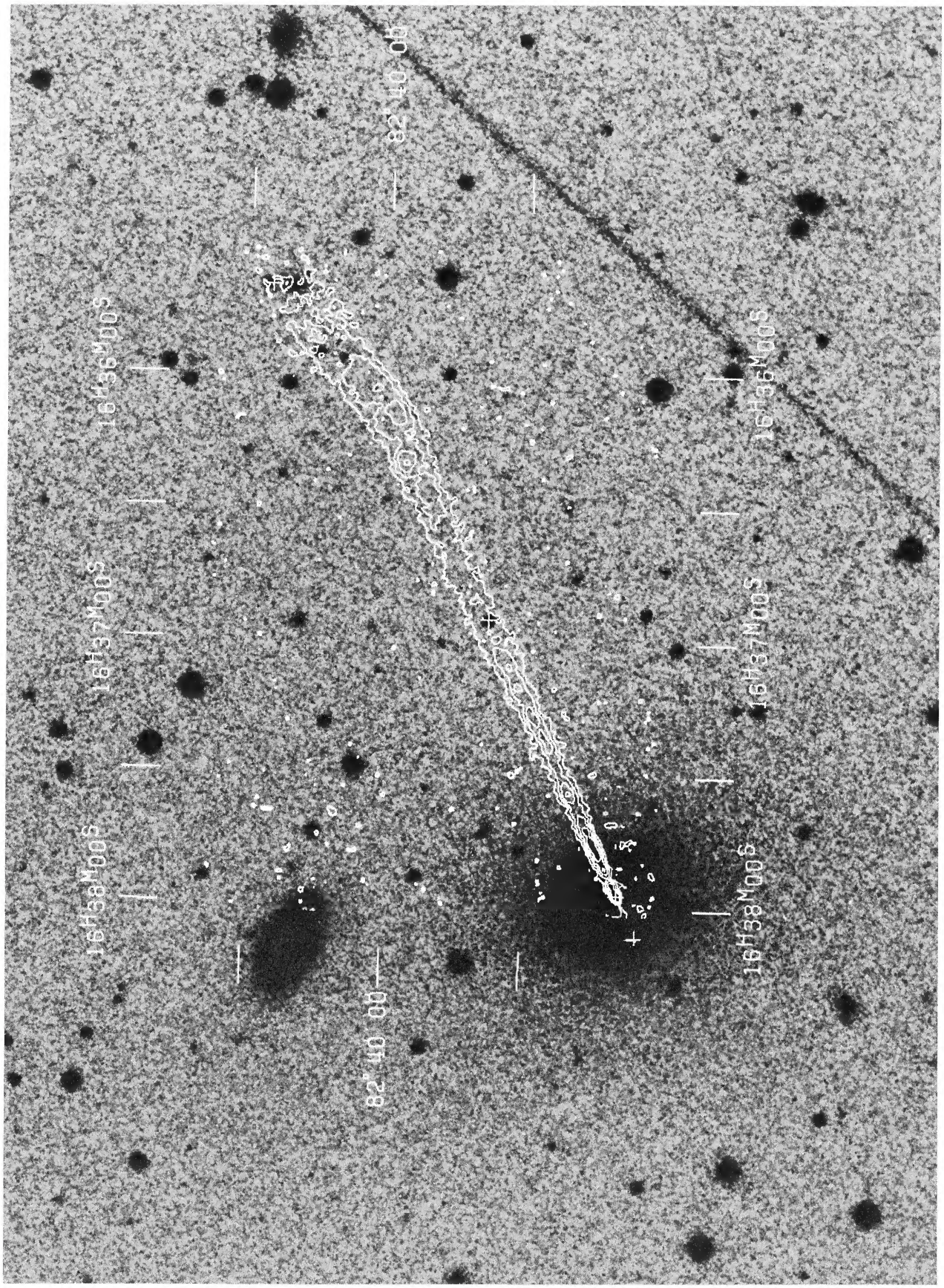

FIG. 28.—Contours from the 1480 MHz map at 4'.4 resolution, superposed on a Palomar 48″ Schmidt plate of NGC 6251 (127-O4 emulsion) obtained by Dr. A. G. de Bruyn

our Galaxy, for three reasons. First, observations of other radio galaxies of large angular extent (Willis and Strom 1978; Strom and Willis 1980; Willis *et al.* 1981) show that the foreground Faraday screen generally changes by only a few rad m^{-2} over scales of several arc minutes as indeed we find in the outer jet of NGC 6251. Second, NGC 6251 is well removed from the areas of sky where Simard-Normandin and Kronberg (1980) found large local fluctuations among the RMs of adjacent sources. Third, the correlation of the most deviant RMs with the optical extent of NGC 6251 is unlikely to occur by chance, as would have to be the case if they were produce by material in our Galaxy. It is much more likely that the variations in RM across the base of the jet arise in a magnetoionic medium in or around NGC 6251 itself, particularly since the most negative RMs occur on the lines of sight closest to the center of NGC 6251.

It is very unlikely that much of the Faraday rotation arises within the jet itself, however. A second Faraday screen producing -80 rad m^{-2} of RM in addition to the galactic contribution of -49 rad m^{-2} must rotate the *E*-vectors at 1370 MHz by $\sim 220°$ from the position angles they would have had in the absence of the second screen. If the second screen were fully mixed with the synchrotron-emitting region of the jet, the differential rotation between the front and the back of the jet would depolarize it significantly at 1370, 1480, and 1662 MHz. The expected depolarization depends on details of the field and particle configurations in the jet, but simple slab models predict a depolarization of ~ 0.15 between 1480 and 4885 MHz. Given the high degrees of polarization in the regions most negative RM, and the fact that the values of p_{1480}/p_{4885} in the inner parts of the jet *at high resolution* (§ V*a*) are ~ 1.0, it is unlikely that more than ~ 20 rad m^{-2} of the RM variation arises from a Faraday screen within the jet itself.

We may also compare the situation in NGC 6251 with the calculations of Faraday rotation within homogeneous cylinders by Cioffi and Jones (1980). They showed that the rotation of the *E*-vectors from their unperturbed angles due to internal Faraday depth in a homogeneous cylinder that is viewed edge-on (a first-order approximation to a radio jet) cannot exceed $\sim 60°$. In NGC 6251, however, there are *differential* rotations of the *E*-vectors across the base of the jet that significantly exceed 60°. This confirms our conclusion that material along the line of sight between our Galaxy and the jet must produce the observed RM variations. Given the correlation between the largest negative RMs and the center of NGC 6251, between the RM fluctuations and the optical extent of the galaxy, and the conclusion that the Faraday screen cannot lie within the jet itself, we infer that the variable component of the Faraday screen mapped in Figures 20 and 21 lies in front of the jet, within or immediately around NGC 6251 itself.

The jet lies close to the minor axis of NGC 6251, and the scale of the "excess" Faraday screen is that of the visible galaxy (Fig. 27). If the thermal material responsible for the excess Faraday screen is spheroidally distributed around the nucleus of NGC 6251, the RM gradient would lie primarily *along* the radio jet unless the magnetic field configuration is one with strong large-scale gradients in the line-of-sight component in other directions. Figures 20 and 21 show that the contours of constant RM are approximately perpendicular to the jet over the first 15″ (6 kpc) from the core, but further out the RM has a complex structure with steep gradients *across* the jet as well as along it. Most of the variation from RMs near -130 rad m^{-2} at the base of the jet to -49 rad m^{-2} in the outer jet occurs between 15″ and 70″ (6 and 30 kpc) from the core. In this region the contours of constant RM are not perpendicular to the jet but run approximately along P.A. 80°.

These RM gradients must in part be due to gradients in the thermal density or in the line-of-sight magnetic field along P.A. $-10°$, significantly displaced from the optical minor axis of NGC 6251. Monotonic gradients in density alone (such as would be expected in a smooth galactic halo) could not produce the reversal in sign of the RM gradient that occurs $\sim 40''$ from the core. Density gradients alone also cannot explain why the RMs in this region are *less* negative than those we attribute to the foreground medium of our Galaxy, whereas those elsewhere in the jet are *more* negative. Both the change in sign of the RM gradient and the small values of the RM in this region of the jet require that the (density-weighted) line-of-sight magnetic field in NGC 6251 reverses *direction* on (projected) scales of 10″ (4.3 kpc) in the foreground of the jet. Evidence for a similar kpc-scale "magnetosphere," also with significant reversals of the integrated line-of-sight field, has also been found from RM determinations within the active elliptical galaxy M84 (Laing and Bridle 1983). We cannot determine the field structure outside the jet in NGC 6251, however, (*a*) because the RM data are only quasi–one-dimensional as a result of the shape of the jet, and (*b*) because any clumping of the ionized medium along the line of sight through NGC 6251 weights the line-of-sight field integration in an unknown manner.

We can estimate the properties of the magnetoionic medium outside the NGC 6251 jet only if we assume that it is smooth. If (*a*) the thermal density contributing to the large-scale Faraday screen is modeled as a smooth spheroidal distribution of gas, (*b*) the typical line-of-sight component of the magnetic field through this gas is B_{-6} microgauss, and (*c*) the scale of the distribution is of order the 70″ (30 kpc) over which the large-scale RM gradient is observed, then the mean electron density in the region should be $\sim 0.003/B_{-6}$ cm^{-3} and the mass of ionized gas $\sim 8\times10^{9}/B_{-6}$ solar masses. While we have no independent constraints on the physical parameters of this medium, these values would be plausible if B_{-6} is in the range from 1 to 10. The emission measure of the material would be $0.5/fB^{2}_{-6}$ cm^{-6} pc, where f is the filling factor of the material. It would not be detectable optically unless it is strongly clumped ($f \ll 1$). Its density and scale would be similar to those of the medium required to confine the jet thermally at $T \approx 3\times10^{7}$ K (§ VII*a*).

Our data show, however, that not all of the Faraday screen in NGC 6251 is in a *smooth*, large-scale magnetosphere. Our high-resolution RM data (Fig. 21) show that the projected scale *along* the jet of the regions with the strongest RM gradients *across* it is 5″–10″. Furthermore, these regions cannot themselves be highly aggregated into clumps whose scales are smaller than our beam, for this would depolarize the jet emission at 1370–1680 MHz. The RM and depolarization data together suggest that the structures producing the *transverse* RM gradients have line-of-sight scales of order 5″–10″

(2.5–5 kpc). This is much less than the 70″ scale of the main longitudinal RM gradient discussed above. These smaller structures could not be distributed *evenly* throughout a spheroid of scale ~ 70″, for then there would be many along every line of sight, and the RM perturbations associated with them would superpose and average out. It is more likely that they are confined to a region itself of order 2.5–5 kpc from the jet, i.e., to a "sheath" surrounding it. A possible, but not obligatory, interpretation of our RM data would then be that the *transverse* RM gradients at these locations result from field lines which are looped around the jet axis in the neighborhood of the jet.

The existence of such field loops could hold promise for collimation of the jet by *external* magnetic fields if the jet carries a net current. We noted in § VI that the regions of strongest RM gradient transverse to the jet ($\Theta \sim 20''$ and $\sim 50''$) are also its regions of slowest lateral expansion. This correlation of improved collimation with large transverse RM gradients could indicate confinement of a current-carrying jet by surrounding loops of azimuthal magnetic field, in which clumps of ionized material produce the small-scale RM fluctuations. The physics of the correlation between transverse RM gradients and improved collimation could, however, work in the other direction, i.e., the RM structure could reflect a perturbation of the magnetosphere of NGC 6251 around the jet that was induced by another process which reconfined the jet. We cannot distinguish such possibilities at present, and the existence of the correlation itself is our only firm conclusion. Examination of the transverse RM gradients across other radio jets in regions where they become reconfined may, however, be worthwhile.

c) *Three-dimensional Structure of the Jet Magnetic Field*

In a flux-conserving expansion of a jet whose parametric radius R increases with distance z from the core, the field component parallel to the jet axis will vary as

$$B_{\parallel} \propto R^{-2}, \tag{2}$$

while the component perpendicular to the axis will vary as

$$B_{\perp} \propto R^{-1} v_j^{-1}, \tag{3}$$

where $v_j(z)$ is the flow velocity along the jet. In § V*d* we found that the *equipartition* field strength $B_{\rm eq}$ declined with the FWHM Φ of the jet as $\Phi^{-0.73}$ or slower over a region ($\theta < 90''$) where the projected field is dominated by the $B_{\parallel}$ component. If $R \propto \Phi$, the assumptions of equipartition and of flux conservation (eq. [2]) in this region are therefore clearly incompatible. We can envisage three possibilities. First, the projected magnetic field components shown in Figure 22 might not represent the dominant contribution to the magnetic field strength. For example, the field might be dominated by disordered field components whose variation along the jet is slower than that given by equation (2). This possibility is unlikely to be correct, however. There is evidence against it from the ~ 20%–50% degrees of linear polarization observed throughout the $B_{\parallel}$-dominated region of the jet. These are not far below the 71% maximum degree of polarization of synchrotron radiation from a particle spectrum with $\gamma = 2.3$ in a perfectly ordered field. If the scale of the hypothetical disordered field is much less than that of the jet, we may use Burn's (1966) relations for depolarization by random field fluctuations to estimate the maximum disordered field which would be consistent with observing ~ 20%–50% polarization. These relations imply that the disordered component of the field should be ~ 0.65 to 1.60 times the ordered component. In this case one could not ascribe the deviation from equipartition to a disordered component over the whole inner 90″ of the jet. A second possibility is that the assumptions of equipartition may not hold equally, or at all, along this region of the jet. A third possibility is that magnetic flux amplification is occurring, particularly of the parallel component in a shear layer at the edges of the jet. Either or both of these latter possibilities are compatible with our data.

We have examined the ability of several three-dimensional field structures to reproduce the observed distributions of total intensity, degree of polarization, and magnetic field orientation using a numerical routine (Bridle 1984) to compute these quantities for several model field structures. This routine calculates the total and polarized emission from each of 1300 cells on each of 130 lines of sight through the jet, given an assumed (axisymmetric) radial distribution of relativistic particles and an assumed magnetic field configuration. The pitch angle distribution of the particles is assumed to be isotropic in the applications described here. The inclination ι of the axis of the jet to the plane of the sky is allowed to vary, but the jet is assumed to be axisymmetric in all applicable parameters. The exponent γ of the electron energy spectrum is assumed to be uniform throughout the jet. In what follows, our comments on the ability of the field models to reproduce the intensity and polarization data on NGC 6251 are based on the predicted profiles after convolution to the resolution of our data. Examples of the unconvolved profiles produced by different models will be given by Bridle (1984).

Helical magnetic field configurations were proposed for the field distributions observed in 3C31 by Fomalont *et al.* (1980) and NGC 315 by Willis *et al.* (1981). The components of the helical field in (r, ϕ, z) cylindrical coordinates with the z-axis along the jet are the circumferential component B_{ϕ} and the axial component B_z given by

$$B_{\phi} = B_0 \cos\psi, \qquad B_z = B_0 \sin\psi, \tag{4}$$

where B_0 and the pitch angle ψ are constants across the jet. The helix-like field configuration used by CH and BCH in their self-similar jet models is of the form

$$B_{\phi} = B_0 \cos\psi_R (r/R), \qquad B_z = B_0 \sin\psi_R, \tag{5}$$

where B_0 is again constant, and the fiducial pitch angle ψ_R is $\arctan(B_z/B_{\phi})$ evaluated at the boundary of the jet ($r = R$). Laing (1981) calculated unconvolved profiles of total intensity and polarized intensity from these field structures for a relativistic particle spectrum with $\gamma = 2$ and a uniform distribution of radiating particles across the jet. He noted that both fields (4) and (5) predict extensive regions of longitudinal ($B_{\parallel}$) projected field at the edges of the jets, which are not observed in all jets. This objection does not apply to the field configura-

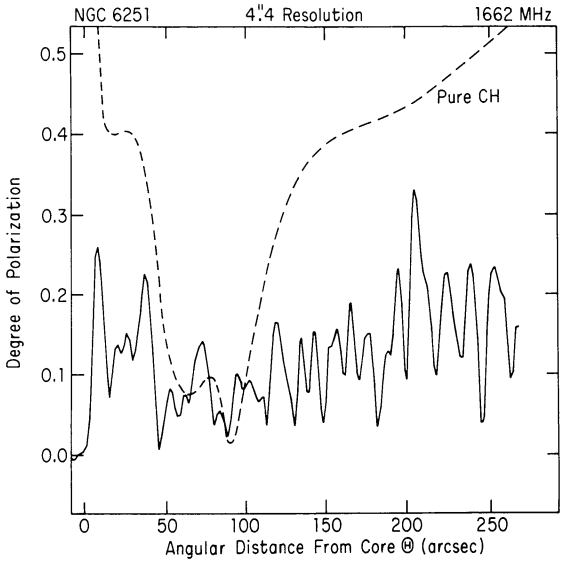

FIG. 29.— *Dotted line*: the variation of the degree of polarization along the ridge line of the jet predicted by a pure CH field in which ψ_R in eq. (5) varies as specified by the BCH model that was fitted to the data in Fig. 26. The jet is assumed to lie in the plane of the sky and to be uniformly filled with relativistic electrons. *Solid line*: the observed variation of p_{1662} along the ridge line, from Fig. 16. The poor agreement between the prediction and the data in the inner and outer jets illustrates the need to add random field components to the pure CH field model (see text).

tion in NGC 6251, however, for this does have extensive $B_\parallel$ edges to its $B_\perp$-dominated regions. We therefore tried fitting CH configurations to our data in some detail.

The map of the projected magnetic configuration at 4."4 resolution (Fig. 22) shows that the main transition from $B_\parallel$ to $B_\perp$ on the jet axis occurs at $\Theta = 90''$ (we do not consider the local anomaly at $\Theta = 50''$ significant in this context). If the jet lies within a few tens of degrees of the plane of the sky, the location of this transition tells us that ψ_R in equation (5) is $\sim 30°$ at $\Theta = 90''$. Given that the BCH model we fitted to the collimation data is highly super-Alfvénic, the evolution of the magnetic field components away from $\Theta = 90''$ can be determined from equations (2) and (3), to which the BCH equations reduce in the super-Alfvénic limit. The location of the $B_\parallel$-$B_\perp$ transition on the jet axis thus specifies the form of $\psi_R(\Theta)$ within the BCH model. This constrains the fitting to our data of the emission from the fields given by equation (5) at any distance Θ from the core.

The degrees of linear polarization predicted by *pure* CH fields using the values of $\psi_R(\Theta)$ from the fit to our $\Phi(\Theta)$ data are substantially greater than those we have observed, for any assumed inclination ι of the jet to the plane of the sky or any reasonable distribution of nonthermal particles with radius in the jet. Figure 29 shows the variation of the predicted degree of polarization on the axis of the jet for a pure CH field, a jet in the plane of the sky, and a constant density of nonthermal particles across the jet, to illustrate this discrepancy.

The predicted degrees of polarization in both the inner and outer jet can be reduced to the observed levels by introducing either thermal material or random field components into the model. The former alternative is unacceptable because the depolarization produced by thermal material varies with frequency, whereas we found $p_{1662}/p_{4885} \approx 1.0$ all along the jet. Furthermore, in a CH field, a small but finite Faraday depth depolarizes only one side of the jet; the other is *re*-polarized, due to the helicity of the field configuration. (This transverse depolarization gradient would be an important signature of the helix-like field configurations in jets with finite Faraday depths, and could be used to distinguish such configurations from other three-dimensional field structures if significant depolarization was detected in a jet.)

The addition of random components to the CH field (clearly plausible on physical grounds) can, however, reconcile the predicted and observed polarizations in a way which does not depend on frequency. We have computed the emission profiles for CH fields to which fully (three-dimensional) random field components have been added at every cell of the emission profile computation. The mean value of the random field component which must be so added to reduce the predicted polarization to the observed values decreases from $\sim 0.75B_0$ in the inner jet to $\sim 0.35B_0$ in the outer jet.

Within such "randomized CH" field models several constraints must be satisfied to obtain reasonable agreement between the predicted and observed total and polarized emission profiles as a function of distance from the core. First, wherever there are asymmetries in the degree of polarization *across* the jet, the jet must be inclined to the plane of the sky. In the region at $\Theta < 90''$, where $B_\parallel$ dominates, the fact that there is generally a polarization minimum *close to the axis* of the jet (Fig. 15) requires that the inclination of the jet to the sky is generally less than 10° and often less than or equal to 5°. In the outer jet, however, much larger inclinations, approaching 40°, are required to reproduce the asymmetries in the depths of the $B_\parallel$ regime across the jet. When this degree of freedom (which is consistent to within a factor of 2 with the observed wiggles of the jet in the plane of the sky) is allowed, we obtain reasonable fits to both the total and polarized intensity profiles all along the jet. Figure 30 shows modeled profiles for two typical locations, one at $\Theta = 32''$ in the inner jet, and the other at $\Theta = 227''$ in the double-trough structure of the outer jet. The parameters of these models are listed in Table 5. They illustrate the ability of the "randomized" CH field to reproduce the dominant features of the polarization distribution and of the projected field configuration—the model profiles should be compared with the data shown in Figures 9*b* and 9*e*.

We conclude that a CH-like field structure, combined with a suitable, and variable, mixture of random field components, is broadly consistent with the observations, provided that the inclination of the jet to the plane of the sky takes small ($< 10°$) values in the inner jet and larger ($\sim 40°$) values in the outer jet. In particular, the fact that the central polarization trough terminates where the jet begins to reexpand rapidly ($\Theta \sim 90''$) finds a natural explanation through the variation of ψ_R with Θ in such models. The azimuthal symmetry assumed in the model predicts either pure $B_\parallel$ or pure $B_\perp$ in the projected field at all locations in the jet, however. None of the regions of the jet where the projected field is oblique to its axis (Fig. 22) can be explained by such models.

Laing (1980, 1981) proposed a model for jet magnetic fields wherein the field is randomized in the plane at right angles to

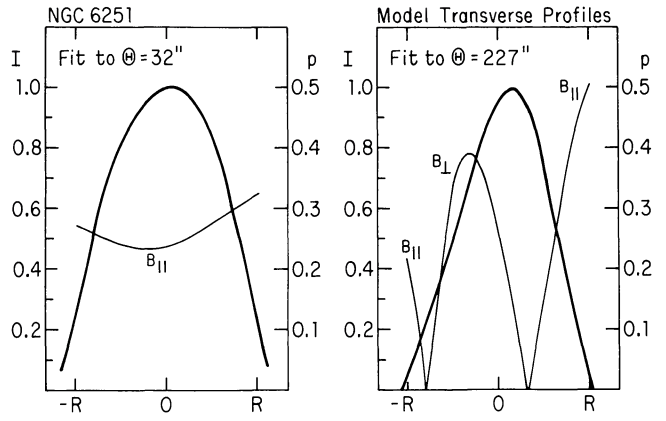

FIG. 30.—Sample fits to the transverse profiles of total intensity (*thick line*) and degree of polarization (*thin line*) of the inner and outer jet, obtained using "randomized" CH field models. These profiles have been convolved to the resolution of our data. They should be compared with those observed at $\Theta = 32''$ (Fig. 9*b*) and $\Theta = 227''$ (Fig. 9*e*). The parameters of the models are given in Table 5.

the jet axis, but has no component B_z along that axis. In this model, the degree of polarization should be constant across the jet, its value being determined (for given γ) solely by the inclination of the jet to the plane of the sky. The model also predicts that the projected magnetic field is $B_\perp$ all across the transverse profile. As the degree of polarization varies significantly across most of the transverse profiles in the NGC 6251 jet, and very few profiles have only $B_\perp$ components, this simple version of Laing's model cannot describe our data.

Laing noted that adding surface shears to this model, as discussed by Baan (1980), could account for the $B_\parallel$ edges to the $B_\perp$-dominated profiles in 3C31 and NGC 315, but he did not calculate specific profiles. We have computed profiles for a modification to Laing's model in which a B_z component is added to the tangled planar field to simulate the ability of shear layers at the edges of the jet to maintain field components parallel to the jet axis. We write

$$B_r = mB_0\rho_1, \qquad B_\phi = mB_0\rho_2, \qquad B_z = B_0(r/R)^n, \quad (6)$$

where ρ_1 and ρ_2 are uniformly distributed random numbers between -0.5 and $+0.5$, and m and n are adjustable parameters. The fields expressed by equation (6) produce variations in the degree of polarization across the jet, and $B_\parallel$ edges to the $B_\perp$ regions, provided the random and sheared components of the field are comparable in strength (i.e., $m \approx 1$). Unlike the profiles obtained from field models with helical field topology, however, *all* transverse profiles derived from equation (6), whether of total or polarized intensity and whatever the inclination of the jet to the plane of the sky, are symmetric about the center line of the jet. This conflicts with the polarization data on NGC 6251 at most distances from the core. It also conflicts with the total intensity profiles in the outer jet. In order to reproduce most of the observed profiles even qualitatively, the axial symmetry of the model would have to be broken, e.g., the sheared (B_z) component of the fields would have to vary with radius r *and* with azimuthal angle ϕ around the jet. We note that the projected magnetic field structure at the first major bend in the northern jet of 3C31 (Burch 1979; Fomalont *et al.* 1980) is very similar to that in the outer jet of NGC 6251. In both cases there is a deep $B_\parallel$ layer on the outer edge of a pronounced bend in the jet. This is consistent with interpreting the $B_\parallel$ layer as due to a nonaxisymmetric shear, stronger on the side of the jet which is "stretched" most as it rounds the bend. We stress, however, that this interpretation is not obligatory, and that the CH field structure is also readily consistent with the data, as shown above. We have not computed models which lack axial symmetry (due to the great possible variety of such models), so we do not show fits to our data of such "sheared Laing" fields.

We conclude that *none* of the simple magnetic structures previously proposed for radio jets represents the total and polarized intensity profiles and the apparent field in NGC 6251 well *at all distances from the radio core*. Fits to the regions of oblique field require deviations from the axial symmetry assumed in any of the simple models. The CH field simulates the data reasonably well if (*a*) random components are added to it in relative amounts which are allowed to vary along the jet, and (*b*) the outer jet is presumed to have deflections out of the plane of the sky that are about a factor of 2 larger than those observed in the plane of the sky. The "sheared Laing" field (eq. [6]) describes the data better than the "tangled field" of Laing (1980, 1981), but to fit the transverse asymmetries in the degree of polarization and the projected field orientation the shear must be assumed to lack azimuthal symmetry. Thus, to differing degrees, both classes of model require breaking of azimuthal symmetry to describe the observed properties of NGC 6251—the "randomized CH" model requiring this in the regimes $20'' < \Theta < 40''$ and $170'' < \Theta < 200''$, and the "sheared Laing" model virtually all along the jet.

TABLE 5

PARAMETERS OF CH FIELDS FITTED TO OBSERVED JET PROFILES[a]

PARAMETER	ANGULAR DISTANCE Θ FROM CORE	
	32″	227″
Field pitch angle Ψ_R	48°	14°
Angle ι of jet to plane of sky	5°	40°
Random field magnitude	0.75 B_0	0.35 B_0
Relativistic electron density	uniform	Gaussian, $\sigma = 0.94\ R$
Relativistic electron pitch angles	isotropic	isotropic

[a]See Fig. 30.

d) Particle Acceleration along the Jet

Consider an adiabatically expanding jet whose synchrotron emissivity ε at frequency ν varies as

$$\varepsilon_\nu \propto (B \sin\theta)^{(\gamma+1)/2} N_0, \tag{7}$$

where θ is the angle between the magnetic field direction and the line of sight, γ is the exponent of the power-law energy distribution of the relativistic electron density $N(E, E+\mathrm{d}E) = N_0 E^{-\gamma}\mathrm{d}E$, and the other symbols have their usual meanings. The variation of field components given by equations (2) and (3) of § VII*a* will be accompanied by a variation in the scaling constant N_0 for the relativistic electron density. We assume that the power-law energy spectrum extends from some minimum energy $E_{\min}$ to a maximum $E_{\max} \gg E_{\min}$ so that the total particle density $N_t \propto N_0 E_{\min}^{1-\gamma}$ for $\gamma > 1$. Particle conservation then requires $N_t v_j R^2 =$ constant along the jet, so that N_0 varies as

$$N_0 \propto v_j^{-1} R^{-2} E^{\gamma-1} \tag{8}$$

to conserve particle numbers (if $E_{\min}$ varies in the same way as the energy E of each particle). If the radiating particles do work as the jet both expands laterally and responds to variations in its flow velocity, then E varies as

$$E \propto R^{-2/3} v_j^{-1/3} \tag{9}$$

Equations (8) and (9) give the variation of N_0 in terms of R, v_j, and γ:

$$N_0 \propto R^{-(2\gamma+4)/3} v_j^{-(\gamma+2)/3}.$$

Hence, the "adiabat" for emissivity as a function of jet radius R is

$$\varepsilon_\nu \propto R^{-(5\gamma+7)/3} v_j^{-(\gamma+2)/3} \tag{10}$$

for a region whose dominant field component is $B_\parallel$ varying as in equation (2), or

$$\varepsilon_\nu \propto R^{(7\gamma+11)/6} v_j^{-(5\gamma+7)/6} \tag{11}$$

for a region whose dominant field component is $B_\perp$ varying as in equation (3). For the case of NGC 6251, with $\gamma \approx 2.3$ all along the jet, an adiabatic expansion would therefore produce:

$N_0(R) \propto R^{-2.87} v_j^{-1.43}$, i.e., the central brightness

$$I_\nu(R) \propto R^{-5.17} v_j^{-1.43} (B_\parallel); \tag{12}$$

$$I_\nu(R) \propto R^{-3.52} v_j^{-3.08} (B_\perp); \tag{13}$$

where we have taken $I_\nu \propto \varepsilon_\nu R$ for an optically thin jet. The $I_\nu \propto \Phi^{-1.5}$ law that is followed over most of the inner jet in NGC 6251 is much slower than expected on the basis of either equation (12) or (13), unless the jet velocity v_j decreases steeply with distance z from the core.

A likely mechanism for a steady velocity decrease in a supersonic jet is entrainment of material from the surrounding medium. If entrainment occurs at constant thrust, v_j is inversely proportional to the mass flux along the jet. A velocity v_j scaling proportional to $R^{-2.6}$ would be required to reproduce the observed $I_\nu(\Phi)$ law in the $B_\parallel$-dominated region of the jet, $v_j \propto R^{-0.66}$ in the $B_\perp$-dominated region. The former v_j-R law would require very large entrainment rates which would be difficult to maintain over large distances while preserving the integrity of the jet. It therefore seems unlikely that longitudinal compression of the jet caused by entrainment is the *sole* reason for the slow $I_\nu(\Phi)$ variation in the $B_\parallel$-dominated regime.

If v_j is approximately constant (as would be the case far from the nozzle in a steady supersonic jet without entrainment or dissipation), the observed variation of I_ν with Φ implies that either B, or N_0, or both, must decline with R more slowly than predicted by the "adiabats": equations (2), (3), (8), and (9). If the relativistic particles are always elastically scattered from the jet boundary and do no work as the jet expands, so that $E \propto v_j^{-1/3}$ replaces equation (9), equations (12) and (13) become

$$I_\nu(R) \propto R^{-4.30} v_j^{-1.43} (B_\parallel), \tag{12a}$$

$$I_\nu(R) \propto R^{-2.65} v_j^{-3.08} (B_\perp), \tag{13a}$$

respectively. Note that both of these laws are *also* steeper (for v_j constant) than the $I_\nu(R) \propto R^{-1.5}$ observed in the inner jet. If the particles and fields in a *constant velocity* jet with $I_\nu \propto R^{-1.5}$ are to remain in *equipartition* as it expands, then we require $B \propto R^{-0.63}$ (see § V*d*) and $N_0 \propto R^{-1.46}$. We conclude that *both* magnetic field amplification and particle reacceleration are required in any steady, constant velocity description of this jet, to account for the discrepancy between the observed brightness variations and all of the "adiabatic" equations given above.

A mechanism for particle reacceleration based on the concept of jets as turbulent mixing regions has been discussed by Henriksen, Bridle, and Chan (1982; hereafter HBC). They proposed that the small-scale viscous dissipation in jets is by the emission of MHD waves from turbulent eddies and the subsequent strong damping of these waves by acceleration of relativistic particles. For this discussion, it is immaterial whether the MHD waves accelerate particles directly through resonant interactions (e.g., Lacombe 1977; Benford, Ferrari, and Trussoni 1980; Eilek 1979, 1982), through the second-order Fermi mechanism (e.g., Bicknell and Melrose 1982), or by developing into shocks which accelerate particles via the first-order Fermi mechanism (e.g., Blandford and Ostriker 1978). These issues impinge primarily on the efficiency of turbulent acceleration and on the particle spectrum that it produces. Whatever the mechanism for the dissipation of the turbulence, we may hope to relate the large-scale turbulent energy to macroscopic observables ($d\Phi/d\Theta, \Phi$) of the jet.

HBC proposed that large-scale vortical hydrodynamic turbulence is intimately associated with the large-scale jet spreading (expansion) rate, so that the variation in turbulent power input along a jet can be estimated from its observed

collimation properties: $\Phi(\Theta)$. Bicknell and Melrose (1982) discuss a shear-driven instability that grows to the scale of the jet as a source of turbulent power. From either viewpoint the turbulent velocity can be estimated from macroscopic jet parameters, and (see HBC) the brightness I_ν at the center of the jet varies as

$$I_\nu \propto A(v_j/R)^2(dR/dz)^3, \quad (14)$$

where A is the mass flux along the jet. If dR/dz can be estimated from the variation of jet FWHM Φ with angular distance Θ from the core, equation (14) predicts the brightness evolution of the jet when A and v_j are known functions of distance z from the core. HBC found good agreement with the $I_\nu(\Phi)$ data for the main jet in NGC 315 taking A constant and using the form of $v_j(z)$ obtained from the BCH model for its collimation.

Figure 31 shows the behavior of equation (14) for A constant (a) assuming that $dR/dz \approx d\Phi/d\Theta$ from Figure 11 and (b) taking dR/dz from the externally confined BCH model fitted to our data in § VIIa. For both calculations the velocity variation $v_j(z)$ was taken from the BCH model of Figure 26. The predicted turbulent power in the outer jet depends critically on whether or not the flow radius R varies smoothly with z, as in the fitted BCH model and in our isophotal width data (Fig. 10), or oscillates violently, as in our FWHM data. This uncertainty in the relationship between the FWHM Φ and the flow radius R at the knots precludes a unique comparison between equation (14) and the $I_\nu(\Phi)$ data similar to that of HBC for the *smoothly* varying brightness distribution in NGC 315. Figure 31 shows, however, that *if* the fluctuations of Φ in the outer jet are accompanied by fluctuations of the flow radius R, then the turbulent power available for particle acceleration in the outer jet is from 3 to 10 times that available in the region $20'' < \Theta < 90''$. The enhanced brightness of the outer jet may thus, in principle, be explained by turbulence-derived acceleration mechanisms. If, however, the knot structure of the outer jet is due to variations in the synchrotron emissivity within a *smoother* flow structure, such as that in the isophotal widths and in the BCH model, then the turbulent power falls short of that required to rebrighten the jet by a factor of $\sim 10^2$. These possibilities cannot be distinguished at present.

The sudden brightness increases on the coreward sides of the knots in the outer jet (Fig. 14, *right panel*) contrast with the trend toward "adiabatic" brightness declines on their lobeward sides. Beyond $\sim 200''$ from the core, the slope of the $I_\nu(\Phi)$ relation in the outer jet away from these sudden brightness increases becomes as steep as (or steeper than) that predicted by the "adiabat" of equation (13). The particle *reacceleration* sites in the outer jet are therefore localized to the coreward sides of these knots, at $\Theta = 174''$, $202''$, and $220''$. The knots $190''$ and $210''$ from the core also have locally anomalous magnetic field orientations. These suggest that the acceleration mechanism in the knots is linked to the process which induces the deviations from axial symmetry in the ordered component of the jet's magnetic field. These properties make it tempting to associate this process with the development of oblique shocks in the jet. (The anomalous $I(\Phi)$ variation and modified magnetic field orientation in the region near $\Theta = 50''$ might be interpreted similarly.) We plan to observe the knots with higher angular resolution and at higher frequencies in order to compare their magnetic structures and spectral index distributions with those expected in shock-acceleration models.

e) Constraints on the Thermal Density in the Jet

The observed lack of depolarization in the inner jet at high resolution and of RM gradients across the outer jet can both be used to constrain the thermal matter density in the jet, if one *assumes* an explicit structure for its three-dimensional magnetic field. Since there are few other constraints on this density, it is of interest to consider the limits which can be derived from our data by assuming simple field configurations. We consider two typical regions of the jet, an "inner" region at $\Theta = 32''$ and an "outer" region at $\Theta = 230''$.

We first consider the slab approximation used by Willis *et al.* (1981) for NGC 315. Here the field is assumed to contain an ordered component whose line-of-sight component is of strength $B_L \propto B_{\rm eq}/\sqrt{3}$ all along a sight line of length L, plus a random component of variance B_r whose scale is d. It is further assumed that there are many fluctuation scales of the random component along the line of sight, so that $L/d \gg (B_r/2B_L)^2$. With these assumptions, the maximum uniform density at $\Theta = 32''$ that would leave $p_{1480}/p_{4885} > 0.8$, as observed, is $\sim 1.5 \times 10^{-3}$ cm^{-3}. A similar maximum density would be inferred from the same constraint using the homogeneous-cylinder model of Cioffi and Jones (1980). We have also used the profile modeling code of Bridle (1984) to compute the effects of finite Faraday depth in the randomized CH magnetic configuration fitted to the transverse profiles at $\Theta = 32''$ in Figure 30. In this case the helicity of the field structure produces a mixture of depolarization and repolarization across the jet, so the first noticeable effects of finite Faraday depth are (a) modification of the shape of the transverse polarized intensity profile and (b) introduction of an apparent RM gradient transverse to the jet. The degree of

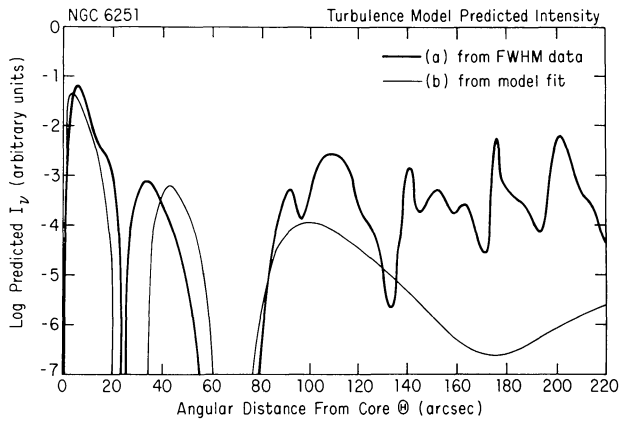

FIG. 31.—The variation of I_ν predicted from eq. (14) using the velocity from the thermally confined BCH model fitted to the jet in Fig. 26. Curve (a) shows the variation predicted if dR/dz is estimated from the FWHM data shown in Fig. 10. Curve (b) shows the variation predicted if dR/dz is estimated from the BCH model fitted to the data in Fig. 26.

polarization is not reduced significantly *all across the jet* in this field configuration until the density exceeds 4×10^{-3} cm^{-3}.

A second constraint arises from the lack of RM gradients across the outer jet. If the jet contains an average line-of-sight magnetic field B_L as before, and a uniform density of thermal particles, RM gradients should be found between the center and the edge of the jet in a uniform field geometry, due to the variation across the jet of the length L of the line of sight through it. In the regions of high signal-to-noise ratio in the outer jet we see no gradients as large as 5 rad m^{-2} across the jet. This sets an upper limit of 1.7×10^{-4} cm^{-3} to the average thermal density in the outer jet assuming a uniform field with $B_L = B_{eq}/\sqrt{3}$. In a CH or randomized CH field geometry, both the variation of L and the helical winding of the organized field component contribute to RM gradients across the jet. We use the code of Bridle (1984) to determine that the same upper limit to the RM gradients across the regions of high signal to noise in the outer jet places an upper limit to the uniform thermal density there of 2×10^{-4} cm^{-3} using the randomized CH field geometry fitted to the data at $\Theta = 227''$ in § VII*c* above.

The argument based on the RM gradient cannot be used to constrain thermal densities in the inner jet, because we do see large RM gradients there, and we cannot separate any (small) fraction of these which might arise in the jet from the (large) fraction which we attribute to the foreground Faraday screen.

It is important to realize that larger densities of thermal material than those estimated above could be "hidden" in the jet (i.e., remain compatible with the polarization data) if its field configuration has many local reversals along the line of sight without being fully disordered in three dimensions. Such a situation could arise, for example, within the "sheared Laing" field configuration discussed above in § VII*c*.

f) Constraints on the Flow Velocity of the Jet

Many methods have been used in the literature to estimate the average flow velocities of jets on the assumption that their properties are stationary in time. Among those applied to jets which do not appear significantly distorted by orbital interactions and for which $v_j \ll c$ is assumed are the following:

1. Arguments based on the energy flux F required to power the source, from the radiative properties of the lobes. For example, if a lobe of luminosity L_{lobe} is continuously resupplied with energy, and the efficiency of conversion to synchrotron radiation of energy conveyed by the jet is ε, then $F = L_{lobe}/\varepsilon$. The quantity L_{lobe} can be estimated from observations of the lobe and its spectrum at low resolution, but the appropriate value of ε is speculative. The estimate of F is related to the jet parameters as

$$F = \left(u_{int} + \rho_j v_j^2/2\right) v_j \pi R_j^2, \tag{15}$$

where u_{int}, ρ_j, v_j, and R_j are the internal energy density, matter density, velocity, and radius at some point along it. (We neglect the internal structure of these quantities across the jet throughout this section.) To deduce v_j, values of u_{int} are taken from equipartition calculations from the synchrotron properties of the jet, and values of R_j from the widths of the emission profiles. The major unknown is ρ_j.

2. Arguments based on the observed expansion rate of the jet in a regime where it is assumed to be free. As discussed in § VII*a*, the expansion rate of a free jet gives the Mach number M of the flow where it detached from its confinement. The sound speed c_s can be estimated as $c_s = (\Gamma p_{int}/\rho_j)^{1/2}$, where p_{int} is the pressure in the jet and Γ is its ratio of principal specific heats. The jet velocity is estimated as $v_j = Mc_s$. A lower limit to p_{int} can be obtained from the equipartition calculation. The density ρ_j is difficult to estimate, as in method (1).

3. Arguments based on the thrust which the jet must deliver to the feature ("hot spot") in the lobe where it is presumed to terminate. The thrust T that is required in the rest frame of the hot spot must balance $p_{hs}\pi R_{hs}^2$, where p_{hs} is the pressure in the hot spot and R_{hs} is its radius. A lower bound to p_{hs} can be obtained from equipartition calculations for the hot spot, and R_{hs} can be estimated from its synchrotron width. The thrust T is then related to jet parameters through

$$T = \rho_j v_j^{*2} \pi R_j^2, \tag{16}$$

where v_j^* is the velocity of the jet in the rest frame of the hot spot and the other symbols, and the methods of assigning values to them are as in method (1). For a nonrelativistic jet supplying a hot spot that advances with velocity v_{hs} into a medium with density ρ_{IGM}, we also have $\rho_j v_j^{*2} = \rho_{IGM} v_{hs}^2$, so that $v_j^* = \xi v_j$, where $\xi = 1/[1+(\rho_j/\rho_{IGM})^{1/2}]$.

4. An argument which combines methods (1) and (3), by requiring that energy is supplied continuously to the lobes at the luminosity replenishment rate and with the appropriate thrust. If it is assumed that the bulk kinetic energy in the jet dominates its internal energy (so $\rho_j v_j^2 \gg 2u_{int}$), then equations (15) and (16) may be divided to eliminate the direct dependence on jet density ρ_j, giving

$$v_j = 2\xi^2 L_{lobe}/\left(\varepsilon p_{hs}\pi R_{hs}^2\right) \tag{17}$$

There is a residual dependence on ρ_j through the contrast factor ξ. If $\rho_j \ll \rho_{IGM}$ where the jet enters the hot spot, $v_j \gg v_{hs}$ and $\xi \approx 1$.

5. An argument which combines the energy supply requirement (1) with an upper limit to the total mass which can be ejected from the galaxy over the lifetime of the radio source. The rate of mass outflow in the jet is

$$dm/dt = \rho_j v_j \pi R_j^2. \tag{18}$$

The lower limit to the lifetime T of the source can be calculated from the distance d_{hs} between the core and the hot spot divided by the mean rate of advance $\langle v_{hs}\rangle$ of the lobes over the lifetime of the source. If the jet is not constant in direction, $\langle v_{hs}\rangle$ may be less than v_{hs} (the instantaneous rate of advance of a particular hot spot), which in turn is $v_j(1-\xi)$. We can therefore write $T > d_{hs}/v_j(1-\xi)$, so that the total mass ejected by the jet over the lifetime of the source is

$$M_{tot} = \mathrm{T}\, dm/dt > \rho_j d_{hs} \pi R_j^2/(1-\xi). \tag{19}$$

For a "cold" jet with $\rho_j v_j^2 \gg 2u_{int}$ we can eliminate $\rho_j \pi R_j^2$ by

dividing equation (15) by equation (19) to obtain

$$v_j^3 > 2L_{\rm lobe}d_{\rm hs}/\varepsilon M_{\rm tot}(1-\xi). \quad (20)$$

We consider all five methods for estimating the velocity of the jet in NGC 6251. Each method has major uncertainties, so we do not regard any of the following velocity estimates as secure.

We first use method (4), because this relies mainly on observations of the lobe and minimizes the uncertainties arising from the estimate of the density ρ_j in the jet if $\xi \approx 1$. We assume that the jet terminates in the brightest feature of the northwest edge of the lobe (see Fig. 12). The radius of this feature on our 1446 MHz "snapshot" map (corrected for the finite instrumental beam) is 48″, or 21 kpc. The angle subtended by this radius at the nucleus of NGC 6251 is 3°.1. This angle is consistent with interpreting the feature as the termination of the jet, since the angle characterizing the rate of growth of the jet radius with distance from the core over the outer regime of Figure 10 ($180'' < \Theta < 240''$) is 3°.3. The peak flux density of the feature at 1446 MHz is 33 mJy; we use this to calculate its equipartition parameters, assuming that the radio spectrum is a power law of index 0.7 running from 1 MHz to 10 GHz. The lower frequency limit corresponds to integrating down to the same minimum *particle energy* (180 MeV) as in our equipartition calculations for the radio jet. With these assumptions, the equipartition energy density in the feature is $u_{\rm min} = 3.1\times10^{-14}$ Jm^{-3}. The integrated luminosity of the lobe, assuming a spectral index of 0.7 to an upper frequency of 10 GHz, is 1.1×10^{35} W. Substitution into equation (17) gives

$$v_j = 9800\xi^2/\varepsilon \text{ km s}^{-1}.$$

Recalling that $\xi < 1$ by definition, we conclude that *energy and thrust balance can be achieved in this jet at subrelativistic velocities*, provided that the conversion efficiency ε is not too low.

To apply methods (1), (2), or (3) we must invoke the constraints on ρ_j described in § VII*e* above. Recall (*a*) that these depend on assumptions of equipartition and of the magnetic field configuration in the jet and (*b*) that even with these assumptions, the data give *limits* to ρ_j rather than measurements of it. We make the calculations assuming thermal densities *equal* to those given by the *limits* of $n < 4\times10^{-3}$ cm^{-3} at $\Theta = 32''$ and $n < 2\times10^{-4}$ cm^{-3} at $\Theta = 227''$ derived in § VII*e* using the randomized CH fields.

The jet radius R_j at $\Theta = 227''$ (estimated by its HWHM $\Phi/2$) is 6″.5, or 2.8 kpc, and the minimum internal energy $u_{\rm int}$ there from the equipartition calculation for the jet is 6.0×10^{-13} Jm^{-3}. Energy balance then gives the jet velocity as the solution to

$$1.28\times10^{-7}v_j + 3.59\times10^{-20}v_j^3 = 1/\varepsilon.$$

This yields $v_j = 2640$, 6350, and 14000 km s^{-1} for $\varepsilon = 1$, 0.1, and 0.01, respectively. Applying the same method using the data for $\Theta = 32''$ ($R_j = 0.75$ kpc, $u_{\rm int} = 5.4\times10^{-12}$ Jm^{-3}) gives the velocity as the solution to

$$8.28\times10^{-8}v_j + 5.13\times10^{-20}v_j^3 = 1/\varepsilon.$$

This yields $v_j = 2490$, 5710, and 12400 km s^{-3} for $\varepsilon = 1$, 0.1, and 0.01, respectively. If the jet is *assumed* to be "cold" ($\rho_j v_j^2 \gg 2u_{\rm int}$), the first term could be neglected, giving

$$v_j = 2700\varepsilon^{-1/3}\left[6.7\times10^{-24}/\rho_j(32'')\right]^{1/3} \text{ km s}^{-1}, \quad (21)$$

where the second term in brackets measures the ratio of the density at $\Theta = 32''$ to the upper limit of 6.7×10^{-24} kg m^{-3} deduced there in § VII*e*. In contrast, if the jet is *assumed* to be hot ($\rho_j v_j^2 \ll 2u_{\rm int}$), the second term can be neglected, and we find

$$v_j = 12{,}000/\varepsilon \text{ km s}^{-1}.$$

This "hot jet" assumption leads to relativistic jet velocities (to which our equations are inapplicable) for $\varepsilon \ll 0.05$.

Applying method (3) with the hot spot parameters discussed above requires that for thrust balance

$$v_j = 1720/\xi\left[3.4\times10^{-25}/\rho_j(227'')\right]^{1/2} \text{ km s}^{-1}$$

from the data for $\Theta = 227''$, or

$$v_j = 1400/\xi\left[6.7\times10^{-24}/\rho_j(32'')\right]^{1/2} \text{ km s}^{-1} \quad (22)$$

from the data for $\Theta = 32''$.

To apply the expansion-rate method (2) one must assume that the jet is free in its initial rapidly expanding regime. Section VII*a* gave an argument why this is attractive, based on the high X-ray luminosity that would be required to confine the base of this region were it not free. We therefore take $M = 14 \sec\iota$, $u_{\rm int} = 4.4\times10^{-12}$ J m^{-3} near $\Theta = 17''$ from the equipartition calculations there, and $p_{\rm min} = 0.86u_{\rm int}/3$. To estimate ρ_j at $\Theta = 17''$, we convert from the value at $\Theta = 32''$ (where the density was estimated from the depolarization data) assuming constant velocity and mass flux (i.e., that no material from the ambient medium is entrained into the flow). We infer that $\rho_j \le 5.2\times10^{-24}$ kg m^{-3} at $\Theta = 17''$ with these assumptions, so that $c_s \ge 570$ km s^{-1} (taking $\Gamma = 4/3$) and

$$v_j = 8000 \sec\iota\left[5.2\times10^{-24}/\rho_j(17'')\right]^{1/2} \text{ km s}^{-1} \quad (23)$$

for $M = 14 \sec\iota$. Note that the Mach number of the jet in the *thermally confined* BCH model shown in Figure 26 would be only 5.4 sec ι at $\Theta = 17''$.

To apply method (5), we must estimate $M_{\rm tot}$, the total mass ejected in the jet on one side of the galaxy over the lifetime of the source. An upper limit to $M_{\rm tot}$ can be obtained by writing that a fraction $\varepsilon_{\rm out}$ of all of the gas produced by stars throughout the galaxy over the Hubble time is potentially available to participate in the jet outflow (either by falling onto the "central engine" as "fuel" and being ejected in the primary jet, or by subsequent entrainment into the jet). Assuming a production rate of one solar mass per year for this

giant elliptical galaxy, we put $M_{\rm tot} = 5\times10^9\varepsilon_{\rm out}$ solar masses. Using equation (20) with $d_{\rm hs} = 412$ kpc from the western lobe leads to

$$v_j = 656\left[\varepsilon\varepsilon_{\rm out}(1-\xi)\right]^{-1/3}\ {\rm km\ s^{-1}} \qquad (24)$$

As $0 < \xi < 1$ and ε and $\varepsilon_{\rm out}$ are both less than 1, equation (24) argues strongly against very low ($\lesssim 1000$ km s^{-1}) jet velocities where the jet enters the lobe.

Given the many uncertainties in the assumptions upon which these estimates of v_j are based, none can be considered better than a rough order of magnitude for the jet velocity. We note, however, that the estimates based on the energy budget (eq. [21]), on the expansion rate (eq. [23]), and on the thrust balance at the warm spot (eq. [22]) depend on the jet density ρ_j in very similar ways. We can therefore select other parameters of the jet in self-consistent combinations by requiring that these methods yield the *same* velocity to first order, regardless of the jet density. For example, requiring that the estimates (eqs. [21], [23]) from the energy budget and the expansion rate agree demands that $2700\,\varepsilon^{-1/3} \approx 8000 \sec\iota$; i.e. that

$$\varepsilon \approx 0.04\cos^3\iota.$$

We then return this value of ε to equation (20) between v_j and the ejected mass $M_{\rm tot}$, leaving the latter as an unknown parameter. Consistency between equations (20), (21), and (23) then demands a minimum ejected mass $M_{\rm tot}$ (the source lifetime T taking its minimum value of $d_{\rm hs}/v_j$) of 7×10^7 solar masses. This is an acceptable lower limit, compatible with the gas production estimate for an outflow efficiency $\varepsilon_{\rm out} < 0.014$.

We conclude that reasonable "cold" models of the jet exist wherein the jet velocity $v_j \approx 8000$ km s^{-1} and the efficiency $\varepsilon \approx 0.04$, *if* the pressure and density in the jet are close to the lower limit derived from synchrotron relations and the upper limit derived from Faraday effects, respectively. The ratio of bulk kinetic energy in the jet to that in its radiating particles and fields in these models would be $\sim 40:1$. The mass outflow rate would be of order 1.2 solar masses per year.

These parameters do, however, entail a dilemma concerning thrust balance at the warm spot. Matching the velocity estimated from the expansion rate to that inferred from thrust balance in this density regime requires that $8000 \sec\iota \approx 1400/\xi$; i.e., that

$$\xi = 0.18\cos\iota.$$

To obtain $\xi < 0.18$ in conformity with this requires $\rho_j \geq 20\rho_{\rm IGM}$ where the jet approaches the warm spot. This is not impossible, but if the jet is thermally confined as described in § VII*a* and its density is subject to the constraints of § VII*e*, we would infer $\rho_j < 0.35\rho_{\rm IGM}$ at 227″ from the core (see § VII*g* below). To reach a density contrast of 20:1 from these conditions, $\rho_{\rm IGM}$ would have to decline much more rapidly with distance from the core than ρ_j. An alternative view of the thrust balance problem is to say that the jet parameters given above assign the jet ~ 30 times the thrust needed for equilibrium with the equipartition parameters of the warm spot, if the density contrast between the jet and the background medium is in fact less than or equal to 1. This could mean that the jet is still compressing the warm spot (so the latter is not in pressure balance with it), or that the warm spot is far from equipartition, or that the shape of the warm spot was approximated very poorly in the equipartition calculation. (Assuming it to be a very thin disk instead of a cylinder would alleviate the discrepancy).

The low-resolution maps of the lobe in Figures 1 and 12 suggest a more attractive (but not obligatory) alternative. They show that the jet becomes suddenly dimmer just as it enters the more diffuse emission from the lobe, as if the transition between what we have termed the "outer jet" and its faint extension into the lobe marked the onset of a sudden flaring of the jet. This makes it attractive to speculate that around $\Theta = 270''$ (120 kpc from the core) most of the jet flow again became free, perhaps due to a very rapid decline in the external confining pressure. The resulting sudden overexpansion of the bulk of the jet could take place (and "feed" the lobe) while a collimated "core" continues on, bearing only a small fraction of the initial fluxes of energy, momentum, and mass. In this case the velocity estimates derived from the initial expansion rate and from the *integrated* properties of the lobe would be correct for the first 270″ of the jet, but the thrust imparted to the eventual termination of the jet near the warm spot would be greatly overestimated. The "thrust problem" would be removed if the collimated residue of the jet at $\Theta > 270''$ was derived from $\sim 1/30$ of the cross section of the entire jet at $\Theta \leq 270''$.

A jet velocity of 8000 km s^{-1} would imply that the distance traveled by a relativistic electron radiating at 5 GHz in its synchrotron loss time in the inner jet ($\Theta \approx 32''$) would be ~ 30 kpc (70″). The distance traveled in the synchrotron loss time in the outer jet ($\Theta \approx 230''$) would be ~ 210 kpc (490″). The lack of spectral gradients in the jet between 1.4 and 5 GHz (Figs. 5 and 6) would therefore be consistent with velocities of this order or greater even if there were no particle reacceleration along the jet as discussed in § VII*d*. Observations of the jet at 14 GHz, where the scales associated with synchrotron losses would be only 60% of these scales for 5 GHz, may, however, provide independent evidence for particle reacceleration along the jet.

Given that there is no *measurement* of ρ_j, however, we cannot exclude "hot" jet models, which for low conversion efficiencies ($\varepsilon < 0.05$) could require jet velocities of order c for energy balance. Such models could account for the one-sidedness of the jet via Doppler favoritism, at the expense of requiring a substantial deprojection of an already large linear scale for the jet via the $\sec\iota$ factor. (The side-to-side intensity ratio of $\sim 40:1$ between the main jet and the counterjet at $\Theta = \pm 100''$ from the core requires $[v_j/c]\sin\iota > 0.61$ if interpreted as Doppler favoritism.) We stress that the above arguments do not rule out such mildly relativistic jet velocities, but merely show that they are not *required* for energy and thrust balance.

g) *Lateral Oscillations*

In § IV*c* we displayed data on the transverse oscillation of the jet and found that projected wavelengths of 143″, 31″, 12″, 9″, and 5.″7 are present. The peaks in the oscillation power spectra are broad, and the dominant oscillation "wave-

length" tends to increase with Θ. Power spectra computed over restricted ranges of Θ generally had sharper peaks, confirming that the lateral oscillations contain growing, lengthening disturbances.

Among the mechanisms considered in the literature for producing lateral perturbations of jets are (*a*) orbital motion of the primary collimator around another body, whether a companion massive object within the nucleus of the active galaxy (Begelman, Blandford, and Rees 1980; Lupton and Gott 1982) or another galaxy (Blandford and Icke 1978); (*b*) precessional motion of the primary collimator resulting from interaction with another body (e.g., Rees 1978; Begelman, Blandford, and Rees 1980; Icke 1981; Linfield 1981; Gower *et al.* 1982); (*c*) torquing of the confining gas in the interstellar medium during galaxy-galaxy interactions (Wirth, Smarr, and Gallagher 1982); and (*d*) fluid dynamic instabilities at the jet boundary (e.g., Ray 1981, 1982; Hardee 1979, 1982; Ferrari, Trussoni, and Zaninetti 1981, 1983).

Orbital motion alone would lead to a single-wiggle wavelength with fixed amplitude Δ and mirror (C) symmetry between the jet and counterjet. Precessional motion alone (at a single rate) would lead to a single-wiggle wavelength with linear growth in amplitude Δ with Θ (constant amplitude of Δ/Θ) and inversion (S) symmetry between the jet and counterjet. To account for the observed changes in amplitude and for the lengthening of the dominant wavelength of the lateral oscillations of this jet, both orbital and precessional models would need to invoke *multiple* or time-varying motions such as nutations (on whose parameters there would be few or no independent constraints). This multiplicity of parameters would be arbitrary (even if possibly correct). In contrast, the multiple and distance-dependent character of the lateral oscillations of this jet invites interpretation in terms of instabilities of the underlying flow. We therefore consider this mechanism for the oscillations first.

Several authors have analyzed the response of confined jets to Kelvin-Helmholtz instabilities generated at the interface between the jet and the external confining medium. Hardee (1979) and Ferrari, Trussoni, and Zaninetti (1981) discussed the growth of these instabilities in cylindrical jets of constant cross section. They concluded that such jets are unstable to helical and pinching modes whose wavelengths are of the order of the jet circumference. Hardee (1982) examined the stability of isothermal cylindrical jets of *increasing* cross section, a situation that better approximates observed jet behavior. He concluded that expanding jets are also unstable to Kelvin-Helmholtz perturbations, but that the perturbation wavelengths increase, and their growth rates decrease, in proportion to the jet radius. The wave amplitudes should thus increase more slowly than exponentially along an expanding jet. These instabilities could thus in principle mimic the behavior of the lateral oscillations of this jet, producing a complex spectrum of lateral deviations without disrupting it totally.

Two difficulties confront comparisons between the instability models and the observations. The first is that by the time an instability has grown to the extent that it influences the bulk appearance of the jet, it may no longer be properly described as a perturbation of the underlying flow, as in the theoretical models. The second is that observations can determine which lateral oscillation wavelength has the *largest amplitude* at a given distance from the core, while the theory predicts which wavelength *grows fastest*. These need not be the same. Nevertheless, it is of interest to examine whether the existing instability theories predict oscillations whose wavelengths are of the correct order of magnitude to match the observed behavior.

Hardee (private communication) gives the following relations for the wavelength λ_h of the fastest growing helical wave, based on exact numerical analysis of perturbations to the isothermal jet:

$$\lambda_h/R_j \approx f(\eta)\,M - 2.5, \tag{25}$$

where M is the local Mach number of the flow with respect to the internal sound speed of the jet, R_j is the radius of the jet, and $\eta = \rho_j/\rho_{\rm IGM}$, the ratio of the densities inside and outside the jet. The following form of $f(\eta)$ represents the results of Hardee's numerical calculations to within 5% over the range $0.01 \leq \eta \leq 300$:

$$f(\eta) = 4.2/(1+\sqrt{\eta}). \tag{26}$$

Equations (25) and (26) predict that the wavelength of the fastest growing helical mode should lengthen as the jet expands, at least superficially in agreement with our data. (This may be subject to some experimental bias, as discussed in § IV*c*.) We now ask whether these wavelengths are of the correct magnitude to be Kelvin-Helmholtz instabilities, given the range of density contrasts and Mach numbers we can estimate for the jet. If the jet is thermally confined by an external medium at 3×10^7 K, then the external number density at $\Theta = 32''$ is $n_e \geq 4\times10^{-3}$ cm^{-3}, and at $\Theta = 227''$ is $n_e \geq 6\times10^{-4}$ cm^{-3}. Our limits to the internal density ρ_j from § VII*e* therefore correspond to density contrasts $\eta \leq 1$ at $\Theta = 32''$ and $\eta \leq 0.35$ at $\Theta = 227''$. Since the jet must be confined if the oscillations are Kelvin-Helmholtz instabilities, we estimate the local Mach number with those from the confined BCH model of Figure 26, obtaining $M = 8$ at $H = 32''$ and $M = 13$ at $\Theta = 227''$.

In the part of the inner jet ($20'' < \Theta < 40''$) where the $9''$ wavelength dominates, the *average* jet radius R_j, which we take to be $\sim \Phi/2$, is $1''.9$. If this $9''$ oscillation is indeed the fastest growing helical mode in this region of the jet, then $\lambda_h/R_j \approx 4.75$, assuming the jet to lie close to the plane of the sky. For $\eta < 1$, this requires $M \leq 3.2$, appreciably lower than the Mach number at this distance in the BCH model. For $M = 8$, $\lambda_h/R_j = 4.75$ requires $\eta = 13$, in which case either the jet would be completely depolarized at 1370 MHz with the field configurations discussed in § VII*e*, or the confining medium would need to have an implausibly high temperature ($> 4\times10^9$ K). The $9''$ lateral oscillation is thus unlikely to be the fastest growing helical mode if our estimates of these other jet parameters are correct. This difficulty cannot be alleviated by appealing to projection effects. If the jet makes an angle ι to the plane of the sky, both the oscillation wavelength and the jet Mach number will have been underestimated by a factor $\sec\iota$, while R_j is unaffected. Thus, for reasonable Mach numbers, the projection effects cancel through equation (25). In the outer jet region ($140'' < \Theta < 220''$) where the $31''$ wavelength dominates, the average jet radius is $5''.5$, which corresponds to $\lambda_h/R = 5.6$. For a density contrast $\eta < 0.35$,

this requires $M < 3.1$, or for our estimated Mach number of $M = 13$, $\eta = 33$. It is therefore even less attractive to interpret this wavelength as the fastest growing $n = 1$ mode at these distances from the core. Similar conclusions would be reached using the numerical results of Ferrari, Trussoni, and Zaninetti (1983).

The 143″ oscillation dominates the behavior of the jet beyond $\Theta \approx 240''$. If *this* oscillation is interpreted as the $n = 1$ helical mode, then $\lambda_h / R_j \approx 17.5$ where it begins to dominate. This would require either $M < 7.6$ at $\eta < 0.35$, or $\eta = 3$ at $M = 13$.

We conclude that interpreting any of the lateral oscillations of the jet as the most rapidly growing $n = 1$ Kelvin-Helmoltz mode at the distance from the core where they dominate requires either higher density contrasts η between the jet and the confining medium, or somewhat lower Mach numbers, than we would otherwise infer. The 143″ oscillation presents the least severe problems, so this would be the best candidate for the predicted $n = 1$ helical instability. Closer agreement with the other estimates of jet parameters would be obtained if this oscillation were to have grown in a regime somewhat closer to the core, at a smaller value of R_j, and have been convected out to the regime where we observe it as the dominant lateral oscillation.

Because we cannot demonstrate directly that the 143″ oscillation ever grows faster than linearly with Θ, the interpretation of it as a Kelvin-Helmholtz instability could not be distinguished observationally from that of a precessing central collimator. The time scale required for the precession, for a jet velocity $v_j = 8000$ km s^{-1}, would be 7.5×10^6 yr. The most critical test for a precessional model, namely, its ability to mimic the observed lateral oscillations *over several wavelengths* and on *both sides* of a source (producing inversion symmetry), cannot be applied using our current data, because the counter-jet is too faint. Orbital models are not attractive for this source, since there is clear evidence that the deflections Δ grow with distance Θ from the core.

Whichever interpretation is made of the 143″ oscillation, the nature of the faster oscillations is enigmatic. To attribute them also to motion of the primary collimator would imply a complex motion for that object, due to the many different periods involved. The increase of the dominant wavelength with distance from the core would require the dominant period in the motion to be decreasing with time (if the jet velocity is constant). Interpreting them as Kelvin-Helmholtz instability modes would probably require that they be modes other than the fastest growing ($n = 1$) helical mode, perhaps higher harmonics of the kind calculated by Hardee (1982) and by Ferrari, Trussoni, and Zaninetti (1981, 1983). The oscillation with 31″ projected wavelength does increase faster than linearly with distance from the core and involves large changes in the symmetry of the transverse profiles rather than the displacement of the outer contours of the jet. These observations argue against interpreting it as resulting from a *simple* precessional motion with a constant precession cone angle, but it is not clear whether it should be interpreted as a surface instability.

Finally, we note that the wavelength of the fastest growing *pinching* ($n = 0$) Kelvin-Helmholtz mode calculated by Hardee (1982) is given by

$$\lambda_p / R_j = 0.6 M \eta^{-1/3}. \quad (27)$$

Using $\eta = 1$ and $M = 8$ at $\Theta = 32''$, equation (27) predicts $\lambda_p = 9''.1$ in the inner jet. Growth of this mode might therefore account for the separations of the major knots in the inner jet, and for the semiregular oscillations of the expansion rate in the slowly expanding regime of the jet shown in Figure 11. It would, however, remain to be explained why it should be coupled to the transverse displacements of the knot peaks so as to appear also in the Δ-Θ data.

VIII. SUMMARY OF CONCLUSIONS

We summarize our conclusions about the physics of the jet as follows:

1. The jet is not free everywhere. Its initial expansion is so rapid that it may have detached from its initial confinement, and have become free with a Mach number of order 14, within the first 8 kpc from the core. At ~8 kpc from the core, however, it clearly becomes reconfined. This reconfinement can be produced by the thermal pressure of a medium at $\sim 3 \times 10^7$ K whose density decreases from 0.005 cm^{-3} ~4 kpc from the core to 0.0005 cm^{-3} kpc from the core, without violating known constraints from the X-ray data on NGC 6251. Indeed, if the 1.4×10^{42} ergs s^{-1} inner component of the X-ray source detected at NGC 6251 with the *Einstein* IPC has the correct scale, this model for the confinement will be preferred. Further evidence for the transition from freedom to confinement is provided by the lack of a more powerful X-ray source in the inner 1 kpc of NGC 6251.

2. The only center-darkened feature in the jet (at our resolution) occurs where the initial reconfinement of the jet takes place. This feature, and the subsequent train of bright knots in the jet, may be related to the formation of shocks and consequent particle acceleration within the jet during the reconfinement process, as discussed by Sanders (1983).

3. There is clear evidence for a magnetoionic medium within the inner 30 kpc of NGC 6251 but exterior to the jet. This medium produces a large-scale (~30 kpc) RM gradient along the jet, but there is also much substructure on scales from 2.5 to 5 kpc, possibly in a "sheath" around the jet. Its *mean* density, if it was smoothly and spherically distributed around the nucleus of NGC 6251, would be $0.003/B_{-6}$ cm^{-3}, where B_{-6} is the average magnetic field strength in microgauss. Its density and scale may therefore be similar to that of the 3×10^7 K medium required for the reconfinement of the jet. The density-weighted line of sight magnetic field in the medium has reversals on a scale of order 10 kpc.

4. There are strong RM gradients across the jet where its expansion properties change most rapidly. This relationship probably indicates an interaction between the jet and the surrounding magnetoionic medium, but it is not clear whether the underlying physics is the magnetic confinement of the jet, or a secondary perturbation of the medium as a result of reconfinement by other means.

5. The magnetic field within the jet must lack axial symmetry and contain a variable mix of random and organized

components. Randomized variants of the self-similar Chan-Henriksen field configuration consistent with flux conservation and with the observed jet expansion data can be made to fit the transverse profiles of total and polarized intensity reasonably well, provided that both the inclination of the jet and the mixture of random and organized fields vary along the jet. There are, however, significant regions where the apparent magnetic field is oblique to the jet axis. These regions cannot be explained within such models without breaking their axial symmetry. If axial symmetry is broken, the "sheared Laing" fields of equation (6) can also describe the data. The configuration of the magnetic field therefore remains uncertain.

6. Steady-state jet models require relativistic particle reacceleration (or rapid deceleration of the jet flow) to account for the variation of brightness with jet radius. The particle reacceleration (or jet deceleration) may be continuous throughout the inner 120″ (50 kpc), but appears localized to the coreward sides of the bright knots in the outer jet.

7. Models of particle acceleration derived from large-scale vortical turbulence (e.g., Henriksen, Bridle, and Chan 1981) can provide sufficient energy input to account for the brightness of the outer jet if the jet *flow* expands and contracts with the synchrotron FWHM. There is sufficient substructure within the jet that detailed comparisons between these models and the data are inappropriate, however.

8. Only upper limits can be derived for the thermal particle density in the jet from the polarization data, and then only if it is *assumed* that the line-of-sight magnetic field in the jet does not contain large numbers of small-scale reversals (as it could in the "sheared Laing" geometry). The apparent depolarization observed at low angular resolution and lower frequencies by Saunders *et al.* (1981) is an artifact of the foreground RM gradients.

9. Only weak constraints (eqs. [15]–[24]) exist for the jet velocity, in part because of the uncertainty in the thermal density ρ_j in the jet. Models can, however, be constructed wherein the jet provides the necessary energy flux and thrust to power the radio lobe continuously without appeal to relativistic bulk motion. (The brightness asymmetry between the jet and the counterjet would be intrinsic in such models.) "Cold" jet models with velocities ~ 8000 km s^{-1}, conversion efficiencies ~ 0.04 between bulk kinetic energy and synchrotron radiation, and outflow rates near one solar mass per year are compatible with the data. Since we have only upper limits to the jet density, "hot," high-velocity jets cannot be excluded if the efficiency of converting their internal energy to synchrotron radiation in the lobes is less than 0.05.

10. The lateral oscillation spectrum is more complex than *simple* models based either on Kelvin-Helmholtz instabilities or on precession of the central collimator would predict. Neither class of model is strongly favored by the data, but the instability models may require lower Mach numbers, higher density contrast, or both between the jet and the surrounding medium than would otherwise have been inferred. Orbital models are unattractive because the amplitudes of the lateral oscillations grow significantly with distance from the core.

In all of the above except 3, 4, and 5 we have made the now conventional assumption that the synchrotron emission of the radio jet adequately traces the major physical parameters of an underlying flow. We stress that this *is* an assumption, for which the main observational support is the general lack of limb brightening in all such jets (which implies that the synchrotron emission originates in a well-filled volume rather than in a sheath around a more compact flow). Subject to this caveat, a general result of this study is that nonrelativistic models for a thermally confined "cold" flow can provide an appropriate theoretical framework for interpreting this jet. Neither relativistic bulk motion nor magnetic confinement is *required*, although either may be occurring. It is therefore of interest to note that the regimes of Mach number (5–14) and density contrast ($\rho_j/\rho_{\rm IGM} \leq 1$) suggested in § VII for this jet are similar to those for which numerical experiments (Norman *et al.* 1982) on *cylindrical* jet propagation in a *constant density* background produce wholly stable flow systems. The processes leading to the development of strong oblique shocks within the flows examined by Norman *et al.* may therefore be relevant to the formation of the knots, to the origin of the magnetic field perturbations, and to the mechanism of particle acceleration, in this radio jet.

Against this we must balance the fact that our data do not exclude relativistic motion for this jet, and the observation that the parsec-scale jet in NGC 6251 (Readhead, Cohen, and Blandford 1978; Cohen and Readhead 1979) is on the same side of the unresolved core as the kpc-scale jet discussed here. This encourages belief that the reason for one-sidedness in the VLBI jet extends to the kpc scales. It is therefore important to establish whether the parsec-scale structure in this source exhibits superluminal motion or low-frequency variability, either or both of which would favor relativistic motion as the cause of its one-sidedness. It is also important to establish whether the side-to-side intensity asymmetry on the parsec scale in this source is quantitatively similar to that on the kiloparsec scale ($\geq 40:1$).

We are indebted to Robert Laing for a continuing and vigorous dialog on radio jets and their interpretation which stimulated many aspects of this study. We also thank Jean Eilek, Ron Ekers, Ralph Fiedler, Phil Hardee, Dick Henriksen, Bob Sanders, and Dick Sramek for valuable discussions, and Arnold Rots for writing software used to prepare several of the data displays. A. H. B. is most grateful to the NRAO for its hospitality and financial support during leaves of absence from Queen's University at Kingston, Canada, during the early stages of this research, and to the taxpayers of Canada for their (unwitting) subsidy of it through a grant from the Natural Sciences and Engineering Research Council.

REFERENCES

Baan, W. A. 1980, *Ap. J.*, **239**, 433.
Baars, J. W. M., Genzel, R., Pauliny-Toth, I. I. K., and Witzel, A. 1977, *Astr. Ap. Suppl.*, **61**, 99.
Begelman, M. C., Blandford, R. D., and Rees, M. J. 1980, *Nature*, **287**, 307.
Benford, G., Ferrari, A., and Trussoni, E. 1980, *Ap. J.*, **241**, 98.

Bicknell, G. V., and Melrose, D. B. 1982, *Ap. J.*, **262**, 511.
Biermann, P., and Kronberg, P. P., 1983, *Ap. J. (Letters)*, **268**, L69.
Blackman, R. B., and Tukey, J. W. 1958, *The Measurement of Power Spectra* (New York: Dover).
Blandford, R. D., and Icke, V. 1978, *M.N.R.A.S.*, **185**, 527.
Blandford, R. D., and Ostriker, J. P. 1978, *Ap. J. (Letters)*, **221**, L29.
Bridle, A. H. 1982, in *IAU Symposium 97, Extragalactic Radio Sources*, ed. D. S. Heeschen and C. M. Wade (Dordrecht: Reidel), p. 121.
_____. 1984, in preparation.
Bridle, A. H., Chan, K. L., and Henriksen, R. N. 1981, *J.R.A.S. Canada*, **75**, 69 (BCH).
Bridle, A. H., Davis, M. M., Fomalont, E. B., Willis, A. G., and Strom, R. G. 1979, *Ap. J. (Letters)*, **228**, L9.
Bridle, A. H., Fomalont, E. B., and Henriksen, R. N. 1983, in preparation.
Bridle, A. H., Henriksen, R. N., Chan, K. L., Fomalont, E. B., Willis, A. G., and Perley, R. A. 1980, *Ap. J. (Letters)*, **241**, L145.
Burbidge, G. R., and O'Dell, S. L. 1972, *Ap. J.*, **178**, 583.
Burch, S. F. 1979, *M.N.R.A.S.*, **187**, 187.
Burn, B. J. 1966, *M.N.R.A.S.*, **133**, 67.
Burns, J. O., Christiansen, W. A., and Hough, D. H. 1982, *Ap. J.*, **257**, 538.
Burns, J. O., Owen, F. N., and Rudnick, L. 1979, *A.J.*, **84**, 1683.
Chan, K. L., and Henriksen, R. N. 1980, *Ap. J.*, **241**, 534 (CH).
Cioffi, D. F., and Jones, T. W. 1980, *A.J.*, **85**, 368.
Clark, B. G. 1980, *Astr. Ap.*, **89**, 377.
Cohen, M. H., and Readhead, A. C. S. 1979, *Ap. J. (Letters)*, **233**, L101.
Courant, R., and Friedrichs, K. O. 1948, *Supersonic Flow and Shock Waves* (New York: Interscience), p. 387.
Eilek, J. A. 1979, *Ap. J.*, **230**, 373.
_____. 1982, *Ap. J.*, **254**, 472.
Fabricant, D., Lecar, M., and Gorenstein, P. 1980, *Ap. J.*, **241**, 552.
Ferrari, A., Trussoni, E., and Zaninetti, L. 1981, *M.N.R.A.S.*, **196**, 1051.
_____. 1983, preprint.
Fomalont, E. B. 1980, in *IAU Symposium 94, Origin of Cosmic Rays*, ed. G. Setti, A. Spada, and A. W. Wolfendale (Dordrecht: Reidel), p. 111.
Fomalont, E. B., Bridle, A. H., Willis, A. G., and Perley, R. A. 1980, *Ap. J.*, **237**, 418.
Gower, A. C., Gregory, P. C., Hutchings, J. B., and Unruh, W. G. 1982, *Ap. J.*, **262**, 478.
Hardee, P. E. 1979, *Ap. J.*, **234**, 47.
_____. 1982, *Ap. J.*, **257**, 509.
Henriksen, R. N., Bridle, A. H., and Chan, K. L. 1982, *Ap. J.*, **257**, 63 (HBC).
Högbom, J. A. 1974, *Astr. Ap. Suppl.*, **15**, 417.
Icke, V. 1981, *Ap. J. (Letters)*, **246**, L65.
Kellogg, E., Baldwin, J. R., and Koch, D. 1975, *Ap. J.*, **199**, 299.
Ku, W. 1982, private communication.
Lacombe, C. 1977, *Astr. Ap.*, **54**, 1.
Laing, R. A. 1980, *M.N.R.A.S.*, **193**, 439.
_____. 1981, *Ap. J.*, **248**, 87.
Laing, R. A., Bridle, A. H. 1983, in preparation.
Laing, R. A., Bridle, A. H., and Fomalont, E. B. 1983, in preparation.
Lake, R. G., and Roeder, R. C. 1972, *J.R.A.S. Canada*, **66**, 111.
Lea, S. M., Mushotzky, R., and Holt, S. S. 1982, *Ap. J.*, **262**, 24.
Linfield, R. 1981, *Ap. J.*, **250**, 464.
Lupton, R. H., and Gott, J. R. 1982, *Ap. J.*, **255**, 408.
Miley, G. K. 1980, *Ann. Rev. Astr. Ap.*, **18**, 165.
Norman, M. L., Smarr, L., Winkler, K.-H., and Smith, M. D. 1982, *Astr. Ap.*, **113**, 285.
Perley, R. A. 1982, *A.J.*, **87**, 859.
Perley, R. A., Bridle, A. H., Willis, A. G., and Fomalont, E. B. 1980, *A.J.*, **85**, 499.
Perley, R. A., and Cornwell, T. J. 1983, in preparation.
Perley, R. A., and Fomalont, E. B., and Johnston, K. J. 1980, *A.J.*, **85**, 649.
Perley, R. A., Willis, A. G., and Scott, J. S. 1979, *Nature*, **281**, 437.
Ray, T. P. 1981, *M.N.R.A.S.*, **196**, 195.
_____. 1982, *M.N.R.A.S.*, **198**, 617.
Readhead, A. C. S., Cohen, M. H., and Blandford, R. D. 1978, *Nature*, **272**, 131.
Rees, M. J. 1978, *Nature*, **275**, 516.
Rees, M. J., Begelman, M. C., and Blandford, R. D. 1981, *Proc. 10th Texas Symposium on Relativistic Astrophysics* (*Ann. NY Acad. Sci.*, **375**, 254).
Sanders, R. H. 1983, *Ap. J.*, **266**, 73.
Sargent, W. L. W., Young, P. J., Boksenberg, A., Shortridge, K., Lynds, C. R., and Hartwick, F. D. A. 1978, *Ap. J.*, **221**, 731.
Saunders, R., Baldwin, J. E., Pooley, G. G., and Warner, P. J. 1981, *M.N.R.A.S.*, **197**, 253.
Schreier, E. J., Gorenstein, P., and Feigelson, E. D. 1982, *Ap. J.*, **261**, 42.
Schwab, F. R. 1980, *SPIE Proc.*, **231**, 18.
Simard-Normandin, M., and Kronberg, P. P. 1980, *Ap. J.*, **242**, 74.
Strom, R. G., and Willis, A. G. 1980, *Astr. Ap.*, **85**, 36.
Thompson, A. R., Clark, B. G., Wade, C. M., and Napier, P. J. 1980, *Ap. J. Suppl.*, **44**, 151.
Waggett, P. C., Warner, P. J., and Baldwin, J. E. 1977, *M.N.R.A.S.*, **181**, 465.
Wardle, J. F. C., and Kronberg, P. P. 1974, *Ap. J.*, **194**, 249.
Willis, A. G. 1981, in *Proc. 2d ESO/ESA Workshop*, ed. B. Battrick and J. Mort (ESA SP-162), p. 71.
Willis, A. G., and Strom, R. G. 1978, *Astr. Ap.*, **62**, 375.
Willis, A. G., Strom, R. G., Bridle, A. H., and Fomalont, E. B. 1981, *Astr. Ap.*, **95**, 250.
Willis, A. G., Strom, R. G., Perley, R. A., and Bridle, A. H. 1982, in *IAU Symposium 97, Extragalactic Radio Sources*, ed. D. S. Heeschen and C. M. Wade (Dordrecht: Reidel), p. 141.
Willis, A. G., Wilson, A. S., and Strom, R. G. 1978, *Astr. Ap.*, **66**, L1.
Wirth, A., Smarr, L., and Gallagher, J. S. 1982, *A.J.*, **87**, 602.
Young, P. J., Sargent, W. L. W., Kristian, J., and Westphal, J. A. 1979, *Ap. J.*, **234**, 76.
Young, P. J., Westphal, J. A., Kristian, J., Wilson, C. P., and Landauer, F. P. 1978, *Ap. J.*, **221**, 721.

A. H. BRIDLE: National Radio Astronomy Observatory, Edgemont Road, Charlottesville, VA 22901

R. A. PERLEY: National Radio Astronomy Observatory, P.O. Box O, Socorro, NM 87801

A. G. WILLIS: Department of Liberal Studies, Athabasca University, Edmonton, Alberta T5V 1G9, Canada